



Density functional theory and molecular dynamics simulations for resistive switching research



Marco A. Villena^a, Onurcan Kaya^{b,c,e}, Udo Schwingenschlögl^a, Stephan Roche^{b,d}, Mario Lanza^{a,*}

^a Materials Science and Engineering Program, Physical Science and Engineering Division, King Abdullah University of Science and Technology (KAUST), Thuwal 23955-6900, Saudi Arabia

^b Catalan Institute of Nanoscience and Nanotechnology (ICN2), CSIC and BIST, Campus UAB, Bellaterra, Barcelona 08193, Spain

^c School of Engineering, RMIT University, Melbourne, Victoria 3001, Australia

^d ICREA Institut Català de Recerca i Estudis Avançats, Barcelona 08010, Spain

^e Department of Electronic Engineering, Universitat Autònoma de Barcelona (UAB), Campus UAB, Bellaterra, Barcelona 08193, Spain

ARTICLE INFO

Keywords:

Resistive switching
Density Functional Theory
Molecular dynamics
Phase-change
Materials
Metal-oxide materials
Magnetic materials
Ferromagnetic materials
Organic materials
Two-dimensional materials

ABSTRACT

Resistive switching (RS) devices, often referred to as memristors, have exhibited interesting electronic performance that could be useful to enhance the capabilities of multiple types of integrated circuits that we use in our daily lives. However, RS devices still do not fulfil the reliability requirements of most commercial applications, mainly because the switching and failure mechanisms are still not fully understood. Density functional theory (DFT) and/or molecular dynamics (MD) are simulations used to describe complex interactions between groups of atoms, and they can be employed to clarify which physical, chemical, thermal and/or electronic phenomena take place during the normal operation of RS devices, which should help to enhance their performance and reliability. In this article, we review which studies have employed DFT and/or MD in the field of RS research, focusing on which methods have been employed and which material properties have been calculated. The goal of this article is not to delve into deep mathematical and computational issues – although some fundamental knowledge is presented – but to describe which type of simulations have been carried out and why they are useful in the field of RS research. This article helps to bridge the gap between the vast group of experimentalists working in the field of RS and computational scientists developing DFT and/or MD simulations.

1. Introduction

Resistive switching (RS) devices are called to play an important role in future electronic circuits and microchips, due to their excellent electrical properties and relatively easy fabrication process. State-of-the-art RS devices consist of a two-terminal metal/insulator/metal (MIM) cell, whose electrical resistance can be adjusted to two or more stable levels by applying electrical stresses to the electrodes. RS devices are usually integrated at the back-end-of-line interconnections of silicon microchips, right above the complementary metal-oxide-semiconductor (CMOS) transistors, so that no additional area is consumed (see Fig. 1a-b) [1,2]. Commercial RS devices often employ phase-change, metal-oxide, magnetic, or ferroelectric materials, in which the bias triggers electronic and/or atomic rearrangements in the insulating and/or metallic layers, which changes the overall resistance of the entire MIM

cell [3] (see Fig. 1d). Recent studies reported the observation of RS effect in other novel material systems, such as two-dimensional (2D) layered materials and their derivates (including MXenes) [4–6], perovskites [7, 8], organic materials [9,10], meshes of nanowires and nanotubes [11, 12], and Janus particles [13,14], among many others [3,15–19]. However, in these more immature material systems, the reliability of the RS effect is significantly weaker.

The quality and reliability of the RS phenomenon observed in a material system are mainly characterised by four figures-of-merit: (i) the electrical resistance of its different states, (ii) the time and the energy that it takes to switch from one state to another, (iii) the maximum number of times that a device can be switched between two or more states (often referred to as endurance), and (iv) the maximum time that a device stays in a specific state if no write/erase electrical stress is applied (often referred to as retention) [18]. Most RS materials exhibit two

* Corresponding author.

E-mail address: mario.lanza@kaust.edu.sa (M. Lanza).

resistance states, often referred to as high resistive state (HRS) and low resistive state (LRS), but in some others, additional intermediate resistance states can be programmed [20]; however, identifying each of them reliably is much more challenging [18]. Depending on their figures-of-merit, RS devices could be employed for different applications, including data storage, computation, encryption, and transmission (Fig. 1e) [21,22]. RS devices made of phase-change, metal-oxides, or magnetic materials have started to be commercialized as non-volatile memory by 2021 and they represented ~0.5 % of the total standalone memory market (that is, around 621 million USD) [23]. However, intense research is still needed to improve the performance and reliability of RS devices in general, so that they can consolidate within the micro/nano-electronics industry.

RS is a dynamic phenomenon that is mainly associated with stochastic changes in the atomic or electronic structure of the switching material. For this reason, building reliable and durable RS devices requires a full understanding of these switching and failure mechanisms, i.e., the electronic and atomic rearrangements that change the resistance in every cycle and those that provoke one of the states to become permanent after some use. However, most of the experimental studies in this field only measure the electrical properties of the devices in a probe station and propose an explanation for the switching mechanism based on speculative drawings and schematics. In the best cases, the authors include nano-scale images of the devices revealing the morphology and chemical composition before and after the switching, using transmission electron microscopy (TEM) coupled with energy dispersive X-ray spectroscopy (EDS) and/or electron energy loss spectroscopy (EELS) [24].

However, these images are normally not collected in operando, and hence one cannot be completely sure that the atomic rearrangements displayed are the ones responsible for the RS effect. Some studies presented in operando TEM, EDS, and EELS data [25], but the resolution is typically not enough to resolve single atoms or explain the interaction between them, so it is possible only to obtain a general picture of all processes that are taking place. Moreover, detecting some atomic rearrangements influencing many types of RS devices (such as oxygen vacancies in metal-oxides) is extremely complex to detect even when using the most powerful TEM equipment – due to the low contrast produced in the images. Furthermore, the type of electrical stresses (voltage, time) employed to study the switching mechanism of RS devices during in operando TEM, EDS and EELS is usually different from those to which real RS devices would be exposed in an integrated circuit [26]. In addition to that, all mentioned experimental techniques can provide some information about RS processes in which there is an obvious rearrangement of the atomic structure, as occurs in phase change or metal diffusion mechanisms. However, if the switching process is promoted by more subtle mechanisms as in the case of ferromagnetic or RTS, those types of experimental techniques are blind to these processes. Therefore, while the results of such experiments provide useful information to understand how the devices operate in some cases, uncertainties always remain.

Both DFT and MD simulations can provide valuable information about the mechanisms that take place during the RS process at the atomic level. These simulation methods are designed to simulate the interaction between the atoms from the same or different materials,

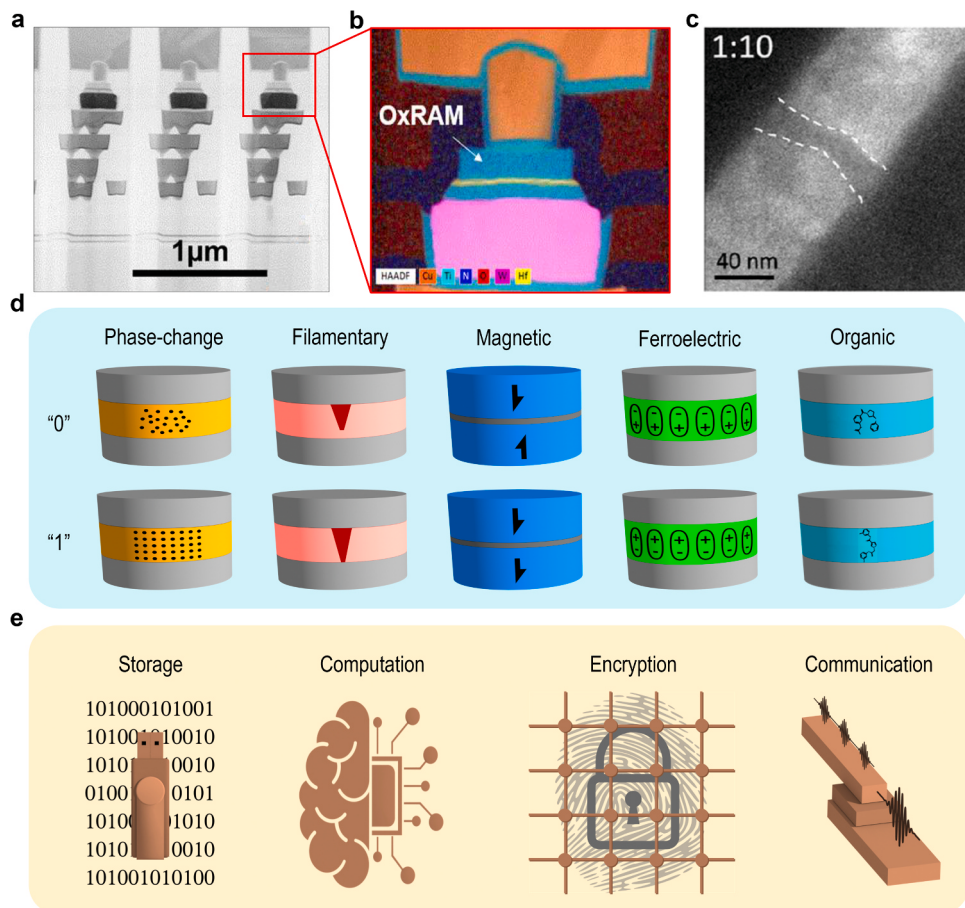


Fig. 1. Structure of resistive switching devices and their applications. **a**, Cross-sectional transmission electron microscopy image of a microchip showing a RS device integrated into a CMOS transistor. **b**, Energy dispersive X-ray spectroscopy image map showing the chemical composition at each single location. **c**, TEM observation for conductive filaments in the Ag/ZnO:Mn/Pt memory cell. **d**, Schematic of the materials mainly used for RS devices. **e**, Schematic of the main applications of RS devices. Modified and reprinted with permission **a** and **b** [288] copyright 2021, IEEE, **c** [289] copyright 2013, ACS publications, **d** and **e** [21] copyright 2022, AAAS.

their evolution over the cycles, etcetera which cannot be experimentally observed. An example of that – although similar studies were done for all other switching mechanisms and materials – is the study of the RS promoted by metal penetration from the electrode to the switching layer. In the early 2000s, one of the most accepted theories was that the RS is controlled by the generation or dissolution of a metallic conductive filament made of metallic atoms provided by the electrodes. The existence of this metallic conductive filament was experimentally observed by TEM image (see Fig. 1c) [27,28] confirming the theory, but it did not provide any explanation about the nature of the filament (is it made of metal ions only?), its location in the device, its evolution during the generation (forming), dissolution (reset), and reconstruction (set) of the filament over the cycles, or how the metal ions can cross the interface between the electrode and the switching layer. However, the different studies based on DFT and/or MD simulations have shed light on those issues [19,29–33]. These results are discussed in detail in Sections 4.2 and 4.3.

In addition, DFT and MD play also an important role in giving support to other simulation models. There are other simulation techniques such as compact modelling, finite elements models, Monte-Carlo models [17,18], or more recently the new models based on machine learning [34,35], frequently used in the study of RS and other fields in different levels [18]. In general, those models need to know in advance the specific properties of the materials present in the system and processes such as band gaps, work functions, formations or activations energy, etcetera for their calibration. Although some of these properties can be experimentally measured, it is not true for all cases or the required technique is very expensive. For these cases, DFT and MD simulations allow us to calculate all properties of the material at a low cost [18].

In this review article, we discuss how DFT and MD simulations can help to understand the functioning of RS devices, describing good practices and discussing multiple examples of such studies in the literature. In Section 2, we review and discuss some of the fundamental concepts of DFT and MD simulations, which are necessary to understand the following sections of this article. In Section 3, we describe the most recommendable methodologies to follow when designing the simulation environment. In Section 4, we analyse the most relevant articles that already used DFT and/or MD simulations in the field of RS research. We describe how previous authors studied multiple atomic and electronic phenomena relevant for RS devices, such as the energy required to generate defect and impurity ions, the drift and diffusion energies of ions in a defective matrix, the charge trapping phenomena near impurities and defects, the electronic structure of doped oxides, and the formation and disruption of conductive nanofilaments (CNFs). Those articles are grouped into sub-sections depending on the type of material analysed, covering phase-change, metal-oxides, magnetic, ferroelectric, organic, and 2D materials. And finally, in Section 5, we describe a RS-related electronic phenomenon of particular interest observed in many different material systems: random telegraph signals (RTS). The goal of this article is not to make deep explanations of the mathematical theory and computational issues related to DFT and MD simulations – that has been already amply discussed in many other articles [36–38]. Instead, we intend to showcase which materials and device parameters can be calculated using DFT and MD simulations and why they are important, aiming to promote collaboration between experimentalists and computational scientists in the field of RS research.

2. Fundamentals

Simulating materials at the atomic level is very challenging, not only because of the large number of elements (electrons and nuclei) to be considered but also due to the complex interactions between them. This problem can be handled using two types of calculations: DFT, which aims to calculate the fundamental properties of the materials (ground state energy, density of states, band structure, etcetera) in a static system; and MD, which models the evolution over the time of a system

affected by the interaction with the environment (temperature, pressure, etcetera). These theories and models were developed in the early 19th century with the advent of quantum mechanics, but they could not be employed systematically in materials systems of more than a few atoms until the end of the 1980s, when computers and advanced numerical methods started to be developed [39–41].

Modern computers running DFT and MD simulations allow performing huge amounts of complex mathematical operations very fast and in parallel. On these computers, the simulations are carried out using specialized software, such as VASP [42], Gaussian [43], Quantum ESPRESSO [44,45], ATK-Quantum Wise [46], CP2K [47], SIESTA [48,49], LAMMPS [50], and others. Some of these software packages are only capable of running DFT simulations, others can run only MD simulations, and others can run both. After analysing most of the literature available in the field of DFT and MD simulations for RS research, we find that ~64 % of the articles use VASP as the main simulation software (see Table 1), although multiple studies use more than one software package.

The development of both DFT and MD models has been a century-long process, and detailed explanations about their accurate functioning can be very extensive [37,38]; hence, providing such detailed descriptions is out of the scope of this work. Instead, Section 2 aims to present fundamental concepts of DFT and MD simulations that are necessary to understand the methodology and literature review presented in Sections 3 and 4.

2.1. Density functional theory

DFT studies the atomic and/or electronic structure of a material by solving the Kohn-Sham equations [51], replacing the original many-body electron problem of the Schrödinger equation by an auxiliary independent particle problem [39]. The construction of this auxiliary system is based on the following two assumptions: (i) the ground-state electron density of the real system can be expressed by the ground-state electron density of the auxiliary system of non-interacting particles; and (ii) the auxiliary Hamiltonian to model the behaviour of an electron with spin σ at a given point r includes the standard kinetic energy operator as well as a local potential, namely $V_{\text{eff}}(r)$. This potential includes contributions from the external potential due to the nuclei, the electron-electron Coulomb potential, and the exchange-correlation potential.

Applying these conditions, the Kohn-Sham equation is expressed as:

$$\left(-\frac{\hbar^2}{2m_e} \nabla^2 + V_{\text{eff}}(r) \right) \Psi_i(r) = \epsilon_i \Psi_i(r) \quad (1)$$

where Ψ_i and ϵ_i are the wavefunction and the energy of state i (respectively), m_e is the electron mass and \hbar is the Planck's constant. The density function $n(r)$ is given by:

$$n(r) = \sum_{\sigma} \sum_i |\Psi_i(r)|^2 \quad (2)$$

Considering Eqs. (1) and (2), and the two aforementioned assumptions, the total energy of a system $E[n]$ is expressed as a functional of the electron density function $n(r)$:

$$E[n] = T_s[n] + \int d\mathbf{r} V_{\text{ext}}(\mathbf{r}) n(\mathbf{r}) + E_{\text{Hartree}}[n] + E_{\text{II}}[n] + E_{\text{xc}}[n] \quad (3)$$

here, $V_{\text{ext}}(\mathbf{r})$ is the external potential due to the nuclei and other external effects, $E_{\text{II}}[n]$ represents the interaction between the nuclei, and $E_{\text{xc}}[n]$ is the exchange-correlation energy. $T_s[n]$ is the independent-particle kinetic energy given by:

$$T_s[n] = -\frac{\hbar^2}{2m_e} \sum_{\sigma} \sum_i \int d^3r |\nabla \Psi_i(r)|^2 \quad (4)$$

and $E_{\text{Hartree}}[n]$ is the Coulomb interaction energy between the electron

Table 1

List of publications with DFT and/or MD simulations results in the RS field. The most relevant type of calculations reported in those articles are: Angle distribution function (ADF), band structure (BS), charge density (CD), conductance (CON), diffusion energy barrier (DIF), density of states (DOS), electron localization function (ELF), energy comparison between states (ESC), formation energy (FE), ferromagnetic polarization (FP), Geometry description (GEO), characterization of the interface between two materials (INT), Inverse participation ratio (IPR), pair correlation function (PCF), polarization transition barrier (PTB), and spin polarization (SP). A detailed description of each term is given in Supplementary Note 1. The information provided by each work about the functional used is collected in the “Functional” column.

	Switching layer	Type of calculation	Software	Functional	Ref.	
Phase Change materials	Ge ₂ Sb ₂ Te ₅ -C _x	PCF, GEO	CASTEP	PBE	[119]	
	GeSbTe, Ge ₂ Sb ₄ Te ₅ , Ge ₂ Sb ₂ Te ₅	DOS, IPR, PCF, GEO	CP2K	PBE	[145]	
	Ge ₂ Sb ₂ Te ₅	PCF, DOS, IPR, GEO	CP2K	PBE	[111]	
	Ge ₂ Sb ₂ Te ₅	PCF, GEO,	VASP	PBE	[139]	
	Sb ₂ Te ₃	FE, DOS, BS, ELF	VASP	PBE, HSE06	[127]	
	Ge ₂ Sb ₂ Te ₅	GEO, PCF,	CPMD	PBEsol	[140]	
	Ge ₂ Sb ₂ Te ₅	DOS, GEO	CP2K	PBE0	[130]	
	Ge ₂ Sb ₂ Te ₅	GEO	VASP	–	[120]	
	GeTe/Sb ₂ Te ₃	GEO	VASP	PBE	[131]	
	Ge _x Sb _y Te _z	GEO	ABINIT	PBE	[133]	
	Ge ₂ Sb ₂ Te ₅	GEO	VASP	–	[121]	
	VO ₂	BS, INT	CASTEP	PBE	[291]	
	(Cu, Ag, Au)InTe ₂ , (Cu, Ag, Au)SbTe ₂	ELF	ABINIT	LDA	[117]	
	Ge ₂ Sb ₂ Te ₅	GEO, PCF, ADF	VASP, LAMMPS	PBEsol	[292]	
	Ag _{0.5} Ge ₂ Sb ₂ Te ₅	GEO, PCF	VASP	PBE	[123]	
	GeTe	GEO, DOS	CP2K	PBE, LDA	[110]	
	In ₁₅ Sb ₈₅ , Ge ₁₅ Sb ₈₅	PCF, GEO	CP2K	PBE	[144]	
	(SiTe) ₂ (Sb ₂ Te ₃) _n	BS, GEO	WIEN2K	PBE	[125]	
	GeTe	PCF	SIESTA	–	[293]	
	Ge ₂ Sb ₂ Te ₅	ADF, GEO	VASP	PBE	[122]	
	Ge ₂ Sb ₂ Te ₅	GEO, DOS	VASP	PBE	[126]	
	Ge ₂ Sb ₂ Te ₅	GEO, PCF, DOS	VASP	–	[129]	
	Ge ₂ Sb ₂ Te ₅ , Ge ₈ Sb ₂ Te ₁₁ , Ge ₂ SbTe ₂ , Ge ₄ SbTe ₂ , Ge ₂ SbTe ₂	GEO, ADF	VASP, CP2K	PBE	[128]	
	Ge ₂ Sb ₂ Te ₅	GEO	VASP	–	[118]	
	GeSb ₂ Te ₄	GEO, DOS, IPR	CP2K	gradient-corrected functionals	[132]	
	Ge _x Sb _y Te _z	DOS, IPR	CP2K	gradient-corrected functionals	[108]	
	Ag ₄ In ₃ Sb ₆₇ Te ₂₆	PCF	CP2K	GGA	[124]	
Metal Oxide materials	Oxygen Vacancies	HfO _x , Hf _x Ti _y O _z	DIF	VASP	–	[161]
	HfO ₂	DIF	VASP	PW91, HSE06	[153]	
	HfO ₂	FE, CD	VASP	PW91, HSE06	[154]	
	HfO _x	GEO, CD	–	LDA	[151]	
	HfO ₂	FE, CD, DOS, GEO	VASP, CASTEP, DMol	PBE	[155]	
	Black Phosphorus	DOS, ELF	VASP, CASTEP, DFTB+	GGA+U	[179]	
	HfO ₂	DOS	VASP	LDA+U, PBE0, HSE06	[174]	
	HfO ₂	FE, ELF, DIF	VASP	LDA+U, HSE06	[156]	
	HfO _x	DOS, FE	VASP	LDA+U, HSE06	[181]	
	CeO ₂	DOS, CD, INT	VASP	PBE, HSE06	[178]	
	Ta ₂ O ₅	ELF, DOS	VASP	GGA+U	[186]	
	SrZrO ₃	DOS, BS, FE, ELF	VASP	PBE	[171]	
	NiO	DOS, CD, DIF	VASP	LDA	[163]	
	CeO ₂	DOS, FE, CD	VASP	PBE, HSE06	[184]	
	TaO _x	DOS, CD	VASP, QuantumATK	PBE, HSE06	[169]	
	TiO ₂	FE, BS	VASP	LDA+U	[166]	
	Ta ₂ O _{5-x}	PCF	VASP	PBE	[185]	
	TiO ₂ , NiO, Pr _{0.7} Ca _{0.3} MnO ₃	FE, CD, DOS	VASP	LDA+U, GGA+U	[164]	
	TiO ₂	BS, DOS, ELF, FE,	VASP	LDA+U, GGA+U	[172]	
		GEO				
	TiO ₂ , HfO ₂ , Al ₂ O ₃	CD, FE	VASP	LDA+U, GGA	[183]	
	NiO	DOS, FE, CD	VASP	SGGA+U	[162]	
	MgO	DIF	VASP	PW91	[188]	
	HfO ₂	CON	SIESTA	LDA	[157]	
	TiO ₂	ELF, DOS, FE	VASP	LDA+U	[165]	
	TiO ₂	DOS, INT, DIF	VASP, CRYSTAL06	PBE, B3LYP	[30]	
	Ta ₂ O ₅	DOS, CD	VASP	PBE	[170]	
	TiO ₂	DOS, CD	FLEUR	–	[167]	
	V ₂ O ₅	FE	VASP	PBE	[168]	
	NiO	DOS, INT, CD,	VASP	PBE, HSE03, HSE06, B3LYP	[74]	
		GEO				
	ZrO ₂	DOS, FE, GEO	VASP	PBE, PBE+U, PBEsol, PBE0, B3LYP, HSE06	[29]	
	ZrO ₂	FE	CASTEP	PW91	[182]	
	HfO ₂	DOS	VASP	PBE, HSE06	[159]	
	TiO ₂	BS, DOS, ELF, FE	VASP	LDA+U	[173]	
	TiO ₂ +Sr, Al, Zr, Hf, V, Cr, Co, Ni, Cu	DOS, FE	VASP	LDA+U	[176]	

(continued on next page)

Table 1 (continued)

	Switching layer	Type of calculation	Software	Functional	Ref.
	HfO _x	FE, ELF	VASP	–	[152]
	HfO ₂	DOS, BS, FE, CD	VASP	GGA	[180]
	Ta ₂ O ₅	DOS, FE, CD, DIF	VASP	PBE, HSE06	[187]
Metal Ions	aSiO ₂	INT, DIF, CON	QuantumATK, CP2K	PBE, GTH	[195]
	CeO ₂	DOS, CD, INT	VASP	PBE, HSE06	[178]
	CeO ₂	DOS, FE, CD	VASP	PBE, HSE06	[184]
	GeTe	CD, GEO	VASP	PBE	[294]
	InSe	DIF	VASP	–	[295]
	ZnO	DIF	Quantum ESPRESSO	PBE	[296]
	SiO ₂	GEO	LAMMPS	–	[31]
	SiO ₂	GEO, INT	VASP	PBE	[297]
	TiO ₂	DOS, INT, DIF	VASP, CRYSTAL06	PBE, B3LYP	[30]
	TiO ₂	DOS, CD, INT	QMAS	GGA+U	[193]
	ZrO ₂	DOS, FE, GEO	VASP	PBE, PBE+U, PBESol, PBE0, B3LYP, HSE06	[29]
Magnetic materials	Zn _{1-2x} Cr _x Ti _x Se, Zn _{1-2x} Cr _x Ti _x Te	DOS, SP	–	GGA	[228]
	CrO ₂	BS, SP	QuantumATK	SGGA	[229]
	PtMn ₃ N _{0.25}	DOS, SP	WIEN2k	PBE96	[298]
	NiMnSb	BS, SP	–	–	[233]
	Ni ₂ MnGa	GEO, BS, DOS, SP	VASP	GGA	[238]
	Fe ₃ GeTe ₂	BS, DOS, SP	Quantum ESPRESSO	PBE	[230]
	CaV ₃ S ₄ , CaMn ₂ S ₄	BS, DOS, SP, GEO	WIEN2k	PBESol	[237]
	MgO	BS, SP	SIESTA	–	[231]
Ferroelectric materials	HfO ₂ , ZrO ₂	FP, PTB	VASP	PBE, HSE	[250]
	PbTiO ₃ , PbZrO ₃	PCF, FP	Quantum ESPRESSO	–	[254]
	HfO ₂	PTB	Quantum ESPRESSO	LDA	[251]
	BiFeO ₃ , Sm _x Bi _{1-x} FeO ₃	FE	VASP	LDA+U	[242]
	HfO ₂	PTB	ABINIT	PBE	[239]
	LSMO/SrTiO ₃ /LSMO	DOS	Quantum ESPRESSO	LDA+U, PBE	[299]
	Hf _{0.5} Zr _{0.5} O ₂	GEO	Quantum ESPRESSO	BLYP	[255]
	HfO ₂	FE, PTB, GEO	ABINIT	PW, PBE, HSE06	[75]
	ZrO ₂	PTB	ABINIT	LDA	[241]
	Hf _{1-x} Zr _x O ₂	GEO	ABINIT	PW	[249]
	[InCl ₆ H ₁₁ N ₂ O ₈] _{1.5} H ₂ O	DOS, GEO	CP2K	PBE	[243]
	PbTiO ₃	PTB	VASP	LDA	[300]
	BaTiO ₃	DOS	VASP	–	[301]
	Al _{0.75} Sc _{0.25} N	DOS, CD, FE	Quantum ESPRESSO, VASP	PBE	[244]
	Al _x Sc _{1-x} N _y	FE, DOS	Quantum ESPRESSO	PBE	[245]
	BaFe ₁₂ O ₁₉	BS	VASP	PBE+U	[302]
Organic materials	HKUST-1	DOS	VASP	PBE	[303]
	pC6DTP	BS	GAUSSIAN09	B3LYP	[304]
	[Ru ^{II} L ₃](PF ₆) ₂	INT	VASP	PBE-D3	[305]
	[Fe ^{II} L' L ₂](PF ₆)	ESC	VASP	PBE	[306]
	S(CH ₂) ₁₁ MV ²⁺ X ₂ ⁻	CD	VASP	B97D	[307]
	D-π-A, D-π-D, A-π-A	CD, ESC	VASP, GAUSSIAN	–	[223]
	rGO-th	BS, INT	DMol	PW91	[308]
	GO-PVK	CD	GAUSSIAN03	B3LYP	[309]
	DDP-CuNP	ESC, DOS	CP2K	PBE-D3	[310]
	MAPbI ₃	INT, FE, BS, DOS	VASP	PBE	[222]
	eCPF	CD	GAUSSIAN09	–	[311]
	CS-GO	DOS	CP2K	PBE	[312]
	CH ₃ NH ₃ PbI ₃	DOS, BS, CD, FE	VASP	GGA	[221]
2D materials	HfS ₂	BS	Quantum ESPRESSO	PBE	[211]
	MoS ₂	INT, DIF	VASP	PBE	[19]
	h-BN	DOS, BS	VASP	PBE	[219]
	MoS ₂	DOS	VASP	PBE-D2	[32]
	HfS ₂	BS, DOS	VASP	PBE	[210]
	h-BN	DOS, DIF	VASP	PBE-D3	[207]
	MoS ₂	FE, DIF	VASP	PBE	[218]
	h-BN	FE	VASP	PBE	[205]
	h-BN	CD	LAMMPS, QuantumATK	PBE-D3	[206]
	h-BN	FE	VASP	PBE-D3	[215]
RTS	HfO ₂	DOS, CD	VASP	PW	[275]
	SiO ₂	ESC, CD	VASP	PBE	[265]
	Si	ESC	ABINIT, VASP, Quantum ESPRESSO	–	[313]
	SiO ₂	ESC	LAMMPS	HSE	[314]
	SiO ₂	GEO, CD	GAUSSIAN03	B3LYP	[277]
	HfO ₂	BD, DOS, CD, ESC	CRYSTAL03	B3LYP	[276]
	SiO ₂	ESC, CD	VASP	PBE	[271]
	SiO ₂	ESC, CD	VASP	PBE	[315]

density $n(r)$ and itself defined as:

$$E_{\text{Hartree}}[n] = \frac{e^2}{8\pi\epsilon_0} \int d^3r d^3r' \frac{n(r)n(r')}{|r - r'|} \quad (5)$$

Using this formalism, the ground state energy $E[n]$ (Eq. 3) can be calculated for certain approximations of the exchange-correlation energy $E_{xc}[n]$ and the external potential $V_{ex}(r)$. In most software packages for DFT simulations, it is possible to use three approximations of exchange-correlation energy (often referred to as functional): the local density approximation (LDA) [40], the generalized gradient approximation (GGA) [41,52], and the hybrid functional.

The LDA functional considers the solid as a homogeneous electron gas. Under this rough approximation, the exchange-correlation energy is a local effect that can be modelled as integral of the exchange-correlation energy density over the entire space:

$$E_{xc}^{\text{LDA}}[n] = \int d^3r n(r) [\epsilon_x^{\text{hom}}[n] + \epsilon_c^{\text{hom}}[n]] \quad (6)$$

where ϵ_x^{hom} and ϵ_c^{hom} are the exchange and correlation energy densities, respectively. The ϵ_c^{hom} was calculated with Monte Carlo methods by D. M. Ceperley and B. J. Alder [53]. In general, there are several versions or approximations for ϵ_x^{hom} that can be used as different approaches of the LDA [54]. For all of them, the computation cost is usually low due to the strong approximations used.

The GGA functional is an improvement of the LDA functional and considers the inhomogeneities of the electron density by its value and gradient at each point. In this way, the total exchange-correlation energy can be expressed as:

$$E_{xc}^{\text{GGA}}[n] = \int d^3r n(r) \epsilon_x^{\text{hom}}[n] F_{xc}(n, |\nabla n|) \quad (7)$$

where F_{xc} is a dimensionless function. Like the LDA, several GGA approaches propose different versions of F_{xc} according to certain approximations. Table 2 lists the most common GGA approaches. In general, the GGA functional is the most widely used functional because it provides the best trade-off between simulation time and accuracy.

Hybrid functionals augment the DFT exchange-correlation energy with the Hartree-Fock exchange energy. This type of functionals can be more accurate, but its computational cost is high. Hence, it is frequently used only for small systems or for very specific calculations. Like the LDA and GGA, there are several hybrid functionals approaches (see Table 2) according to the approximations used.

2.2. Molecular dynamics

Classical molecular dynamics (MD) simulations calculate the position and morphology of particles (atoms, clusters of atoms, molecules) over time by solving the kinetic equations. First, the interaction between

atoms (or molecules) is modelled by a potential field (Eq. 8). Second, the potential field is derived to obtain the force field ($F = -\nabla V(r)$). And third, the acceleration of each particle in the system is calculated over time. The main difficulty of this calculation relies on determining the interatomic potential field, which is usually approximated to:

$$V(r_i) = \sum_{i=1}^N V_1(r_i) + \sum_{i \neq j} V_2(r_i, r_j) + \sum_{i \neq j \neq k} V_3(r_i, r_j, r_k) + \dots \quad (8)$$

where each term describes one aspect of the interaction between the N particles and the environment (boundary conditions). Most software packages available use the classical MD which only considers the first three terms to ensure a good trade-off between accuracy and simulation time. However, there are more sophisticated implementations of this interatomic potential (or force) field that can describe more complex interactions or systems such as chemical reactions (where chemical bonds are created are/broken) or interactions between complex molecules.

The first term of Eq. (8) represents the external perturbations present in the system (external electric field, pressure, others) at each position (r_i). The second term models the interaction between two atoms placed in the positions r_i and r_j , which can be related to bonding interactions (depending on the type of chemical bond) and non-bonding interactions (Coulomb interaction or van der Waals forces). Bonding interactions are usually modelled considering the interaction between two atoms as a classical elastic interaction between two bodies. Under this approximation, the bonding potential equation is equivalent to a Newtonian potential:

$$V(r) = k(r - r_0)^2 \quad (9)$$

where k is the force constant and r_0 is the equilibrium distance of the bond. The non-bonding interactions are usually described by the classical Lennard-Jones potential which combines the Pauli repulsion and the dispersion interaction [55,56]:

$$V(r_{ij}) = 4\epsilon \left[\left(\frac{\sigma}{r_{ij}} \right)^{12} - \left(\frac{\sigma}{r_{ij}} \right)^6 \right] \quad (10)$$

where r_{ij} is the distance between the atoms i and j , ϵ is the depth of the potential well (usually referred to as dispersion energy), and σ is the distance between particles at which the potential energy is zero. The third term in Eq. (8), that is $V_3(r_i, r_j, r_k)$, considers the angle formed by the atoms placed at the locations r_i , r_j , and r_k . This type of interaction is similar to the bonding interaction but depends on the angle (θ) rather than the distance between atoms, and it is calculated as:

$$V(\theta) = k(\theta - \theta_0)^2 \quad (11)$$

The parameters k , r_0 , etcetera can be determined experimentally or

Table 2
Most common approaches of LDA, GGA, and Hybrid functionals available.

	Functional	Authors	Ref.	Comments
LDA	SVWN	Slater, Vosko, Wilk, Nusair	[316,317]	Rough.
	PW	Perdew, Wang	[70]	Low computational cost.
GGA	BP86	Becke, Perdew	[40,318]	Underestimation of the band gap.
	BLYP	Becke, Lee, Yang, Parr	[40,73]	Low computational cost.
	PW91	Perdew, Wang	[319,320]	
	PBE	Perdew, Burke, Ernzerhof	[321]	
	PBEsol	Perdew, Ruzsinszky et al.	[322]	
	RPBE	Hammer, Hansen, Norskov	[323]	
	SOGGA	Zhao, Truhlar	[324]	
Hybrid functional	B3LYP	Becke, Lee, Yang, Parr	[325]	Good estimation of the band gap.
	PBEO	Perdew, Ernzerhof, Burke	[326]	High computational cost.
	HSE	Heyd, Scuseria, Ernzerhof	[327]	
	B97	Becke	[328]	
	TPSSh	Staroverov, Scuseria, Tao, Perdew	[329]	

via DFT, and they are available in the literature or provided by the developers of the different MD simulation software for many material systems [57]. Using accurate values for these parameters is crucial to achieving a good value of the potential/force field via MD. However, for some material systems, the accuracy of these parameters is limited by the available experimental data and/or the computation cost required for the DFT simulations. Recent developments in machine learning have been used to improve the accuracy of the parameters used in the calculation of the force field [58–60].

In previously described classical MD, the type of interactions or bonds between atoms are stable and cannot be dynamically broken or created during the evolution of the system over time. It means that the classical potential (or force) field is not adequate for RS research because the generation and recovery of vacancies during the generation of the CNFs are not correctly modelled. During the creation and dissolution of CNFs, new atomic bonds are created and dissolved, so the potential field must consider these types of processes. In this case, it is recommended to use reactive MD which is based on a more accurate implementation of the force field called reactive force field (ReaxFF) [61,62]. ReaxFF uses the classical formalism previously explained adding additional empirical interatomic potentials that dynamically model the bond-order interaction between atoms. In this case, the force field is derived from the energy expression:

$$V_{\text{system}} = V_{\text{bond}} + V_{\text{over}} + V_{\text{angle}} + V_{\text{tors}} + V_{\text{vdWaals}} + V_{\text{coulomb}} \quad (12)$$

where V_{bond} describes the potential associated with forming bonds between atoms. V_{over} is a penalty preventing the over-coordination of atoms. V_{angle} and V_{tors} are the potentials associated with three-body valence angle strain and four-body torsional angle strain. V_{vdWaals} and V_{coulomb} model the electrostatic and dispersive interaction between all atoms. Each potential from Eq. 12 represents a function that models each contribution. As it happens for classical MD, all potential functions have several parameters that are calculated using empirical techniques or DFT simulations [61].

3. Methodology

For a specific material system and problem to solve, selecting the most suitable model, approximations, and set of parameters for the simulation (pseudopotential, k-point grid, cut-off energy, etcetera) is essential to obtain a good result. A bad selection of these parameters can result in erroneous values and interpretations, prohibitively long computation times, and/or even convergence problems that result in infinite computation times. It should be noted that the selection of the set of parameters brings associated an inherent trade-off between the accuracy of the results and the computation time needed to obtain the result. Typically, the average computation time of DFT or MD simulations is higher than other simulation techniques [18], and it can be from a few seconds to several days. Mainly, the computation time depends on the number of atoms in the system, the set of parameters, and the computation power of the supercomputer used. For this reason, a set of parameters that may be valid for one supercomputer might not be practical for a different supercomputer. In the following subsections, we describe important considerations when making such selections. We often refer to the software VASP — which can run both DFT and MD simulations — because it is by far the most used in the field of RS (see Table 1), although the basic concepts are similar for other software and implementations.

3.1. Choosing the pseudopotentials

The potential generated by the atoms is one of the main interactions modelled by DFT. Due to the complexity of calculating this potential, it is replaced by a simplified version, often referred to as pseudopotential. The pseudopotential treats the core electrons that are strongly bound to

the atomic nucleus as a part of the nucleus, and only electrons that can be part of interactions between atoms are considered.

The choice of the pseudopotential and its parameters is critical in achieving an accurate and reliable simulation result since it always adds certain errors to the calculations because of the mentioned simplifications adopted. The most employed pseudopotentials can be divided into three groups: norm-conserving pseudopotential (NCP) [63], ultra-soft pseudopotential (USPP) [64], and projected augmented waves pseudopotential (PAW) [65,66].

Except for specific applications, the PAW pseudopotential is the most used in the RS research because it provides an accurate enough approximation to keep the simulation time in a reasonable range. PAW potentials have been calculated for all elements in the periodic table and they are usually provided by developers of each simulation software. In the case of the PAW provided by VASP [67], each potential is provided in several flavours or approaches for different approximation levels identified by the extensions h , s , pv , sv , and d . The extension h (harder) implies that the potential takes a more accurate approximation than the standard potential and hence requires a greater energy cut-off. The extension s (softer) means that the potential was calculated using a rougher approximation than the standard version. The extensions pv , sv , and d imply that the p , s , and d semi-core states are treated as valence states, respectively.

It should be noted that in soft materials (such as organic materials, see Section 4.5) the influence of the core electrons often cannot be neglected, so the use of pseudopotential approximations is not recommended. For these scenarios, one can use DFT codes that take into account the near-nucleus electrons using, for instance, a full potential (linearized) augmented plane wave and local orbitals (as implemented in Wien2k [68]) or simply all states represented by Gaussian orbitals (used in CRYSTAL17 [69]).

3.2. Choosing the exchange-correlation functional

The total energy of the system is expressed as a function of the electron density. The exchange-correlation functional is a crucial part of this functional because it is a measure of the energy released when two or more electrons with the same spin are in the same region of space. When this situation occurs, the exchange can be interpreted as a correction to the repulsive energy and is often referred to as the Fermi correlation. On the other hand, correlation is a measure of the energy released due to the movement of one electron being influenced by the presence of all other electrons due to their Coulomb repulsion.

There are many different forms of the exchange-correlation functional, and each of them has its own set of approximations and limitations. However, the functional (especially the correlation part) is critical when treating strongly correlated materials, such as transition metal oxides, which is one of the most employed family of materials used in RS devices. For this reason, the choice of exchange-correlation functional can significantly impact the accuracy of our results.

In general, LDA functional makes the roughest approximation, where the electron exchange-correlation energy is the same as in a uniform electron gas. GGA functional considers some inhomogeneities in the energy distribution, which is a more realistic representation without increasing the simulation time too much compared to the LDA approach. GGA gives good results on the structure relaxation or for comparative studies, but it is important to take into account that the calculation of the band gap of the material under study will be underestimated. Hybrid functionals are more accurate and overcome this problem, but they often require more computing resources and/or computing time. Hybrid functionals include a mixture of both GGA (or LDA) and the non-local exchange approximation, typically from the Hartree-Fock theory. When using hybrid functionals it is recommendable to split the project into two parts: first use a GGA functional for the first calibration of the main parameters and the initial relaxation, and second use the hybrid functional to calculate the desired parameter.

Although we are speaking about three types of functionals, there are several versions of all of them as Table 2 shows. In the case of GGA, the most common functional is the Perdew-Burke-Ernzerhof (PBE) [70], which in the field of RS has been particularly useful to calculate the relaxation of the crystal structure and formation energy of the defects involved in the switching, although there are more approaches available [71]. On the other hand, the Heyd-Scuseria-Emzerhof (HSE) [72] and the Becke-(3 parameters)-Lee-Yang-Parr (B3LYP) [73] are the hybrid functionals most used. A detailed revision of the most relevant hybrid functionals for different software can be found in the reference [15]. A good practice is to compare the results calculated using different functionals [29,74–76].

Note that the long-distance interactions between particles are not considered in the mentioned functionals since their interactions are usually negligible. This practice simplifies the equations and speeds up the calculations. However, the Van der Waals forces play a significant role in the dynamics of two-dimensional materials [77] like transition metal dichalcogenides (e.g., MoS₂ and WSe₂) [78–80], and tri-chalcogenides (e.g., TiS₃ and ZrS₃) [81–83] which are also used in the fabrication of RS devices and other electronic devices [2]. For this reason, it is necessary to use long-range functionals that usually are more accurate than the semi-empirical approaches. One of the most used is the vdW-DF functionals [84,85] whose non-local correlation accounts for dispersion interactions. In this way, the van der Waals contributions of atoms due to their local chemical environment are considered.

3.3. Choosing the K-points grid over the Brillouin zone

In DFT, the total energy of the crystalline structure under study is calculated as the sum of the contributions of all electrons in the continuum space, but this calculation is very expensive. However, according to the Bloch's theorem [86] the total energy of a crystal can be calculated from the electron wavefunction by considering a grid of points (usually called k-points) defined in the first Brillouin zone of the crystal. In this way, the energy is now calculated on a finite grid of points only, which is a huge computational simplification. The correct definition of the k-points has a strong effect on the accuracy, convergence stability, and the computation time required for the calculations.

In most cases, the k-points are generated by the code as Gamma-centred mesh or as Monkhorst-Pack mesh. The Gamma-centred mesh uses the centre of the Brillouin zone, also known as the gamma centre, as the origin of the mesh. From there, all points of the grid are generated following the symmetry of the lattice vectors of the crystalline structure. The algorithm automatically selects the optimal positions of the k-points to ensure the uniformity of the sample of the Brillouin zone. In the case of the Monkhorst-Pack scheme [87], it follows a similar procedure to generate the grid of points, but its centre is shifted from the gamma centre to a certain value. In both methods, in the case of VASP and other software packages, the user must manually define the number of points that the software has to generate along each direction. Typically, both types of grids reduce the computation time, keeping the accuracy of the simulation in a reasonable range. However, they can fail to describe the ground state of metals due to the large number of free electrons, which cannot be correctly calculated with a homogeneous grid.

In general, the best practice to determine the correct number of k-points defined along each lattice direction is to plot the total energy of the system versus the k-points to find the convergence value of energy in a reasonable simulation time. However, in the case of VASP, there are several tools available, such as VASPKIT [88] that can help with this task providing a starting point for this calibration process.

In the field of RS (and other materials/devices), one of the most common results provided is the band structure calculation (see Table 1). In this case, the k-points are systematically defined along the high-symmetry paths of the crystal under study. Although the definition of all k-points can be manually done, several website tools such as *SeeK-path* [89] or *Bilbao Crystallographic server* [90] automatically calculate the

correct grid based on the crystal structure. This website is compatible with several software packages.

In the research of RS mechanisms, it is common to work with large systems with a high number of atoms. These systems require a lot of computation resources, so it is not possible to use a dense k-point grid. To solve it, the Gamma-only grid (or Γ -point grid) is commonly used. This Γ -point grid only includes the gamma point of the Brillouin zone for the calculations dramatically reducing the computation time. However, the simulation cell in the real space must be large enough (>10 Å each lattice distance) to compensate for the local errors added using that very low number of points in the grid.

Another particular case frequently studied in the RS field is the case of 2D materials (see Section 4.6) or slab surfaces. In this type of unit-cells where only a few layers are considered, an empty gap bigger than 12–15 Å is forced on the top (or bottom) of the crystal to avoid the interactions between atoms due to the periodic boundary conditions. For simplicity, a common practice is to set only one k-point along the out-plane direction to reduce the number of calculations along the empty space.

3.4. Software and parameters

When working with DFT or MD simulations, different sets of parameters must be defined depending on the software used. While all parameters are important, a few of them are critical and need to be calibrated to achieve an accurate result. In general, these parameters define the threshold of the different magnitudes considered or calculated during the calculations. The most common critical parameters defined for the type of simulations used in the RS field are:

3.4.1. Cut-off energy

A frequent strategy used to represent the electronic orbital is the choice of the appropriate basis set. In general, these auxiliary functions are a linear combination of Gaussian functions centred around the nuclei (used by CP2K, for instance) or plane waves implemented uniformly throughout the simulation domain (used by VASP, for instance). Theoretically, an infinite number of those functions is required to produce an exact result, which is unfeasible. In this context, the parameter cut-off energy is used to define the range of energies for the plane-wave-basis for which the calculations are executed, so all plane waves with energy smaller than the cut-off energy are included. In general, the solutions of the plane waves with high energy do not affect too much to the final solution, so they can be ignored by using lower values of the cut-off energy. VASP developers suggest using a cut-off energy of 130 % cut-off energy of the pseudopotential used [91,92], which is a good first approximation in most cases that they studied. While this approach can help users to spare computing hours (that is, money and time) the correct practice is to manually plot the value of the cut-off energy versus the total ground energy of the system under study versus the simulation time. The idea of this graph is to find the cut-off energy value for which the ground energy solution converges (according to the error target) in the shortest possible time [93].

3.4.2. Convergence threshold of energies

This parameter represents the difference of energy between two consecutive self-consistent calculation steps. If the energy difference is smaller than the defined threshold value, the calculation loop is stopped. This threshold is usually defined by default by the code (typically around 10^{-4} eV), and it works for standard calculations. However, this value should be decreased for some specific cases such as 2D materials and phonons, (among others). This threshold is set for the whole simulation domain that contains N_{atom} atoms. Therefore, we recommend that E_{total}/N_{atom} should be no larger than 10^{-5} eV/atom for electronic structure calculations.

3.4.3. Convergence threshold of forces

This parameter determines the limit of the forces felt by all atoms in the structure. In most of the algorithm packages, this parameter is automatically defined by the code around 0.01 Å/eV. However, a very common calculation in the RS field is the calculation of the formation energy of one or more defects (see Section 4.2.1). In this case, where the symmetry of the cell is broken because one or more atoms are missing, the forces felt by the atoms around the missing atom space usually is larger than the rest of the atoms. If the force threshold is too small, the simulation time could dramatically increase, achieve a non-realistic structure, or the structure never converges. In these cases, it is important to track the evolution of those forces throughout the successive relaxation steps and reconsider the threshold according to it.

3.5. MD ensembles

MD is focused on the simulation of systems that can change over time (number of particles, volume, pressure, etcetera) when its temperature or any external field is applied. According to the characteristics of the system under study and the type of interactions between the atoms or molecules present in the system, the first step is to choose the more suitable potential (or force) field. Classical MD has been used in several works for the study of amorphous materials, ionic diffusion, etcetera, but this method is not the most convenient for the simulation of the CNFs dynamics in the study of the RS phenomena in metal-oxide materials (see Section 4.2). During CNFs formation (or destruction), many oxygen vacancies are created (or recombined), so the potential field must correctly model the generation and destruction of new chemical bonds between the atoms during the RS process. In this scenario, ReaxFF (see Section 2.2) is the most suitable force field.

In addition, it is necessary to define the system of interest. The definition of the position of all atoms, type of atoms, etcetera is similar for DFT and MD cases using VASP. However, in the case of MD, it is critical to define how the system interacts with the environment by the selection of the suitable thermodynamic ensembles and the time step since the system will change over time:

3.5.1. Thermodynamic ensembles

Simulating a completely open system (in which all possible interactions between the system and the environment are allowed) is very complex and the computation cost is prohibitive. Establishing boundary conditions is normally used to calculate the result of interest in a reasonable time. To do that, one must define the thermodynamic parameters (number of particles, temperature, pressure, enthalpy, chemical potential, etcetera) that are constant (or stable) during the simulation, reducing the degrees of freedom of the system. The group of parameters that define specific boundary conditions are often referred to as thermodynamic ensemble, and they have been well described [94, 95]. The choice of the correct ensemble depends on the system under study, the type of simulation that we are running (stabilization of the system, melting the material, cooling down the structure, etcetera), and the information that we are looking for. The thermodynamic ensembles most used in MD simulations are:

- *Microcanonical ensemble or NVE*. The system keeps constant the number of particles (N), its volume (V), and the total energy (E), hence the acronym NVE. This ensemble corresponds to an isolated system that cannot exchange heat or matter with the environment.
- *Canonical ensemble or NVT*. The system keeps constant the number of particles (N), its volume (V), and the temperature (T), hence the acronym NVT. In this case, the system can exchange heat with the environment keeping constant its temperature and volume resulting in a variation of the pressure.
- *Grand-canonical ensemble or μ VT*. The system keeps constant the chemical potential (μ), its volume (V), and the temperature (T), hence the acronym μ VT. That means the system is open and can

exchange heat and material with the environment at a constant temperature.

- *Isobaric-isothermal ensemble or NPT*. The system keeps constant the number of particles (N), the pressure (P), and the temperature (T), hence the acronym NPT. The dynamic of this ensemble is similar to the canonical one, but as the pressure is constant in this case, the volume must change to keep the temperature constant.
- *Isoenthalpic-isobaric ensemble or NHP*. The system keeps constant the number of particles (N), the pressure (P), and its enthalpy (H), hence the acronym NHP. Using this ensemble means that there is no control of the temperature of the system.

3.5.2. Time step

The choice of the timestep is a trade-off between cost and accuracy. The Nyquist sampling theorem states that, to transfer information without loss, the time steps must be half of the period of the fastest dynamic event in the system [96,97]. This fastest event usually depends on the mass of the lightest atom in the system, which usually ranges from 0.25 fs for light atoms to 2 fs for heavy atoms. Another factor to take into account is the dimensionality of the simulation. In the stability and prediction of thermal properties of 2D structures, [98,99] smaller timesteps between 0.10 and 0.25 fs must be employed to conserve the total energy. However, to use the largest time step possible, a good practice is to monitor the evolution of the constant parameter of the ensemble used. For example, using the NVE, one should monitor the conservation of energy. If during the calculation the energy changes, the time step must be reduced. This process should be repeated until finding the highest time step that allows keeping the energy constant. Note that the calculation of energy and forces are iteratively computed, and hence there is inherent numerical noise in the solution. For this reason, certain drifting of those parameters is always expected.

3.6. Limitations of the DFT and MD

RS is a dynamic phenomenon that is mainly associated with stochastic changes in the atomic or electronic structure of the switching material. From the experimental perspective, the macroscopic effect of the RS has been widely studied and characterized, but without a clear explanation of the mechanisms responsible for that behaviour at the atomic level. Both DFT and MD simulations offer a detailed microscopic description of structures and processes allowing us to predict insights into the behaviour of RS materials under various conditions. However, these simulation techniques also have limitations.

Although MD and DFT simulations allow us to calculate valuable properties of the materials and processes, the direct comparison between experimental and theoretical work may be challenging stemming from the intrinsic complexities of both realms. Some of the most important bottlenecks of this comparison are the size structure limitations, the spatial resolution, the timescale, and the complexity of the real device.

In the case of DFT simulations, its high computational cost forces us to work with small material systems of a few hundred atoms at most, far from the real device size. It is important to highlight that such computational cost of DFT simulations scales cubically with the increase in the number of atoms, so small variations in the material system have a high cost. Even though the MD simulations can work with a large number of atoms (from thousands to millions of atoms), it is still challenging and costly to access practical sizes, because although the model of the particle interactions is less complex (see Section 2), the number of interactions is higher due to the dynamic interactions between particles. This limitation forces us to study very local processes far from the combination of processes that take place during the RS at different locations of the device.

Linked to the previous limitation, the spatial resolution must be considered in order to interpret and compare the results correctly. Real materials used to have several types of defects. DFT simulations mostly use periodic boundary conditions, i.e., the simulation is done in an

infinite space where the atomic structure is periodically repeated along all directions. For this reason, large supercells are needed to minimize the interaction between, for instance, a defect and its periodic images. If the defects in its periodic image are too close, parasitic interactions can appear producing incorrect results. Moreover, localized electronic states introduced by the defects can be difficult to describe accurately using the standard DFT exchange-correlation functionals, particularly for the states involving *d* and *f* orbitals. These issues can be overcome using the hybrid functionals or DFT+U methods, however, these solutions will increase the computational demand. To avoid that, it is necessary to increase the size of the super-cell or use more accurate functionals, but it will increase the computation cost too. For this reason, it is mandatory to look for a trade-off between the computation cost and the type of defect (or other type of processes) that it is possible to simulate according to the resources available.

It is well known that any real devices are not perfect because during the fabrication process can produce some contamination, the interfaces are not completely flat at the atomic scale, etcetera, and it increases the complexity of the material system. All of these parasitic effects cannot be simulated at the same time due to the limitations mentioned above. From the DFT perspective, a possible solution is the study the effect of each parasitic effect independently considering all possible variations. This solution typically needs a large number of simulations to cover all possible configurations, but it can provide a general picture of the RS process. MD simulations are more flexible about the number of atoms that can be included in the material system but have also some limitations. As was discussed in Section 2.2, interatomic potential fields are parameterized based on usually simpler systems, their transferability to systems with different chemistries or bonding environments is limited. While more elaborate interatomic potentials, such as ReaxFF, can capture the kinetics of complex structures, their cost is typically one order of magnitude larger than the simpler empirical potentials such as Tersoff or EAM. More importantly, interatomic potentials are designed for specific atoms, hence, it might not be possible to find a suitable one for all atoms present in the samples used in experiments, especially accounting for various types of unwanted contaminants or dopants. In such cases, research may need to generate a new interatomic potential, but this process can be both challenging and time-consuming.

The dynamic nature of RS processes involves transient phenomena like filament formation and dissolution, drift and diffusion of the ions, reorganization of the crystallographic structure, etcetera. Such more complex phenomena require the use of time-dependent DFT or MD, which are also quickly limited in system size and complexity [100,101]. MD simulations, depending on the complexity of the structure and size of the supercell, may still allow us to perform simulations typically limited to time scales of picoseconds to microseconds, so if the switching process is out of this time range it cannot be accurately simulated.

4. DFT and MD simulations in RS research

In RS research, the aim of using DFT and MD simulations is usually to clarify the switching mechanism, i.e., the reversible atomic and/or electronic rearrangements that take place when an electrical field is applied. To do so, the potential movement of all the types of atoms/molecules present in the device must be analysed; that includes particles from the metallic electrodes, insulating or semiconducting RS medium, and even dopants and impurities. References [102,103] demonstrated that impurities like oxygen and hydrogen from moisture could play an important role in the switching mechanism. In general, the atomic rearrangements that play a major role in the switching are those that activate at the lowest energies.

By using the physical and mathematical concepts and methodology described in Sections 3 and 4 (respectively), articles using DFT and MD simulations in the field of RS have made around 16 different types of calculations, such as band structure (BS), density of states (DOS), and charge density (CD), among many others to characterise the RS

mechanisms. The type of calculation carried out in each article is indicated in Table 1, and in Supplementary Note 1 we provide a brief description of each one. Although these calculations are widely used in this field, it does not mean that DFT and MD could not be used to carry out other types of RS-relevant calculations that are not listed in Supplementary Note 1.

In this section, we summarize the most important studies that used DFT or MD simulations to analyse RS in different material systems. All results shown in this section can be considered as a guideline of the most important mechanisms or processes that should be considered to face a new material, device configuration, or fabrication process. According to the obtained results, other studies can be carried out to characterize the particular properties of the new material system. In this case, we divide and discuss the literature available per type of material studied: phase-change, metal-oxides, 2D, organic, magnetic, and ferroelectric. For each type of material, we describe which type of simulation has been used, which parameters have been calculated, and how that information can help to confirm or deny whether a specific type of atomic rearrangement is responsible for the RS effect.

4.1. Phase-change materials

RS in phase-change materials was first reported in the 1960s [104], and RS memories based on phase-change materials were commercialized for the first time by Intel and Micron in 2010 [105,106]. Phase-change materials are typically ternary Ge, Sn, and Te alloys, which can form an amorphous (high resistive) phase and a crystalline (low resistive) phase. The transition between the two phases is triggered by the Joule effect [107–113], which is generated by applying electrical stresses between the electrodes. The amorphization of the phase-change material takes ~10 ps [114] which is compatible with time access of the current memory technologies [115]. However, the crystallization process takes ~10 ns [115,116], which can be a constraint for some applications. Most DFT and MD studies on phase-change materials for RS applications analyse the microscopic mechanisms that control this process and its kinetics [117–133].

$\text{Ge}_2\text{Sb}_2\text{Te}_5$ compounds (GST) have shown the best performance for memory technology applications because of their high endurance [134] and high speed in the transition from amorphous to the crystalline phase (i.e., high crystallization rate) [135]. The crystallization process of GST at high temperatures is driven by nucleation, i.e., the crystallization is assisted by a certain number of square rings of atoms (or precursors) that resist the amorphization process and accelerate the crystallization [136–140]. Reference [120] described the crystallization process using MD simulations. The amorphous GST contains intrinsic 4-atoms square rings (following the structure ABAB, where A = Ge, Sb; B = Te) which act as the seed of the crystallization (green and red structures in Fig. 2a). Reference [129] demonstrated that the rings are mainly composed of slowly diffusing Te atoms that capture faster Sb atoms, while the Ge atoms have a marginal role. Fig. 2 shows the evolution of the system during the annealing process of amorphous GST at a constant temperature of 600 K. Fig. 2a-d qualitatively show how the crystal structure grows from the initial seed covering the entire simulation cell. Using the number of rings and cubes as a measure of the evolution of the process, it is possible to distinguish four different stages (identified as I, II, III, and IV in Fig. 2). In stage I (from 0 to 50 ps), some atoms form new unstable squares with random orientation. In stage II the clustering process starts with the formation of new rings without strong connections between them. In stage III, those rings start to connect between them creating new cube-shaped structures. The cube cluster grows by adding new atoms around them creating first a shield of new rings and then creating additional new cubes. In stage IV, all atoms form a rock salt structure (face centre cubic, or FCC, crystal) turning into a new metastable crystal state [141]. Reference [140] also confirms the higher stability of this new crystal state since the total energy per atom of this state is ~110 meV lower. Reference [120] repeated this simulation several

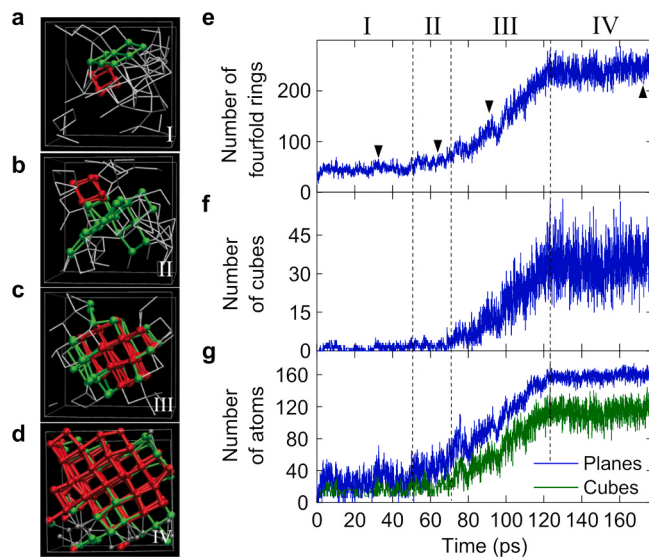


Fig. 2. **a** Formation of structural units during the incubation period I. **b** Development of ordered layer structures at the crystallization site. **c** A cube cluster and planes extending from the cluster interface. **d** Completely crystallized phase with a crystal-glass interface. **e** Evolution of the number of fourfold rings forming planes. **f** Evolution of the number of cubes, and **g** evolution of the number of atoms forming planes or cubes. The triangles in **e** indicate the time at which the a-d snapshots were taken. Reproduced with permission. [120] Copyright 2011, American Physical Society.

times using different initial amorphous states. They obtained different crystallization velocities due to the stochastic nature of the process but following the same four stages confirming the consistency of the process. Similar simulations carried out by other authors confirm the described dynamics [129,139,140].

This model of phase-change materials analysed the chemical order. In the GST crystal, the Ge and the Sb tend to be connected to Te atoms [142,143]; hence, the number of Te-Te, Ge-Ge, Sb-Sb, and Ge-Sb bonds — usually named wrong bonds — can be used to quantify the crystallinity level during the switching process. Fig. 3 shows the evolution of the number of rings and wrong bonds during the GST crystallization process at different temperatures, calculated in reference [139]. The

number of wrong bonds decreases during the process, achieving a stable value at the end of the process. Hence, structural ordering is always accompanied by chemical ordering. Reference [120] demonstrated that most of the remaining wrong bonds are located on the surface of the crystal, confirming the stability of the crystal.

This square ring generation dynamics can be modified by any alteration of the number and the geometry of the rings initially present in the material. Reference [128] studied the type of rings in different GST compounds ($\text{Ge}_2\text{Sb}_2\text{Te}_5$, $\text{Ge}_8\text{Sb}_2\text{Te}_{11}$, GeTe , $\text{Ge}_2\text{Sb}_1\text{Te}_2$, $\text{Ge}_4\text{Sb}_1\text{Te}_2$, $\text{Ge}_7\text{Sb}_1\text{Te}_2$; see Fig. 4). Stable GST mainly forms square rings as expected (Fig. 4a). As the content of GeTe increases (Fig. 4b-c), the 5-atoms rings become more predominant and comparable to the 4-atoms ring. Those new rings also follow the pattern ABAB, so it does not change the stability or the kinetics of the crystallization process [128]. In Ge-rich configurations (Fig. 4e-f), the 5-atoms rings are the predominant. However, these rings do not follow the ABAB pattern due to the excess of Ge atoms, creating local instabilities that reduce the crystallization rate [144,145].

Dopants such as C [119], Ag [123], Y, Hg, Sc [127] have been used to tune the kinetics of the crystallization process of GST alloys, as they can modify the Te-Sb and Te-Ge interactions. Reference [123] demonstrates that the crystallization process is faster if the GST compound contains Ag dopants, as the Ag atoms can substitute some Ge atoms in the square rings.

Reference [126] studied the crystallization process of GST when two different pulse stress protocols were applied. For simplicity, pulses of temperature were considered (see Fig. 5), which are equivalent to the temperature increase produced by the Joule effect after applying and voltage pulse in a real device. In the first pulse stress protocol all applied pulses have the same duration (50 ps), but the amplitude increases (Fig. 5a); and in the second one the amplitude of the pulses is constant (700 K), but their duration progressively increases (Fig. 5b). Both simulations start from the same amorphous structure that contains a certain number of square rings or precursors (see state A in Fig. 5c). The simulations indicate that the second protocol induced a more homogeneous crystal structure in a shorter time.

4.2. Metal-oxides

RS in metal-oxides started to become popular in the early 2000s [16, 17,146–148], and nowadays metal-oxide RS memories are being commercialized by different companies like Fujitsu and ST-Microelectronics as non-volatile electronic memory, and others like IBM, TSMC, and Weabit Nano are also exploring their use for hardware implementation of artificial neural networks. The switching mechanism can be related either to the formation of oxygen vacancies in the metal-oxide or to the penetration of foreign metallic atoms from the adjacent electrodes. Although many research articles claimed the observation of up to 10^{12} cycles in a champion metal-oxide RS device (often using unreliable characterization protocols [149]), the truth is that companies commercializing this technology never promise an endurance of more than 10^6 cycles [150], meaning that reliability improvements are required.

4.2.1. Oxygen vacancies formation and migration

This type of RS mechanism takes place when the electrical field applied mostly breaks atomic bonds in the molecules that form the RS medium. The movement of such atoms leaves behind atomic vacancies that serve as centres for electron trapping and de-trapping, and that can cluster to effectively form a conductive nanofilament (CNF) across the RS medium connecting the electrodes. This mechanism often involves local oxidation-reduction reactions provoked by the migration of ions during the application of an electrical field. This type of RS mechanism has been observed in multiple metal-oxides (HfO_2 [151–161], NiO [74, 162–164], TiO_2 [164–167], V_2O_5 [168], $\text{TaO}_2/\text{Ta}_2\text{O}_5$ [169,170], and SrZrO_3 [171]) coupled with stable electrodes (Pt, TiN, or W), and the RS

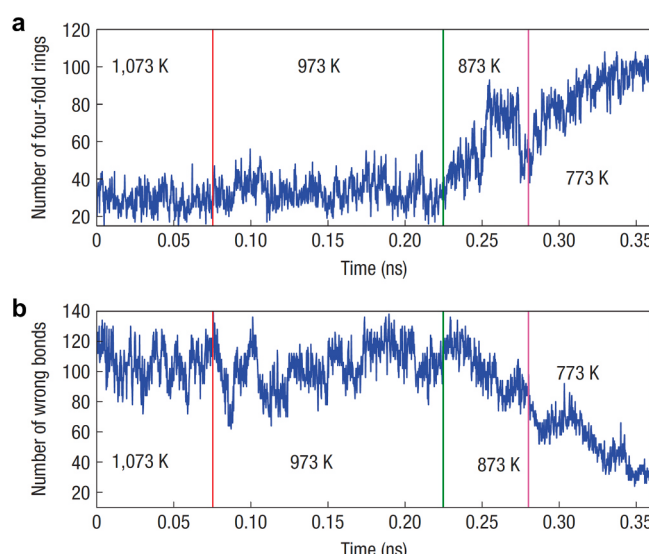


Fig. 3. The evolution of **a** the number of near-regular four-fold rings and **b** the number of wrong bonds during the simulated crystallization process. Reproduced with permission. [139] Copyright 2008, Nature.

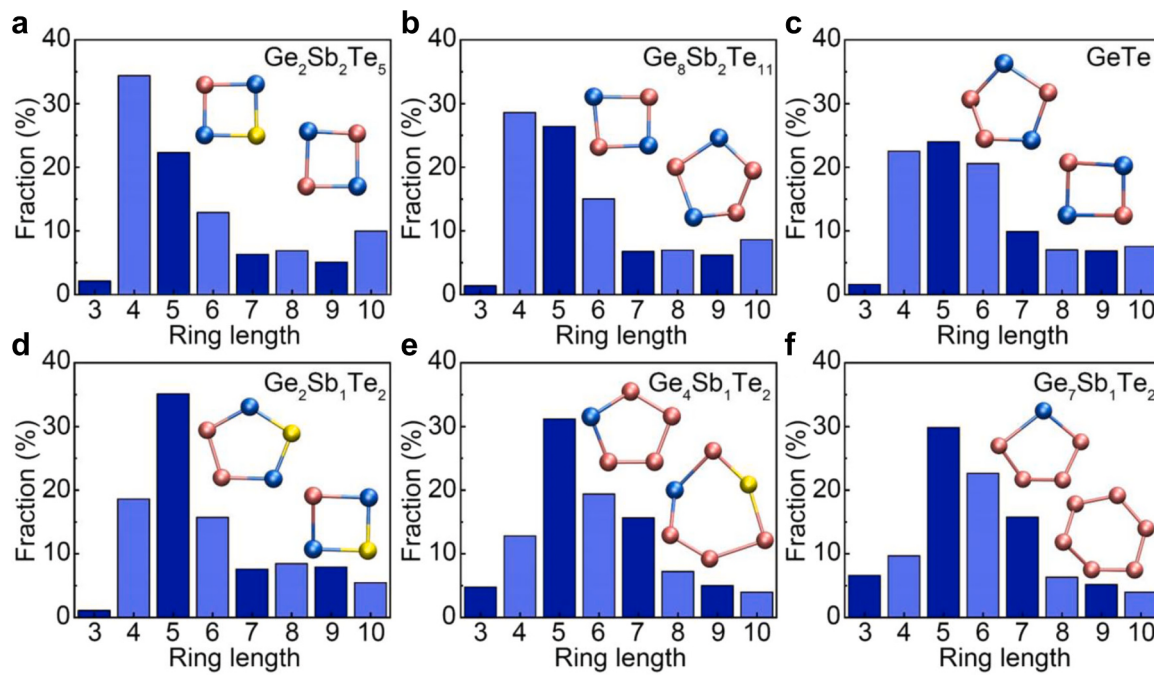


Fig. 4. Primitive ring statistics. The distribution of primitive rings for six amorphous alloys, including stoichiometric GST **a** $\text{Ge}_2\text{Sb}_2\text{Te}_5$ and **b** $\text{Ge}_8\text{Sb}_2\text{Te}_{11}$, **c** GeTe, and off-stoichiometric GST **d** $\text{Ge}_2\text{Sb}_1\text{Te}_2$, **e** $\text{Ge}_4\text{Sb}_1\text{Te}_2$, and **f** $\text{Ge}_7\text{Sb}_1\text{Te}_2$. The insets show typical ring fragments in respective amorphous models. Ge, Sb, and Te atoms are shown in red, yellow, and blue, respectively. Reproduced with permission. [128] Copyright 2021, Elsevier.

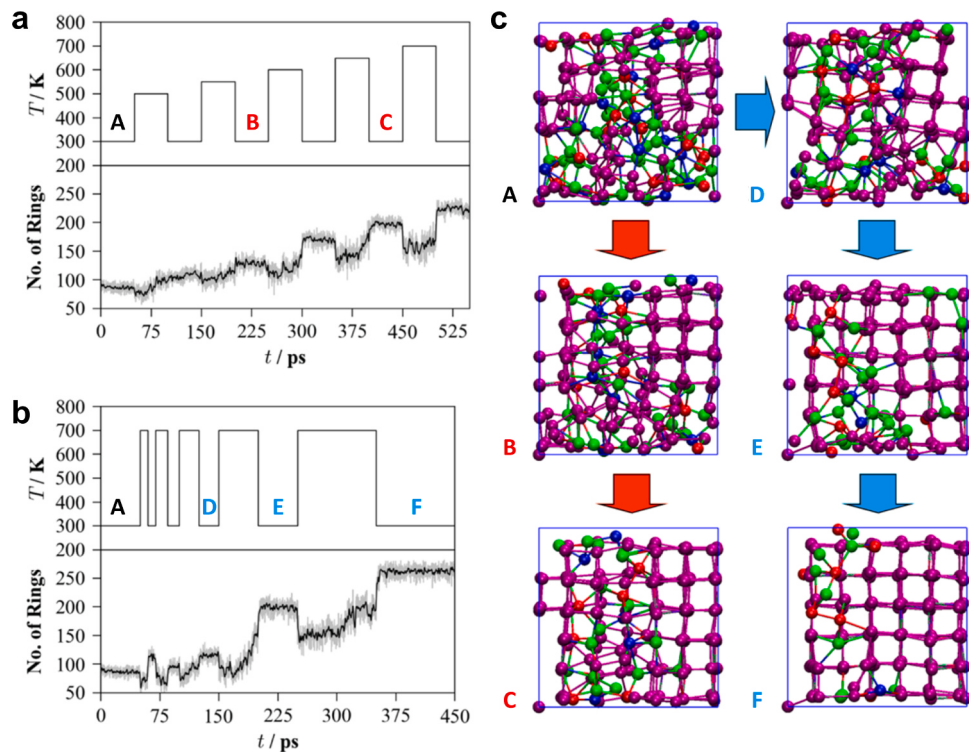


Fig. 5. **a** Evolution of the number of rings (bottom graph) when a sequence of temperature pulses is applied with a constant pulse duration of 50 ps and increasing the amplitude from 500 K to 700 K (top graph). **b** shows the evolution of the number of rings applying pulse with a constant amplitude of 700 K and variable duration. The snapshots of the GST structure in several states of the simulation are shown in **c**. The states are identified as A, B, C, E, and F. Atoms forming parts of four-fold rings are coloured purple, and the colour coding of the other atoms is as follows: Ge, blue; Sb, red; Te, green. Reproduced with permission. [126] Copyright 2015, Nature.

community often refers to it as valence change RS [16].

In all these metal-oxides the formation of oxygen vacancies occurs at energies much lower than the metal vacancies, and hence they are

responsible for the RS effect. It has been demonstrated by calculating the formation energy of oxygen vacancies by DFT simulations using the following equation:

$$E_{FE}(nV_x^q) = E(nV_x^q) - E(\text{bulk}) + n\mu_x + nqE_F \quad (13)$$

where n is the total number of vacancies, q is the charge of the vacancy (in general, $q = 0$ for oxygen vacancies), and $E(nV_x^q)$ and $E(\text{bulk})$ are the ground energy of the structure with n vacancies and pristine, respectively. E_F is the Fermi energy referenced to the valence-band maximum of the defect-free structure, and μ_x is the chemical potential of the vacancy. For oxygen vacancies, this last parameter can be calculated as half of the ground state energy of an oxygen molecule, or $\mu_o = 0.5 \cdot E(O_2)$. Once having the vacancy formation energy, it is possible to predict the most probable configuration or shape of the oxygen vacancy cluster according to the most stable state, i.e., the cluster configuration that requires the lowest formation energy. For example, in reference [165] it was shown that the [001] direction is more favourable for the growth of an oxygen-vacancies-based CNF in TiO_2 . This observation implies that the regions surrounding an oxygen vacancy are prone to form new vacancies. That is because this configuration of oxygen vacancies favours the Ti 3d orbitals overlap, decreasing the energy of the system [153,172–174]. Similar studies have been done for other materials such as HfO_2 [155] and SrZrO_3 [171] confirming that the oxygen vacancies tend to form clusters also in these materials. The work in reference [155] is especially interesting because the authors calculated the charge distribution for several configurations of oxygen vacancies clusters with the HfO_2 film. Their results suggest that only some configurations can form a stable CNF. The formation energies of the first oxygen vacancy for several materials (calculated by DFT) are displayed in Fig. 6a, which shows that the energy is in the range of 4–4.5 eV for most cases. For most materials, the energy to form the second vacancy is either similar or slightly lower than for the first vacancy, resulting in an increasing cumulative formation energy with the number of vacancies (Fig. 6b).

Once demonstrated the capability of the oxygen vacancies formation in the metal-oxide materials that can generate CNFs, DFT simulations have been used to study their electrical properties by the comparison of the density of states (DOS) of band structure (BD) of the material with and without vacancies. This type of calculation can help to discern whether the oxygen vacancies form new states inside the band gap, which is the precise result confirming or denying the presence of a CNF. For example, in reference [163] the authors demonstrated that the accumulation of oxygen vacancies along one specific direction progressively creates a CNF in NiO as Fig. 7 shows. According to their calculations, the band gap of the pristine NiO is 3.2 eV (see Fig. 7b). Fig. 7c-f shows the DOS removing from 1 to 4 nearest-neighbours oxygen vacancies. Those vacancies create additional states inside the band gap, which creates a CNF and allows hopping conduction. The green dashed line is the partial DOS (or PDOS) of one Ni atom located far from the

oxygen vacancies cluster (yellow atom in Fig. 7a). This line does not show any state available inside the forbidden region which confirms that the influence of the vacancies is a local effect supporting the idea of a local CNF.

In reference to [171], the authors calculated the DOS and BS of SrZrO_3 introducing several oxygen vacancies and demonstrated that those vacancies created additional states close to the valence band (see Fig. 8a). The PDOS calculated demonstrates that those additional states come from the 4d orbitals of Zr (see Fig. 8b). Calculations of the charge distribution in the crystal (in the plane where the oxygen vacancies are located) show a high density of electrons (red colour in Fig. 8c) trapped around the path generated by the vacancies. In these conditions, these electrons could easily be transported through the oxygen vacancy path if an external electric field is applied.

Reference [74] carried out a similar simulation but in an $\text{Ag}/\text{NiO}/\text{Ag}$ system, but in this case including the electrodes. The results (see Fig. 9b) indicate that the CNF effectively connects both electrodes. References [74,155,156,163,165] carried out similar DFT calculations to confirm valence change RS in TiO_2 (see Fig. 9a), NiO (see Fig. 9b and inset of Fig. 7), and HfO_2 (see Fig. 9c).

In order to improve the RS features (ON/OFF ratio, retention, power consumption), several studies suggest that introducing dopants during the fabrication process may help in this goal [175–179]. One of the effects of doping insertion is the reduction of the formation energy of the oxygen vacancies close to the dopant atoms [175–177,180]. In HfO_x cation dopants significantly modify the formation energy of the nearby vacancies [181] but depending on the properties of the dopant (valence, atomic radius, magnetization) the formation energy of the oxygen vacancies can increase, decrease, or stay constant [182]. By using DFT, it was demonstrated that in HfO_x [183] the substitutional site dopant is more stable as more isovalent is with the replaced atom. Based on the number of valence electrons, three types of dopants could be defined: Hf-like, p-type, and n-type (see Fig. 10). The formation of positive vacancies is more probable during the electron charge transfer to the dopant. For this reason, the strong p-type and n-type favourably change the formation energy of new vacancies in this condition but also change the switching behaviour. Hf-like dopants reduce the formation energy without significantly changing the switching dynamics, the effect of anions on the formation of oxygen vacancies formation is generally weaker, and the type of dopant atoms is less relevant. It promotes some changes in the switching dynamics and the generation of more stable CNFs [183]. Similar studies were done for other materials such as CeO_2 [178,184], TiO_2 [179], TaO_2 [185,186], and ZrO_2 [29].

The electrodes used on this type of device are called inert electrodes because there are no ion migrations into the insulator, due to their high bonding energy. However, some publications suggest that there is

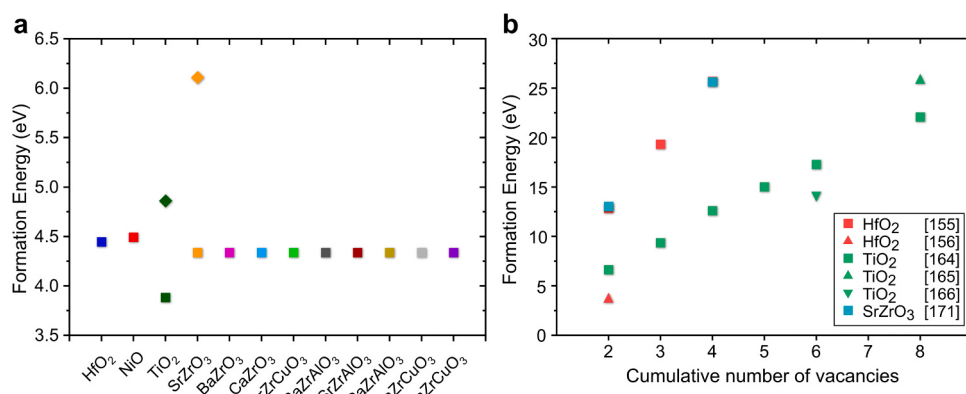


Fig. 6. **a** Calculated formation energy of the first oxygen vacancy for HfO_2 [156], NiO [162], TiO_2 square [164] and diamond [166], SrZrO_3 square [290] and diamond [171], BaZrO_3 , CaZrO_3 , SrZrCuO_3 , BaZrAlO_3 , SrZrAlO_3 , CaZrAlO_3 , CaZrCuO_3 , and BaZrCuO_3 [290]. **b** Calculated formation energy of the secondary oxygen vacancies for HfO_2 [155,156], TiO_2 [164–166], and SrZrO_3 [171].

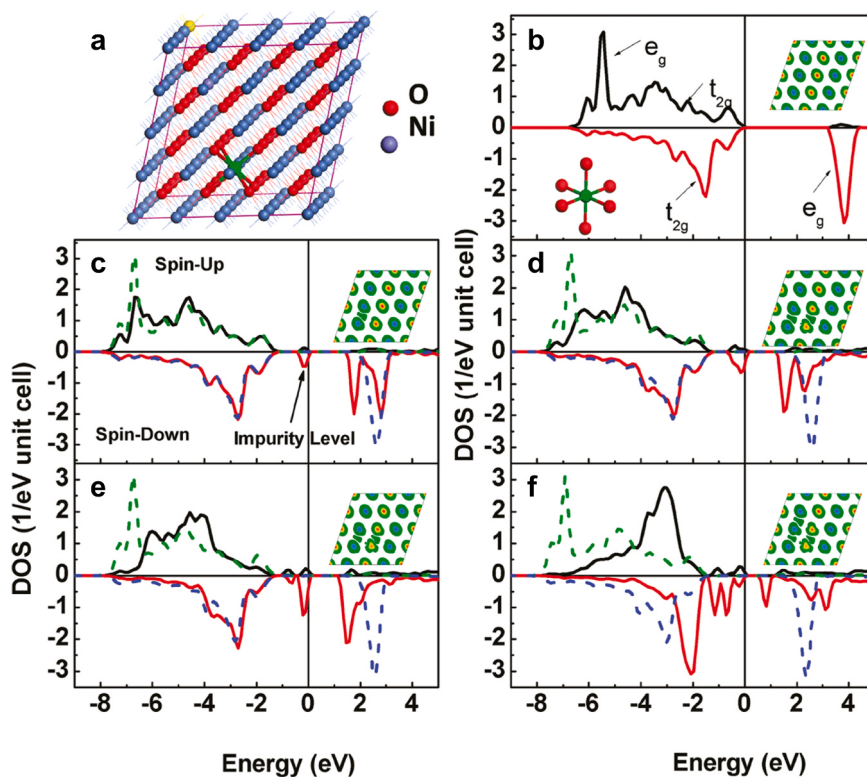


Fig. 7. **a** Schematic of the NiO supercell used for the simulations. **b-f** PDOS (red and black solid lines) of Ni atom highlighted in green in the supercell with 0, 1, 2, 3, and 4 nearest-neighbour oxygen vacancies, respectively. The green dashed lines represent the partial density of states of the Ni atom marked in yellow in panel a. Reproduced with permission. [163] Copyright 2011, American Chemical Society.

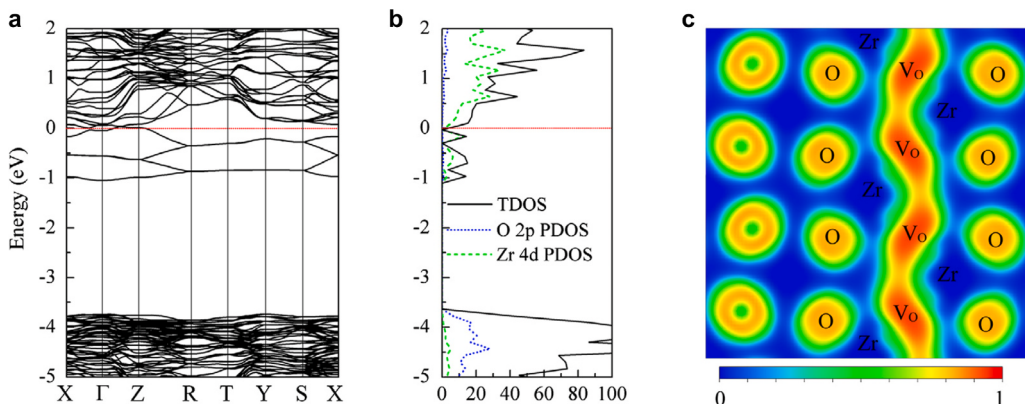


Fig. 8. The calculated **a** BS, **b** DOS, and **c** ELF contour plots projected on the (001) plane of SrZrO₃ for the Vo-row models. Reproduced with permission. [171] Copyright 2013, Elsevier.

always (in some degree) drift-diffusion of metallic ions from the electrodes to the insulator [30,182,187]. Although the number of drifted ions may not be enough to form a CNF and valence change may still be the dominant RS mechanism, such drifted ions can act as dopants changing the formation energy of the oxygen vacancies (in one direction or another), as previously discussed.

Apart from energy formation, the kinetics of the oxygen vacancies play an important role in the formation and disruption of the CNF. This is often studied via DFT simulations by calculating the energy barrier that oxygen vacancies must overcome to drift from one position to another in the material. By using the nudged elastic band (NEB) method [188], reference [163] calculated the migration energy of an oxygen atom (Fig. 11) when: i) the atom moves from its initial location to the first nearest-neighbour oxygen vacancy, breaking the oxygen vacancy

cluster (see black arrow); and ii) the atom moves in the opposite direction forming an oxygen vacancy cluster (see red arrow). The results show that the interaction between vacancies decreases the energy barrier to create a cluster of vacancies and increases the energy necessary to break this cluster. This result (together with the formation energy results showed previously) demonstrates that it is more probable to create vacancies close to other vacancies and that oxygen vacancies clustering can be stable. Only when a high enough energy is applied to the system (either by applying an electrical field or by the Joule effect) the cluster of oxygen vacancies can be broken.

4.2.2. Metal penetration from the electrodes

This type of RS mechanism takes place when the electrical field provokes the migration of the metallic ions from one of the electrodes

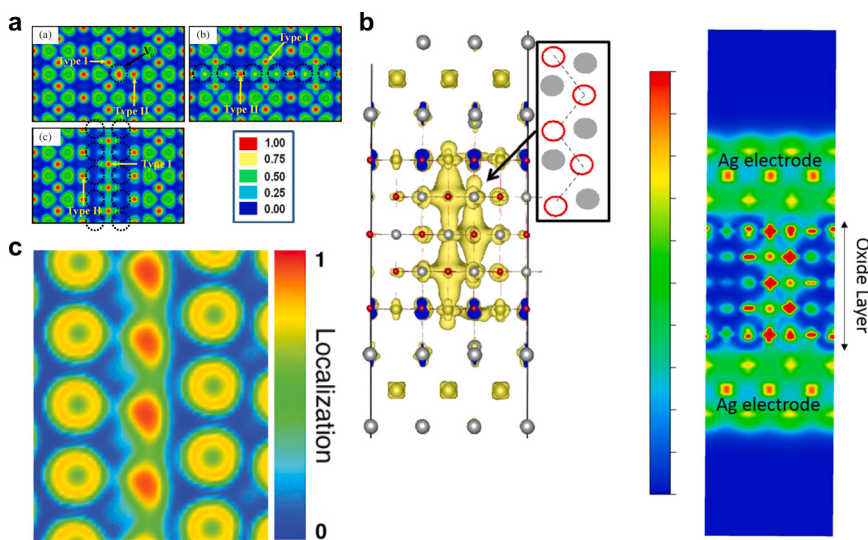


Fig. 9. **a** ELF of (a) isolated vacancy, (b) [110] chain with six vacancies, and (c) [001] chain with eight vacancies. The dotted circles represent the position of oxygen vacancy. **b** Partial charge-density distribution for CF of 5 Vo in an Ag/NiO/Ag structure. The charge is delocalized in the Vo filament connecting both electrodes. **c** ELF of a Vo filament in HfO₂. Reproduced with permission **a** [165] copyright 2010, IEEE, **b** [74] copyright 2018, American Chemical Society, **c** [156] copyright 2016, IEEE.

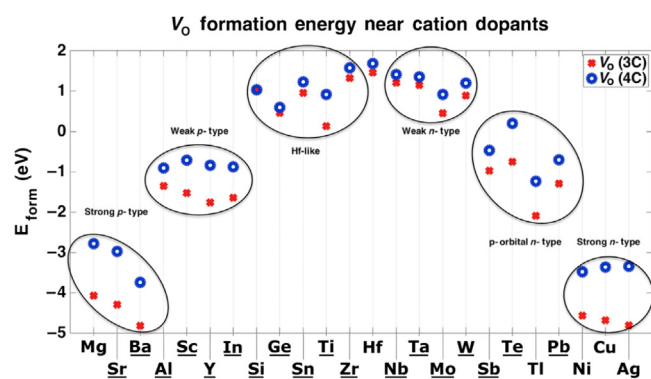


Fig. 10. Formation energy V_o's next to cation substitutional dopant defects. Reproduced with permission. [181] Copyright 2017, American Physical Society.

into the RS medium to form the CNF [16]; hence, this type of device uses electrodes made of active metals (Cu, Ag, Al, etcetera) that have a higher diffusivity [189–191]. For this reason, DFT and MD studies of these devices require the electrode to be present in the structure simulated and the interface electrode-RS medium must be considered.

In these types of devices, the generation and dissolution of the CNFs take place by the diffusion of the metal ions from the electrode to the insulator driven by the external electric field. In [31], the generation of the first CNF (made of Cu ions) in a pristine a-SiO₂ layer (forming

process), the breaking of this filament (reset process), and the formation of the CNF again (set process) were simulated using reactive MD (see Fig. 12). Under an external voltage stress, Cu ions progressively penetrate the insulator layer creating a stable cluster of metal atoms along the direction of electric field (see Fig. 12a-c). Once one of these clusters come into contact with the inert electrode, the structure loses its charge, opening a conductive channel between the electrodes, i.e., creating the CNF shown in Fig. 12d. When the voltage is applied on the opposite bias, the Cu ions are pushed away from the inert electrode breaking the CNF (see Fig. 12e), i.e., the reset process takes place. During the set process (the same voltage bias as in the forming process is applied), the residual CNF is suppressively destroyed (Fig. 12f-g), and all these residual ions are able to rapidly create a new CNF (Fig. 12h). This unexpected result could be an artefact produced by the boundary conditions of the force field used, but it supports the high cycle-to-cycle variability of the RS devices.

The interface between the active metal and the insulator may also play a role in the RS process and its stability. TiO₂ is widely used for this type of device as a switching medium. It is relatively easy to reduce because Ti-O bonds are weak [192], and the resulting stoichiometry variations can affect the nature of the interface with the metal electrode. In addition, the reduction of this oxide is further accentuated when placing an adjacent electrode. Reference [30] calculated the reduction energy for TiO₂ and Ag/TiO₂, obtaining 4.3 eV and 3.84 eV per oxygen atom, respectively. Similar observations have been made in Pt/TiO₂ [193] and Pd/MgO [194]. The reduction of the TiO₂ at the interface with Ag increases the adhesion energy of the electrode from 25 meV/Å²

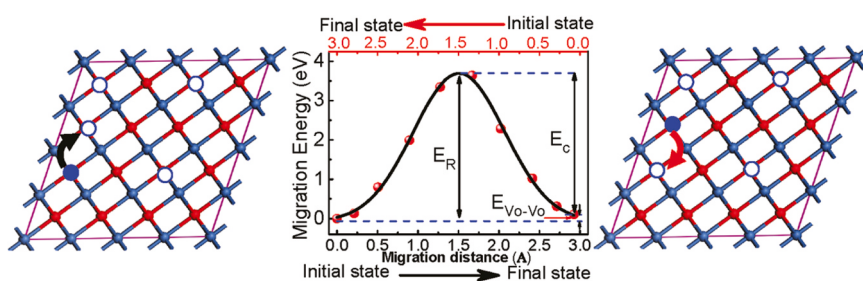


Fig. 11. Calculated migration energy of an oxygen atom (blue filled circle) when it moves to the first nearest-neighbour oxygen vacancy breaking the Vo cluster (black arrow), and to form the Vo cluster (red arrow). Reproduced with permission. [163] Copyright 2011, American Chemical Society.

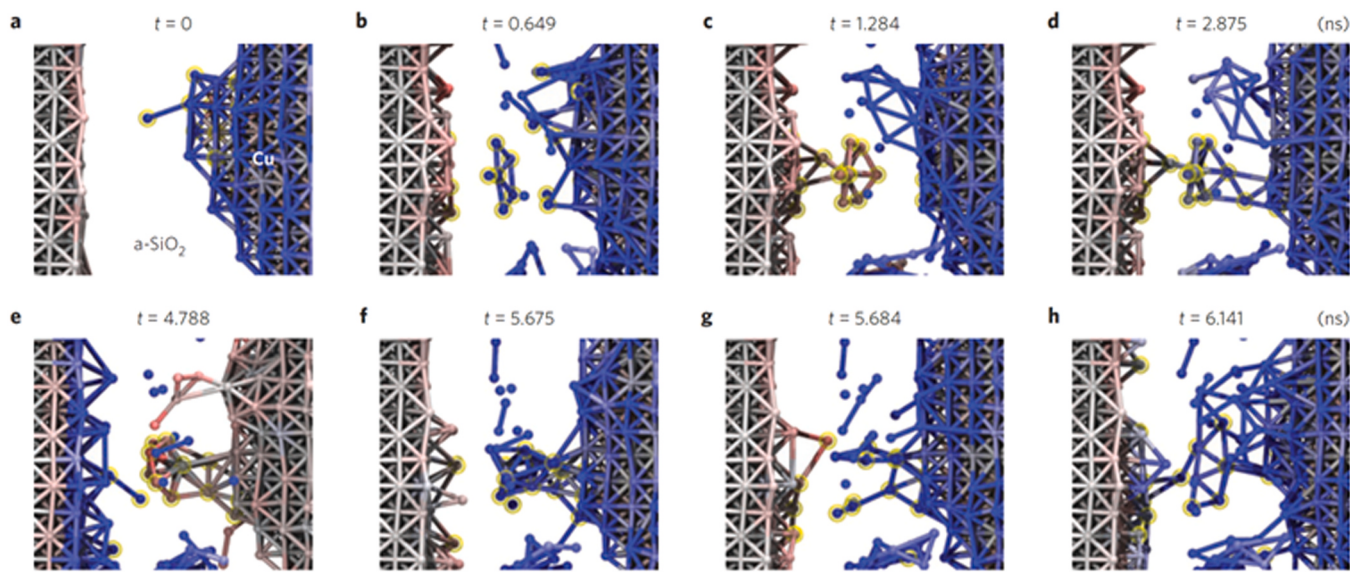


Fig. 12. a-h Frames generated by the reactive MD simulation of the forming, reset, and set process in a Cu/a-SiO₂ device. Reproduced with permission. [31] Copyright 2015, Nature.

for Ag/TiO₂ to 62.3 meV/Å² for Ag/TiO_{2-n} increasing the structural stability of the device. Furthermore, as a result of the TiO_{2-n} reduction process the residual oxygen reacts with the Ag atoms partially oxidizing some of them. This interfacial AgO_n layer favours the generation of silver ions which can diffuse into the oxide triggering the diffusion of ions. Those free Ag ions are also attracted by the oxygen vacancies generated in the oxide during the reduction process, becoming the diffusion channel of the ions [30].

After overcoming the electrode/oxide interface the metallic ions tend to occupy the interstitial space between the atoms (rather than substitute the metallic atom of the oxide) because that is energetically more favourable [29,30]. That is because there is a correlation between the valence electrons, the atomic radius of the inserted ions and the total energy of the system. For example, in the case of TiO₂, the energy cost to remove one Ti atom and replace it with one Ag ion is 22.6 eV [30] which is huge, making this process very improbable. In the interstitial space, however, the distortion produced by the external ion in the structure is lower, so the system is more stable [29]. In [195] diffusion of Ag ions into a-SiO₂ during the RS process was studied. It demonstrated that this insulator tends to form silica rings containing three to nine Si atoms. This accumulation of ring-shaped atoms also creates empty spaces through which the Ag atoms can diffuse. The analysis of the trajectories of the Ag ions during the forming process using MD simulations

demonstrates that the ions preferentially move through the larger rings. Fig. 13 shows the result of an MD simulation of the CNF generation process. The Ag ions (grey spheres) use the larger rings of 8-silica atoms (green ring in Fig. 13b) and the 6-silica atoms (blue ring in Fig. 12b) to split the CNF into two new branches. That means the growing path followed by the CNF is determined by the direction of the applied electric field and by the location of the larger rings. It is another result that explains the device-to-device variability of the RS device since the intrinsic composition of the insulator material also plays a role in the geometry of the CNFs.

4.3. Two-dimensional layered materials

2D layered materials are formed by layers of atoms covalently bonded in-plane, and in which the layers/planes attach to each other by van der Waals forces. RS has been observed in multiple 2D layered materials: (i) semiconductors like transition metal dichalcogenides (TMD), including molybdenum disulfide (MoS₂) [32,196], molybdenum diselenide (MoSe₂) [197,198], tungsten disulfide (WS₂) [199], and tungsten diselenide (WSe₂) [199,200]; and (ii) insulators like graphene oxide (GO) [201,202] and hexagonal boron nitride (h-BN) [203–206]. In most 2D materials the electrical stresses can trigger the formation of intrinsic vacancies (e.g., sulphur in MoS₂) or the penetration of metallic

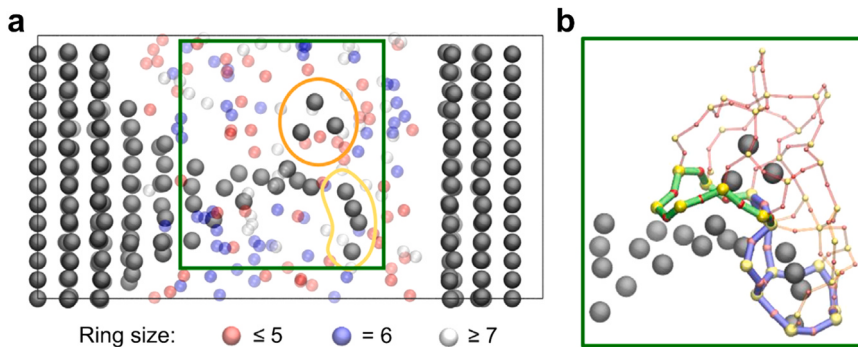


Fig. 13. a) Intermediate frame of the CNF growth process in an Ag/a-SiO₂/Ag device simulated by MD. The Ag ions (grey spheres) form the CNF that crosses the insulator layer composed of silica rings (red, blue, and white spheres). b) Zoom in of the green rectangle in a). The CNF is split into two branches (the upper is the orange circle in a and the lower is the yellow cycle in a) following the location of the larger rings highlighted in green (8-silica ring) and blue (6-silica ring). Reproduced with permission. [195] Copyright 2023, Elsevier.

ions from the active electrodes, and both phenomena could be the onset of the RS phenomenon.

The formation of intrinsic vacancies can play a different role depending on the 2D material analysed and its thickness. In monolayer 2D materials sandwiched by two metallic electrodes, the formation of a vacancy produces a physical pinhole and triggers an effective electrical connection between the electrodes [207,208]. Reference [207] demonstrated – by the calculation of the DOS – that the presence of a vacancy of nitrogen in monolayer h-BN shifts the Fermi level close to the conduction band, reducing the barrier between both electrodes and increasing the tunnel conduction. When the 2D material is thicker and multiple layers are stacked, the formation of vacancies still can tune the conductivity of the entire RS cell, but in more or less degree depending on the atoms that form the 2D material and its bandgap [209,210]. Reference [210] demonstrated that this effect is also present in 40 nm HfS₂, but it is less predominant than in the case of a monolayer material. According to their results, pristine HfS₂ is a weak p-type semiconductor with a band gap of 1.28 eV and 0.71 eV between the Fermi level and the bottom of the conduction band, (see Fig. 14c, e). However, the presence of one V_S (sulphur vacancy) becomes this material a highly doped n-type

semiconductor since the distance between the Fermi level and conduction band is almost 0 eV (see Fig. 14d, f). However, this result was calculated using the PBE functional which underestimates the band gap. So, this result is correct from the qualitative point of view because experimental results suggest that this material shows a weak n-type behaviour [211]. In addition, the formation of vacancies can also leave behind a metallic path (e.g., sulphur vacancies formation in MoS₂ leaves behind a conducting Mo path), which triggers the LRS [212,213]. This behaviour is observed when using stable electrodes with high cohesive energy and low diffusivity (such as Pt, for instance), similar to what happens in metal-oxides (see Section 4.2). This type of vacancies-based RS has been also observed in multilayer graphene oxide [212,213], as the motion of oxygen can leave behind a conductive graphene path. Despite the out-of-plane resistance of graphene is not as low as that of a metallic filament, the resistance ratio with and without oxygen atoms can reach several orders of magnitude [203]. On the contrary, in multilayer h-BN, the formation of boron or nitrogen vacancies produces a local increase of conductance, but the formation of highly conductive LRS still requires metal penetration (what stays behind the boron vacancies is nitrogen, which is not enough conductive to trigger the LRS)

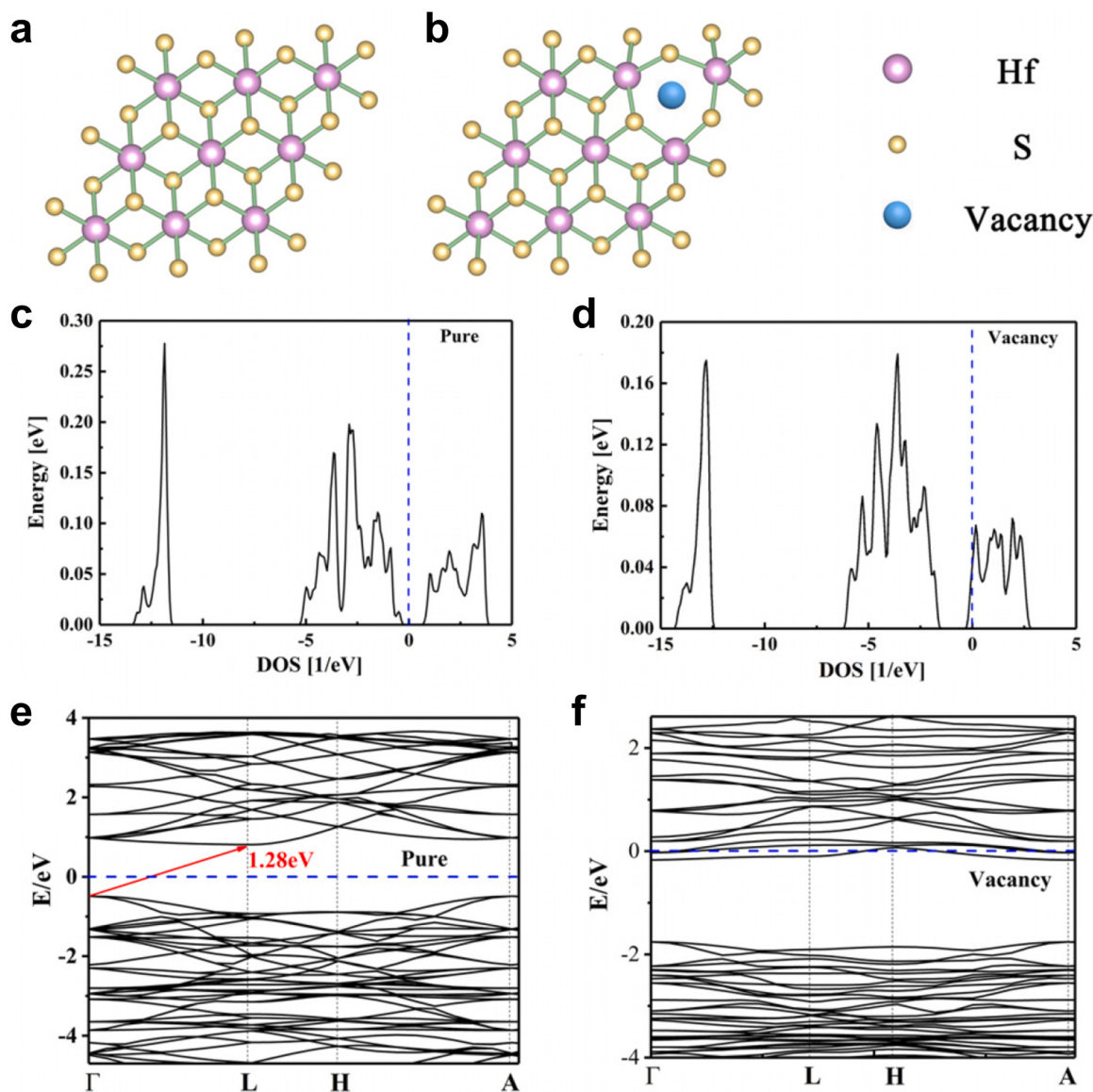


Fig. 14. **a** and **b** Optimized crystal structure of pristine and V_S HfS₂. DOS for **c** pristine HfS₂ and **d** V_S HfS₂. Energy band diagrams for **e** pristine HfS₂ and **f** V_S HfS₂. The dashed blue lines in c, d, e, and f represent the position of the Fermi level. Reproduced with permission. [210] Copyright 2020, American Institute of Physics.

[207,214]. Such conclusions have been extracted via cross-sectional transmission electron microscopy coupled with electron energy loss spectroscopy and energy dispersive X-ray spectroscopy, although DFT or MD simulations were not employed. Hence, complementing such type of conclusions via DFT and/or MD simulations could further clarify the role of vacancy formation in the RS in these 2D layered materials.

It should be noted that, in all those 2D layered materials, the formation of vacancies is much more likely to happen at/near the local defects (either native or introduced during material processing, such as transfer or metal evaporation). In reference [215] it was calculated, using both DFT and MD, that the energy to form a boron vacancy in crystalline h-BN is ~ 10 eV, while this is reduced to ~ 7 eV and ~ 3.5 eV if one or two vacancies are present. Moreover, the energy to form vacancies can drastically decrease (<1 eV) if the material contains some amorphous defective regions embedded in the crystalline structure [215].

If the metallic electrodes employed have a higher diffusivity (e.g., Ag, Au, Cu, etcetera), ions of those metals could also penetrate in the 2D layered material and trigger the LRS [19,30,32,33,207,216–219]. Reference [19] used DFT simulations to calculate the energy needed to extract one Au atom from the electrode in an Au/MoS₂ interface, obtaining a value of 3.8 eV. The extracted Au ion at the interface is unstable, and if the adjacent MoS₂ film contains any vacancy, the Au ion will tend to bond there because the binding barrier Au vacancy is very small [19,30]. Fig. 15b shows the binding energy of Au, Au⁺¹, and Au⁻¹ for MoS₂ and different 2D materials and displays that Au and Au⁺¹ are the most probable states. The negative value of this energy means that the process is exothermic, that is, energetically favourable. If there is no vacancy in the MoS₂ film near the extracted Au ion, the Au ion may diffuse until it reaches a vacancy. In this case, DFT or MD simulations can be used to calculate the diffusion path. In reference [19] the authors estimate that the energy barrier for the ion diffusion between the initial bond with the MoS₂ surface state to the sulphur vacancy is lower than

0.1 eV. This suggests that this step is spontaneous at room temperature or under an external electrical field. Once the ions achieve a location close to the sulphur vacancy, the absorption process takes place. According to the result shown in Fig. 15d, Au and/or Au⁺¹ can easily be absorbed by the sulphur vacancy because the energy barrier is only 0.18 eV. Moreover, the binding process is energetically favourable releasing an energy of around 1.72 eV. On the contrary, the energy cost of the opposite process is around 1.89 eV, indicating the non-volatility of this process.

Once the metallic ion from the electrode overcomes the interface with the 2D material it is important to analyse through which locations of the space are more prone to diffuse [32,33]. References [207,218] calculated the formation energy of one Au ion considering different locations of the space in Au/h-BN/Au and Au/MoS₂/Au RS devices. Fig. 16b-e shows four different interstitial locations for the Au ions in a monolayer h-BN sheet without defects, together with the formation energy of each process. The low negative formation energy indicates that those configurations are low probable. On the contrary, if the metal ion occupies the space left by the boron, nitrogen, and boron-nitrogen vacancy (Fig. 16f-h) the structure is more stable. DFT simulations also allow the analysis of the migration of metallic ions across the RS medium to form the CNF. Reference [207] calculates the energy barrier that the Au ions must overcome to cross monolayer h-BN. The high barrier in the case of the perfect h-BN (10.63 eV) confirms that there needs to be a certain number of defects in the 2D material stack to create a CF. On the contrary, if there is one boron vacancy the energy barrier height is 0.83 eV, and when there is one boron vacancy with one adjacent nitrogen vacancy the energy barrier is 0.09 eV. In the second case, it is possible to consider that there is a hole in the layer because the Au ion can flow across the space left by both defects without any resistance. The entire process of the formation of the CNF in this material was simulated using MD in reference [33] (see Fig. 17). In this case, a custom ReaxFF has been used to simulate the application of an external electric field.

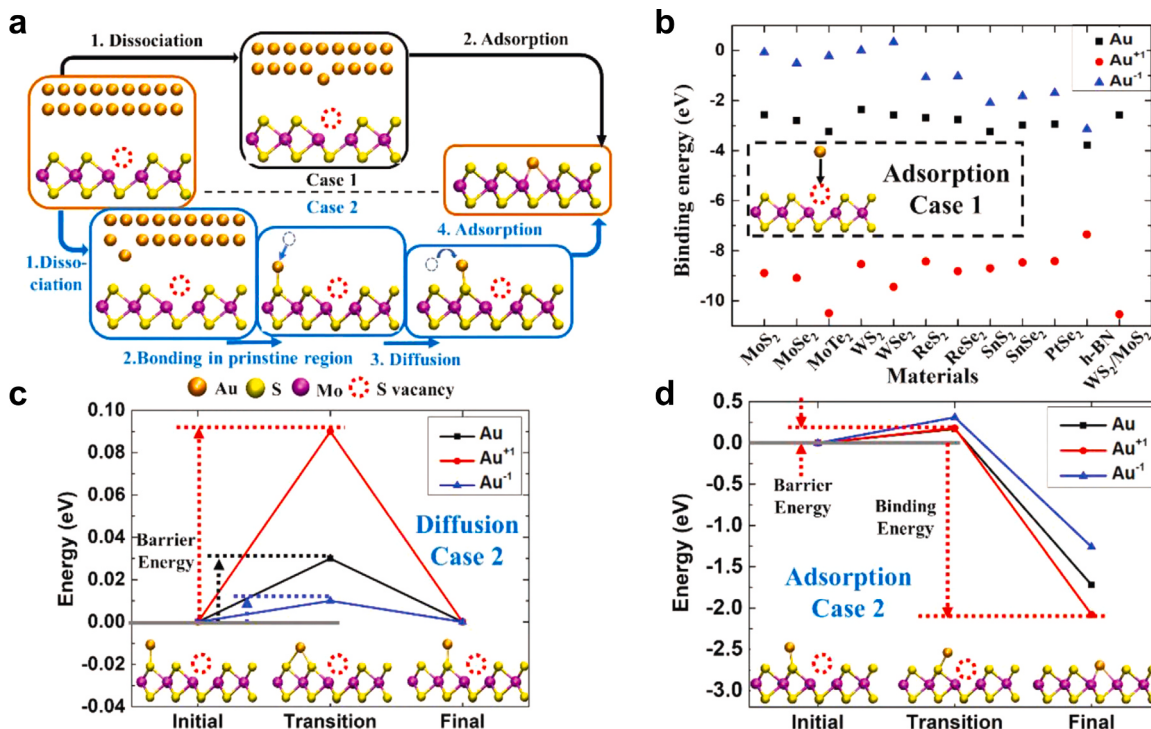


Fig. 15. **a** Schematics of different states in the DDA model. Case 1 corresponds to the direct adsorption of Au in a vacancy and in Case 2 the Au first bonds to the pristine region followed by diffusion across the surface for adsorption into a vacancy. **b** Adsorption (or binding) energy of Au on a vacancy site for a dozen different 2D materials (Case 1). **c** Calculated diffusion pathway and barrier energy of the Au atom/ion from the top of one S atom to the top of a neighbouring sulphur atom in the pristine region of the MoS₂ surface (Case 2). **d** Calculated adsorption pathway and barrier and binding energies of an Au atom/ion from the top of one S atom in the pristine region to the sulphur vacancy site on the MoS₂ surface (Case 2). Reproduced with permission. [19] Copyright 2021, Wiley-VCH.

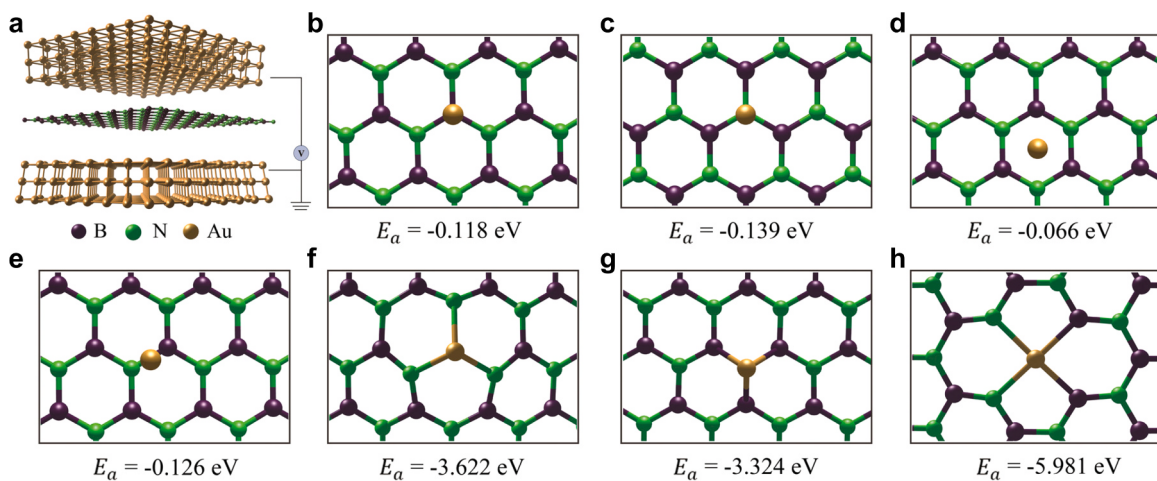


Fig. 16. a Schematic of a memristor based on one monolayer h-BN sandwiched between Au electrodes. b–e Adsorption of Au atoms on different sites of pristine monolayer h-BN, including: on the top of b boron atom, c nitrogen atom, d honeycomb, and e bridge site. f–h Adsorbed states of Au atoms on h-BN with f V_B, g V_N, and h V_{BN}. The Au ion is in the h-BN layer plane in d–h. In b and c the information related to the out plane location of the ion was not provided. Reproduced with permission. [207] Copyright 2022, American Institute of Physics.

This study demonstrated that a possible location for the CNF is the grain boundary of h-BN and provides valuable information about the dynamics of the entire set process. It is important to highlight that although the mentioned results are useful, the estimation of the applied voltage is overestimated. It is a normal situation for these types of studies because the emulation of the electric field by ReacFF is very complex.

4.4. Organic materials

The most commonly studied organic materials for RS applications are hybrid organic-inorganic perovskite (HOIPs), a family of compounds that have the generic chemical formula ABX₃, where A = CH₃NH₃⁺ or CH(NH₂)₂⁺, B = Pb²⁺ or Sn²⁺, and X = I⁻, Br⁻, or Cl⁻. Among all of them, one of the most studied for RS applications is methylammonium lead iodide (CH₃NH₃PbI₃, often referred to as MAPbI₃, see Fig. 18a) [10] which has a band gap of ~1.6 eV [220]. In this material, the most typical defects close to the conduction band are interstitial methylammonium (MA_i), and iodine vacancy [221]. That means, that the migration of those ions and vacancies under an external electrical field could modify the electrical resistance of the MAPbI₃ layer and its interaction with the metallic electrodes. In reference [222] the authors calculate (via DFT) the

binding energy per atom of MAPbI₃ with Cr and Ag electrodes, obtaining values of -0.096 eV and -0.094 eV, respectively. Although these values are underestimated because they were calculated using the PBE functional, this result suggests that the binding energy in both cases is very small due to the interface mismatch of the metal and the RS material (see Fig. 18b-c). The authors also calculated the formation energy of an iodine vacancy near and far from the metal/MAPbI₃ interface (V^a and V^b in Fig. 18b-c, respectively) for both Cr and Ag electrodes, and obtained V^a=0.812 eV and V^b=1.355 eV for Cr electrodes and V^a=1.492 eV and V^b=1.384 eV for Ag electrodes. These results indicate that when using Cr electrodes, the formation of vacancies should be confined to the Cr/MAPbI₃ interface because the formation of vacancies far from the interface is less probable. On the contrary, in Ag/MAPbI₃ structures the formation of iodine vacancies should also occur in the bulk of the MAPbI₃ RS medium. In other words, these results indicate that the RS in the Cr/MAPbI₃ structure is an interfacial effect while it is a bulk process in the Ag/MAPbI₃ configuration [221]. The authors also used DFT to calculate the Schottky barrier of these two structures (without defects) and obtained 0.76 eV for Cr and 0.64 eV for Ag. Once that one V_I is created, these barriers decrease to 0.384 eV and 0.242 eV for Ag.

Organic RS media like pentacene, tris-(8-hydroxyquinoline) aluminium (Alq₃), 2-amino-4,5-imidazoledicarbonitrile (AIDCN) have smaller molecules, although they are still complex from the simulation point of view because they have several types of atoms and a high number of atoms per unit cell. In these cases, the DFT simulations can be used to study the molecule as a unitary group, calculating the spatial distribution of the orbitals, the electrostatic potential surface, the conduction or valence band levels of the entire molecule (also referred to as the lowest unoccupied molecular orbital [LUMO], and highest occupied molecular orbital [HOMO] in a chemical context), among others. Due to the large number of atoms per molecule simulating bulk materials is unfeasible.

In the OFF state of the organic of small molecules RS devices, typically there is a large barrier between the electrodes created by the organic layer placed between them. Once a large enough external electric field is applied, the metallic atoms from the electrode that are near the interface with the organic material become polarized, inducing charge accumulation in the interface metal/organic layers. To make it possible, it is usually necessary to add donor-acceptor dopants to the small molecule to allow this charge transfer. One example of that is the study of the device based on five different D-π-A molecules (D and A mean donor and acceptor, respectively) reported by D. Harshini et al. [223]. Fig. 19b shows the schematic of one of the 5 D-π-A molecules

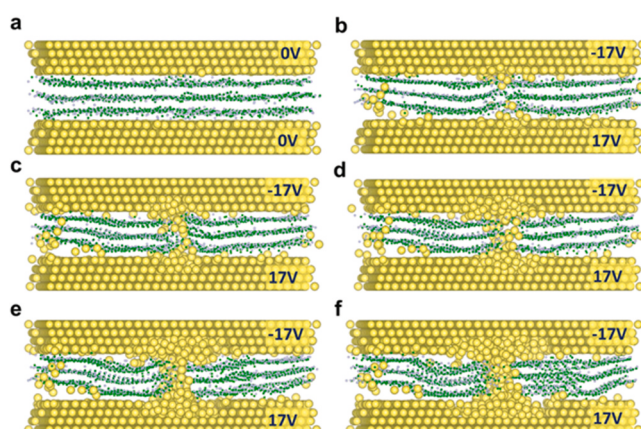


Fig. 17. Atomic snapshots of the formation of the CNF in hBN through grain boundary in a Ni/h-BN/Ni device. a at 0 V after 0.02 ns; at 34 V after b 0.005 ns, c 0.0075 ns, d 0.01 ns, e 0.015 ns, and f 0.02 ns. Ni, B, and N atoms are denoted by yellow, green, and silver balls, respectively. Reproduced with permission. [33] Copyright 2024, Nature.

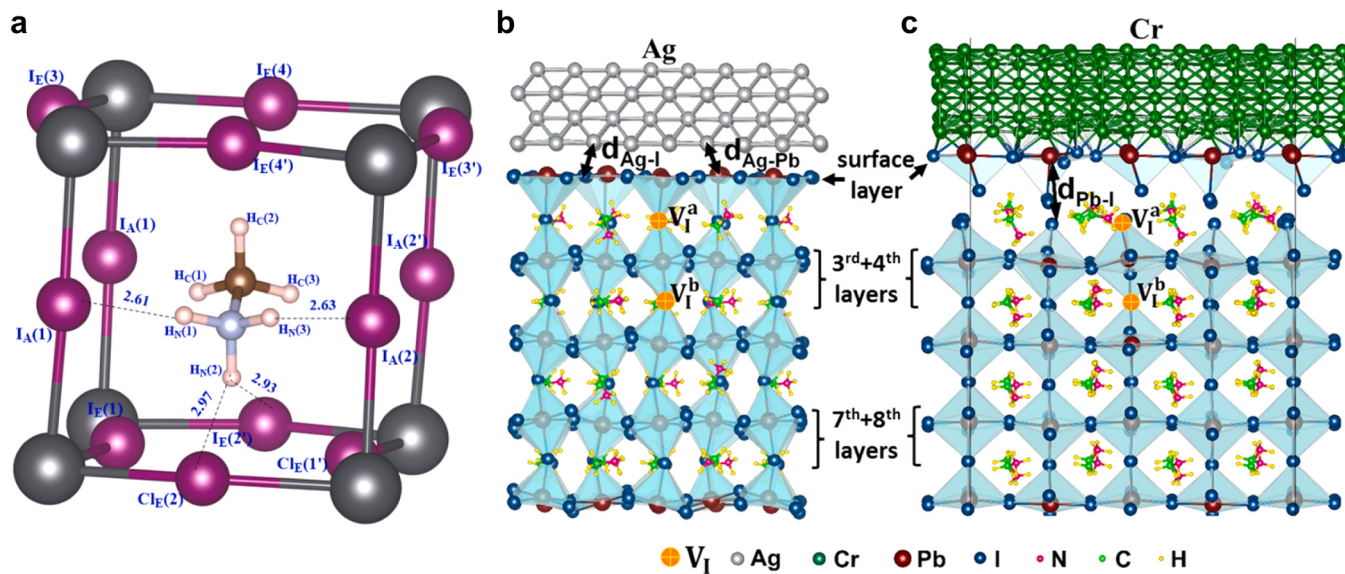


Fig. 18. **a** Schematic of the unit-cell of the organic cation and PbI₆ octahedra in undoped MAPbI₃. **b-c**, Atomic structure of **b** Ag/MAPbI₃ and **c** Cr/MAPbI₃ interfaces with the positions of iodine vacancy defects (V_I^{a,b}). The distance between the metallic electrode and the organic RS medium (d_{Ag,Pb,Cr,I}) are length of the bonds between the atoms in the electrode and the RS medium. Reproduced with permission **a** [220] copyright 2020, Elsevier, **b** and **c** [222] copyright 2023, IOP.

where the blue region is a Triarylgamine acting as the donor, the green region corresponds to a Benzophenone acting as the acceptor, and the purple region is the “backbone” that connects both doped regions. The calculation of the spatial distribution of the molecule orbitals (Fig. 19a) shows that when the external voltage increases and is close to the switching voltage, electrons gain enough energy to transfer from the HOMO to the LUMO+2 of the donor part (see right side of the molecule in Fig. 19a). This excitation of the donor region decreases the ionization potential allowing the formation of a channel throughout the Triarylgamine side, switching the device from HRS to LRS.

By analysing the electronic structure of the molecule via ESP mapping one can establish the correlation between charge dispersion and memory retention. In Fig. 19c the red region of the ESP map was found to serve as an accessible pathway for electron transport throughout the molecular backbone. The electron-withdrawing groups BP, –CHO, and –CN, located within the negative ESP region, were identified as potential traps within the molecular structure. In addition, it was observed that the trapped charges could be stabilized via intra- or intermolecular charge transfer in the excited state. These trapped charges persisted even after a reverse voltage sweep, contributing to the long-term stability of

the low resistive state. Although this state is not reversible and hence these types of materials cannot be used for RS devices, they can still be employed to produce write-once-read-many (WORM) memories.

4.5. Magnetic materials

RS devices based on magnetic materials exploit a magnetic tunnel junction (MTJ), i.e., a metal/insulator/metal cell in which the insulator is extremely thin (~2 nm) and the metallic electrodes are ferromagnetic [224]. The current tunnelling that crosses the insulator is spin-polarized, and the MTJ changes its electrical resistance by changing the relative magnetic orientation between the two ferromagnetic layers [225]. If their magnetic orientation points in opposite directions (anti-parallel state) the device is in HRS, and if both layers point in the same direction (parallel state) the device is in LRS [226,227].

Half-metallic ferromagnetic materials, such as Zn_{1-2x}Cr_xTi_xSe, Zn_{1-2x}Cr_xTi_xTe [228], CrO₂ [229], Fe₃GeTe₂ [230], and MgO [231,232] have nearly 100 % spin polarization. That means that the behaviour of one of the two spin channels is semiconducting or insulating and the other channel is metallic, so the conductivity is dominated by the metallic spin polarization direction [233–236]. This double spin channel can be studied via DFT simulations by calculating the density of states (DOS) of these materials. For instance, Fig. 20 shows the partial DOS of Zn_{0.9}Cr_{0.05}Ti_{0.05}Se and Zn_{0.9}Cr_{0.05}Ti_{0.05}Te [228]. From the total DOS (yellow area) it is clear that both materials show an asymmetric behaviour, i.e., a magnetic nature. The spin-up states in the band gap region exhibit a metallic nature while the missing spin-down states confirm the semiconductor behaviour. The spin-up states are created by the 3d-orbitals of Cr- and Ti atoms according to the partial DOS results. The shifted magnetic bands of Cr- and Ti-cations are formed respectively by the four and two remaining electrons. The first magnetic band is doubly degenerated and fully filled by electrons for both compounds, whereas the second is triply degenerated and contains two electrons for Zn_{0.9}Cr_{0.05}Ti_{0.05}Se. However, in Zn_{0.9}Cr_{0.05}Ti_{0.05}Te it is empty, as it is possible to see in the extension of the pink area in the second case.

The switching dynamics in ferromagnetic materials can be studied via DFT simulations by calculating the band structure. Reference [229] calculated the band structure of CrO₂ (see Fig. 21) and observed that the bands over the Fermi level of the spin-up orientation (red lines) demonstrate metallic behaviour. On the contrary, the spin-down

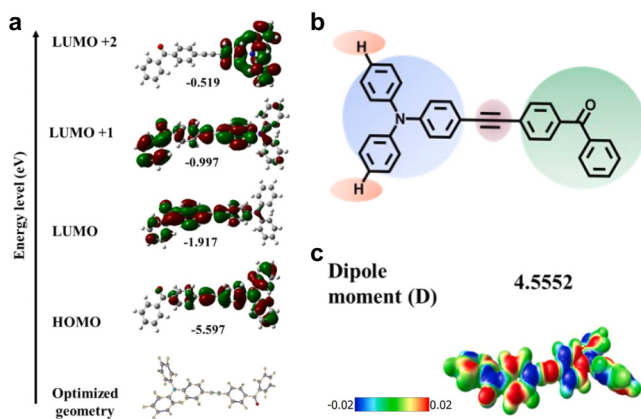


Fig. 19. **a** Calculated molecular orbitals and corresponding energy levels for **b** the D- π -A molecular structure compound. The calculated dipole moment of the molecule is shown in **c**. Reproduced with permission [223] copyright 2022, American Chemical Society.

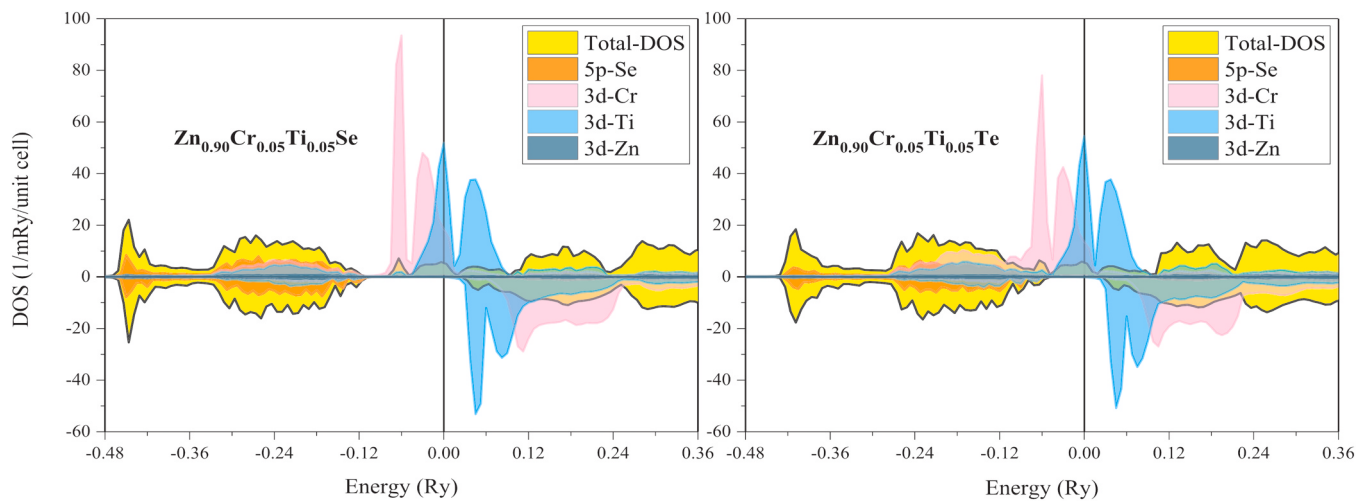


Fig. 20. The total- and partial-DOS of $\text{Zn}_{0.9}\text{Cr}_{0.05}\text{Ti}_{0.05}\text{Se}$ (left) and $\text{Zn}_{0.9}\text{Cr}_{0.05}\text{Ti}_{0.05}\text{Te}$ (right) systems versus energy (relative to the Fermi level). Reproduced with permission. [228] Copyright 2020, Elsevier.

orientation shows a band gap of 4.62 eV confirming the insulator behaviour. In the parallel configuration of both CrO_2 layers, the polarized electrons generated in the first ferromagnetic layer cross to the second layer pushed by the applied positive bias. There, the spin-up channel is also enabled, and hence electrons can flow across the entire device. In the anti-parallel configuration, the channel of the second ferromagnetic layer is open in the down-spin polarization. The positive bias moves the Fermi level in the upward direction in the first layer and in the downward direction in the second, enlarging the bandgap. This increase in the bandgap and the mismatch of the transmission channels (spin-up in the first layer and spin-down in the second) block the conduction throughout the device. Similar conclusions were extracted for CaV_2S_4 , CaMn_2S_4 [237], Fe_3GeTe_2 [230], MgO [231], or Ni_2MnGa [238], confirming these dynamics.

4.6. Ferroelectric materials

A ferroelectric material is a type of material that exhibits a spontaneous electric polarization that can be reversed by applying an external electric field. This means that the electric dipole moment of the material can be aligned in one of two directions, usually referred to as “up” and “down”, which generates two resistive states. This behaviour

spontaneously appears for the non-symmetric crystal configuration of several materials, such as HfO_2 [75,239–241], BaFeO_3 [242], $\text{InC}_{16}\text{H}_{11}\text{N}_2\text{O}_8$ [243], AlScN [244,245], BaTiO_3 [246,247] (among others). These phases of those materials show a piezoelectric effect, meaning that they can generate an electric field in response to mechanical stress. In this domain, DFT simulations have been used to study the transition between phases of the crystal and the role that dopants or vacancies play in those processes.

The crystal phase determines the polar or non-polar behaviour of the materials (Fig. 22a). According to reference [239], they demonstrated by DFT simulations that the cubic HfO_2 $Fm\bar{3}m$ (stable at 2870 K), the tetragonal $P4_2/nmc$, orthorhombic $Pcba$ and $Pnma$, and the monoclinic $P2_1/m$ and $P2_1/c$ (the most stable) show a non-polar behaviour. On the contrary, orthorhombic $Pca2_1$ and $Pmn2_1$, monoclinic Pm and Cc , and triclinic $P1$ show polar behaviour. According to several studies based on DFT calculations, the orthorhombic $Pca2_1$ is the most stable phase with about 60 meV/f.u. [239,241,248–250] — f.u. stands for formula unit, a notation often used to quantify the energy (or other parameters) per unit cell. As Fig. 22b shows, the phase transition can be promoted by variations in pressure and/or temperature. In memory applications, the ferroelectric phase must be stable at temperatures up to 85 °C, which can be challenging in some materials.

In HfO_2 the transition between polarization states is restricted by a high coercive field; therefore, a very large electric field is required to reverse the polarity [251–253]. Based on the results of ref. [239], M. Pešić et al. [240] shows the transition path from the ferroelectric to the antiferroelectric phase calculated by the Nudged Elastic Band (NEB) simulations [44]. It demonstrated that the tetragonal state is an intermedia phase between both polarization phases (see Fig. 22c). In addition, according to this result, the electric field needed to reverse the polarization state is about 1.2 MV/cm in agreement with the experimental data [254].

In order to improve the ferroelectric properties or to force this behaviour, frequently some dopants are added to the material. For instance, Si dope HfO_2 helps to stabilize the orthorhombic phase [75], and Zr dope improves the endurance of the memory device [255]. Contrary to the previous types of memories from the previous sections, in the case of ferroelectric devices, the studies related to the implantation of dopants are focused on the stability of the phases. To do that, the most common practice is calculating the difference in energy between the ferroelectric phase and a non-polar state of reference. As an example of that, C. Künneth et al. calculate the difference in energy of the orthorhombic and tetragonal phases with respect to the monoclinic phase of HfO_2 considering Si doping concentration from 0 to 6.25 f.u.%

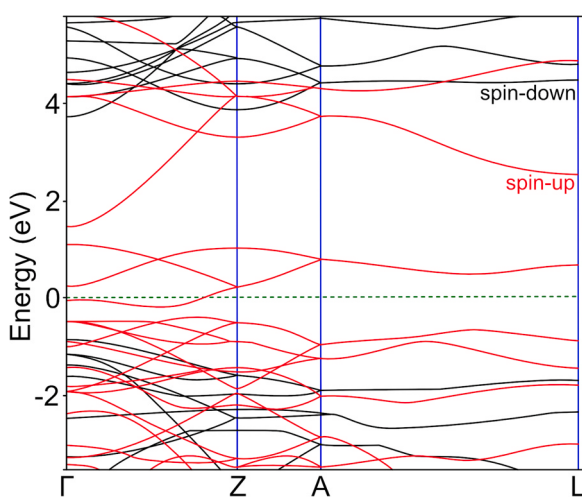


Fig. 21. Band structure of CrO_2 . The red and black lines correspond to the spin-up and spin-down polarization, respectively. Reproduced with permission. [229] Copyright 2021, IEEE.

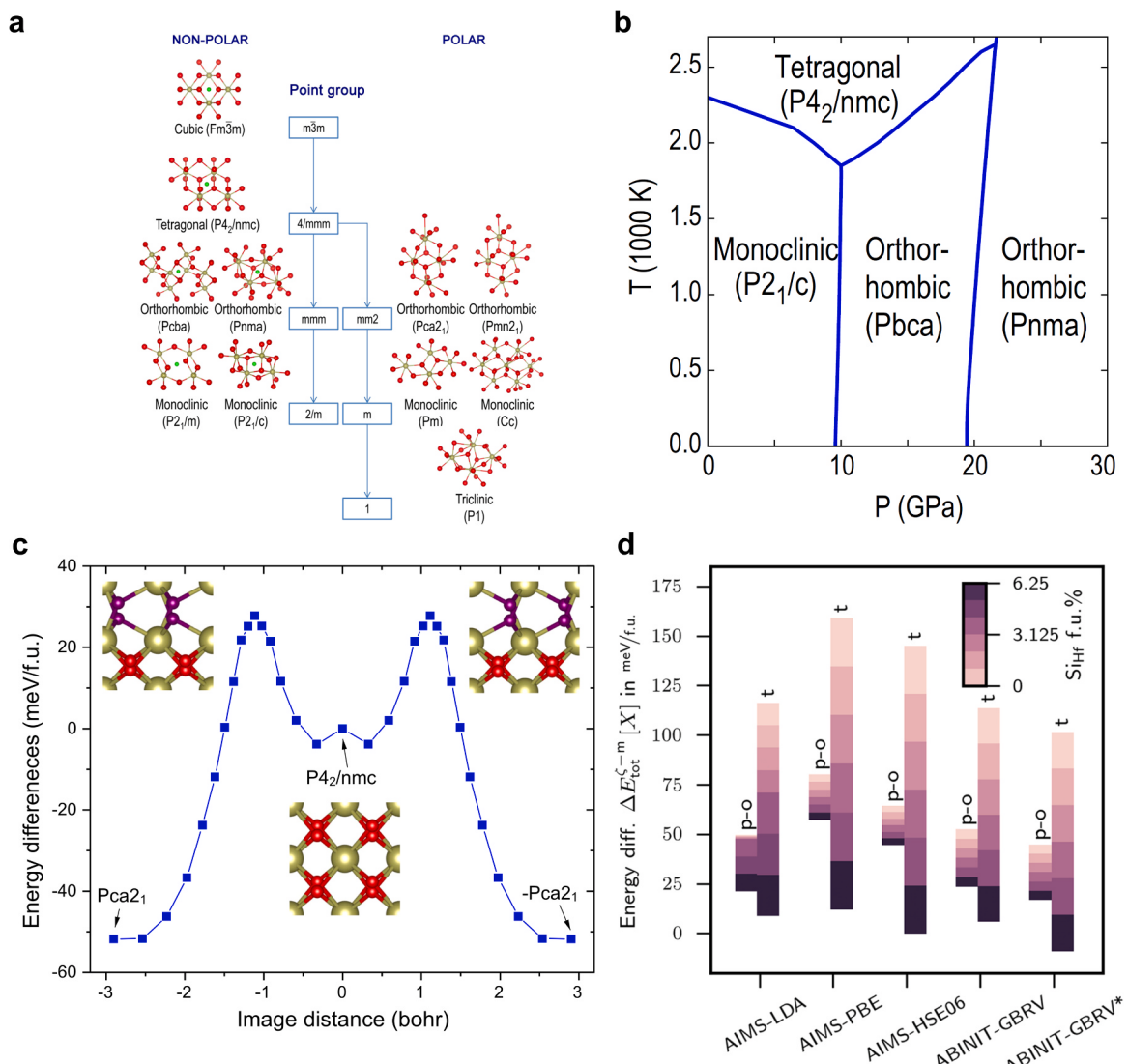


Fig. 22. **a** A flowchart of the evolution of the crystallographic structure of hafnia from lower to higher energy. **b** Computed equilibrium phase diagram of hafnia. **c** NEB calculation of the transition path from the ferroelectric phase via the tetragonal to the negative ferroelectric phase. **d** Energy differences with respect to the m-phase for five different DFT methods up to a doping concentration of silicon-doped HfO_2 . Reproduced with permission **a** and **b** [239] Copyright 2014, American Physical Society, **c** [240] Copyright 2017, Springer, and **d** [75] Copyright 2018, American Chemical Society.

[75]. As Fig. 22d shows, the energy difference was calculated using several methods and functionals, which is the correct practice as explained in section 2.3.

Analysing this result, the tetragonal phase is energetically lower than the orthorhombic phase which is consistent with the previous result showed about the stability of the phases. However, the energy of the tetragonal phase is not the lowest in energy for all simulation methods and doping concentrations. For this reason, Si doping cannot be discarded as a possible stability factor based on the obtained results.

5. Random telegraph signals

A random telegraph signal (RTS) shows stochastic transitions between two or more distinguishable current levels over time when an external stress is applied. Many RS devices exhibit RTS-like currents when specific biasing conditions are applied, especially those made of metal-oxides and 2D materials. While this mechanism strictly implies a change in the resistance (that is, RS) when a transition from one state to another takes place, it has not been referred in the literature as an RS behaviour because the current levels cannot be pre-programmed and

because none of them is constant over time (in contrast to non-volatile bipolar/unipolar RS or even volatile unipolar threshold-type RS). This impedes exploiting RTS for the fabrication of non-volatile memories, neuromorphic computation, or radiofrequency switches, which are the main applications of RS devices. In fact, RTS-like currents in RS devices for those applications are a reliability problem because they could trigger unwanted state transitions spontaneously and/or complicate state identification. It is especially critical in multilevel RS devices, such as those employed for hardware implementation of artificial neural networks [256–259]. Hence, understanding the origin of RTS-like currents in RS devices could help to enhance their reliability. Moreover, RTS-like current signals in RS devices have recently found applications in the field of advanced data encryption, because the stochastic transitions between the current levels can be exploited to generate random number generator circuits [215,260]. Hence, we consider that analysing this phenomenon in RS devices is important.

The first observations of RTS in electronic devices consisted of stochastic fluctuations in the gate current and drain-to-source current of transistors [261], and they were considered a problem affecting the reliability of the gate dielectric (mainly SiO_2 or HfO_2) [262]. Such

changes are generally related to stochastic trapping and de-trapping of electrons in one or more defects, typically at one of the interfaces between the RS medium and the electrodes although it can also be related to deep traps in the RS medium [263]. RTS-like current signals observed in transistors and based on this principle have been traditionally referred as random telegraph noise (RTN). The physical mechanisms that control the RTN are still under discussion. However, the most accepted theory is that the temporal activation of a charged vacancy assists the random transport of electrons between traps [264–268]. The random vibrations of the atoms due to the temperature change the distance between atoms influencing the trapping dynamics [269] or producing temporal bonding reorganization between the atoms [267,270]. For example, Fig. 23 shows the crystal configuration and electron density calculated by DFT of two charge states (neutral and positive) of one oxygen vacancy in SiO_2 [265]. According to this result, the separation between silicon atoms close to one oxygen vacancy is larger if the vacancy is positively charged. This result demonstrates that a variation in the distance between atoms can modify the charge state of the oxygen vacancy. These random variations of the exact position of atoms can also allow the creation of a new Si-Si bonding that changes the atomic structure of the crystal.

DFT simulations can also be used to calculate all possible defect configurations (position of atoms, charge of the defects) which allows to identify all possible electron trapping and de-trapping transitions. In reference [271], the authors calculated the total energy of several defect configurations (different possible positions and charge states) of one oxygen vacancy in SiO_2 . The minimum energy configurations correspond to the metastable states of the neutral and positive defect (N or N' , and P or P' in Fig. 24). When the barrier between the states is small the transition can take place spontaneously, and when it is relatively high an external electrical field is necessary to spark it.

Later studies also reported RTS-like currents in RS-based non-volatile memories made of metal-oxides (such as HfO_2 , TiO_2 , Ta_2O_5). When the RTS-like current is detected in the HRS the working principle shows many similarities to the RTN observed in transistors — and some authors referred to it by such name — and it is mainly based on electron trapping and de-trapping at oxygen vacancies [272,273].

RS devices have also exhibited RTS-like currents in the LRS, but in such cases, the current fluctuations are much higher (hundreds or thousands of microamperes), and they cannot be explained by simply electron trapping and de-trapping. Hence, strictly speaking, those signals cannot be called RTN. The physical mechanism producing RTS-like current in RS-based non-volatile memory programmed in LRS is still under debate, but it has been proposed that it might be related to more profound atomic rearrangements due to the Joule effect at those higher currents. In particular, oxidation/reduction of vacancies or drift of metallic ions from/to the adjacent electrodes are the most accepted theories, similar to what has been discussed in Section 4.2. In some cases, it is also possible to detect gigantic RTS-like current signals in which current across the RS device randomly fluctuates between two levels separated by several orders of magnitude at constant voltage

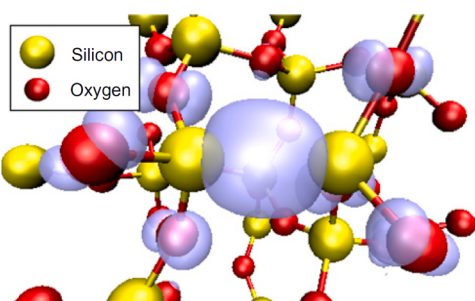


Fig. 23. Two charge states of the one oxygen vacancy calculated by DFT, neutral (left) and positive (right). The electron density is shown as blue regions. Reproduced with permission. [265] Copyright 2012, Elsevier.

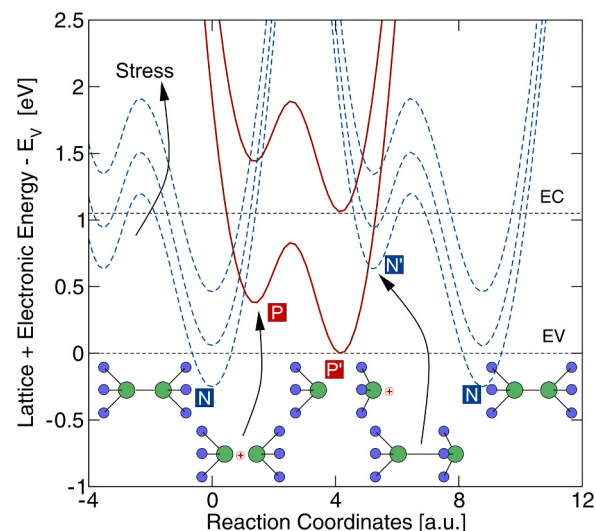
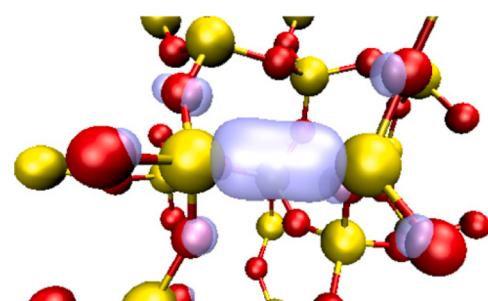
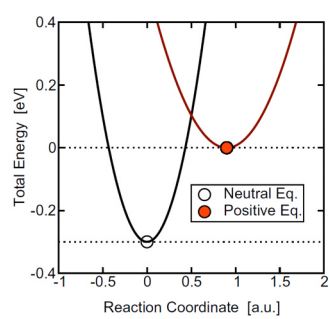


Fig. 24. Total energy surfaces of the metastable states of the neutral defect (dashed lines) and positive (solid lines) states. In the crystal schematic the blue circles represent the oxygen atoms, and the green circles are the silicon atoms. Reproduced with permission. [271] Copyright 2010, Springer.

[260], having the HRS above the quantum conductance and the LRS below it. This effect is observed when the atomic rearrangements in each transition form/disrupt a CNF effectively connecting/disconnecting the two electrodes. Such type of atomic rearrangements normally take place only at the weakest part of the filament, leaving the rest nearly intact in both states.

Note that RTS-like currents can also take place in other oxygen-free RS devices programmed in HRS, such as those using synthetic multilayer h-BN as RS medium [215,260]. In this material, native defects amorphous in nature are embedded inside the crystalline layered structure of the h-BN stack, and they have exhibited RTS-like currents not only at the device level but also when they are tested individually via conductive atomic force microscopy [215]. In these samples, DFT simulations helped to understand that the out-of-plane currents are confined at the amorphous native defects and that their lateral expansion is improbable because the energy for new defects formation (boron vacancies) in the crystalline structure is very high (10 eV, while at the defects it is much lower). Based on the conclusion of the study in reference [215], partially based on the results of DFT simulations, the authors engineered the structure of the h-BN device by changing its size (to $50 \mu\text{m} \times 50 \mu\text{m}$, to have more and weaker defects) and deposition method of the top electrode (to inkjet printing, to avoid uncontrolled damage in the h-BN). The resulting Ag/h-BN/Ag devices exhibited highly stable RTS-like currents in HRS, with a low power consumption of $\sim 5.25 \text{ nW}$ [274].

At the device level, RTS is studied using Monte Carlo and compact models. Those models are more adequate for the characterization of RTS



due to their intrinsic stochastic nature. DFT simulations are frequently used to calculate the chemical and/or physical parameters of the materials and defects that those models need, such as the electron affinity of the defects [275], the energy barrier between states [271,276], and the thermal ionization and relaxation of the defects [276–279].

6. Future perspectives

Although in this work the different aspects of each RS materials and mechanisms have been explained, the complete switching and transport mechanisms are not completely understood or they are controversial in some cases. As we mentioned in previous sections, DFT and MD do not allow us to simulate a complete system. Instead, we must split the system into several smaller problems such as vacancy generation, ions diffusion across the electrode/switching layer interface, crystal structure distortion, etcetera. For this reason, a complete picture of the RS process is missing to a greater or lesser extent depending on the materials and the type of RS mechanisms. In order to achieve a general model for each type of material, all possible mechanisms and processes must be considered and simulated.

In parallel to that, it is well known that one of the bottlenecks of the application of the RS technology to final products is its high cycle-to-cycle and/or device-to-device variability. This problem is inherent to the RS process due to the fast and stochastic nature of all mechanisms that play a role. One of the possible solutions to this problem could come from the use of new materials. In this field, the DFT and MD simulations play in key role since they allow us to prospect and discriminate new material and alloy candidates at low cost and in a reasonable time. This valuable information can be used by experimental teams to fabricate new devices with the correct configuration.

The advances on these fronts are also linked to the ongoing developments in both DFT and MD methodologies. On the MD front, the emerging new techniques to generate more accurate and transferable interatomic potentials, coupled with parallel computing and sophisticated computational algorithms, are steadily enhancing the capability to simulate intricate material behaviours over extended time and length scales. Regardless of the complexity of the interatomic potential in the form described in Section 2.2, it is still mainly empirical, since they are parametrized assuming the atoms will be arranged in certain angles with certain bond distances and using some physical properties such as elastic constants and lattice parameters. Although these potentials are exceptionally faster than DFT simulations, they are however less accurate and transferable. Lately, machine learning-based approaches offer a significant improvement in the accuracy of MD simulations. Machine learning-based models such as Gaussian Approximation Potentials (GAP) [280], DeePMD [281,282], and Moment Tensor Potentials (MTP) [283] can be trained to describe the interactions between atoms and potential energy surface (PES) from the relevant data obtained from a more accurate but more expensive theory (mostly DFT) without making any assumptions regarding the functional form of the interatomic potential. This allows us to perform MD simulations with an accuracy similar to the reference method but on a much larger scale. Being able to study on such large size and time scales will improve our understanding of the dynamics of atoms under certain conditions. Despite the great improvement in accuracy, machine learning-assisted MD simulations are still classical and cannot provide an explicit picture of electrons and electronic properties such as band gap or density of states [284,285].

Alternatively, ab initio MD (AIMD) simulations represent a methodological bridge between classical MD and DFT simulations. In AIMD, the forces between atoms are calculated using quantum mechanics, as in DFT simulations, and then velocities and positions of each nucleus for the next timestep are calculated using classical equations of motion, similar to the classical MD simulations. This is an iterative process. After the atomic positions of each atom are calculated, a new electronic structure calculation is performed based on the new geometry which enables the simulation of the dynamical evolution of the molecular

system [286]. To describe the interaction between atoms, AIMD uses pseudopotentials or localized orbital basis sets, hence, it does not rely on the predefined empirical potentials. This also allows AIMD to provide electronic information and properties of the system under investigation. Despite the advantages over classical MD, AIMD suffers from time and size limitations like the DFT [287]. Even though it can model larger systems compared to the DFT with great accuracy, the size and time scales it can be studied are still limited when compared to the classical MD.

In addition to the mentioned improvements in algorithms, the continuous improvement of supercomputers helps reduce the gap between theoretical predictions and experimental observations in RS research.

7. Conclusions

Resistive switching (RS) devices have exhibited outstanding potential for multiple applications in micro/nano-electronics, not only the already commercial non-volatile memories but also others still in development like artificial neural networks, advanced data encryption and high-frequency (5 G/6 G) telecommunication. However, all these RS technologies suffer reliability issues due to the limited understanding and control over the atomic rearrangements taking place during voltage-induced state transitions. In this article, we have shown how DFT and MD simulations can help researchers to understand the switching mechanism of RS devices. In particular, MD simulations have been used to calculate the stability of different atomic configurations of phase-change materials (crystalline and amorphous), as well as the position of the atoms during the phase transition and the energy and time consumed. DFT simulations have been used to calculate the formation energy of vacancies in metal-oxides and 2D materials, and to determine whether they are likely to aggregate forming clusters of defects. Similar calculations have been performed to study the penetration of metallic ions from the electrode into the metal-oxide and 2D material, both in terms of energy required to overcome the interface and locations towards which the metal ion is more likely to move. In magnetic materials, DFT has been used to calculate the magnetic orientation and the density of states in HRS and LRS. In ferroelectric materials, DFT simulations are especially useful to characterize the different phases and the transition energy between them. Finally, in organic RS materials, the DFT calculations have helped to understand that RS is mainly related either to interface or charge density modulation. Complementing experimental studies in the field of RS with DFT and MD simulations of the RS mechanism would result in a more reliable understanding of RS devices, which should enable/accelerate their integration into commercial technologies.

CRediT authorship contribution statement

Onurcan Kaya: Writing – review & editing. **Udo Schwingschlägl:** Validation. **Stephan Roche:** Writing – review & editing. **Marco A. Villena:** Writing – original draft, Visualization, Methodology, Investigation, Data curation. **Mario Lanza:** Writing – review & editing.

Declaration of Competing Interest

The authors declare that they have no known competing financial interests or personal relationships that could have appeared to influence the work reported in this paper.

Data Availability

No data was used for the research described in the article.

Acknowledgments

This work has been supported by the baseline funding scheme of the King Abdullah University of Science and Technology. ICN2 acknowledges the Grant PCI2021-122092-2A funded by MCIN/AEI/10.13039/501100011033 and by the ‘European Union NextGenerationEU/PRTR’. This work has been performed ‘Amb el suport del Departament de Recerca i Universitats de la Generalitat de Catalunya’ and with funding from PN: ‘Proyecto PID2022-138283NB-I00 (MCIN/ AEI /10.13039/501100011033) and by FEDER. The author O.K. is supported by the REDI Program, a project that has received funding from the European Union’s Horizon 2020 research and innovation program under the Marie Skłodowska-Curie grant agreement no. 101034328. This paper reflects only the author’s view and the Research Executive Agency is not responsible for any use that may be made of the information it contains. Prof. Mario Lanza acknowledges the platform Web Of Talents (<https://weboftalents.com>) for support on the recruitment of talented students and postdocs.

Appendix A. Supporting information

Supplementary data associated with this article can be found in the online version at [doi:10.1016/j.mser.2024.100825](https://doi.org/10.1016/j.mser.2024.100825).

References

- [1] M. Lanza, G. Molas, I. Naveh, *Nat. Electron.* 6 (2023) 260–263.
- [2] K. Zhu, S. Pazos, F. Aguirre, Y. Shen, Y. Yuan, W. Zheng, O. Alharbi, M.A. Villena, B. Fang, X. Li, A. Milozzi, M. Farronato, M. Muñoz-Rojo, T. Wang, R. Li, H. Fariborzi, J.B. Roldan, G. Benettet, X. Zhang, H.N. Alshareef, T. Grasser, H. Wu, D. Ielmini, M. Lanza, *Nature* 618 (2023) 57–62.
- [3] D. Ielmini, *Semicond. Sci. Technol.* 31 (2016) 063002.
- [4] M.M. Rehman, H.M.M.U. Rehman, J.Z. Gul, W.Y. Kim, K.S. Karimov, N. Ahmed, *Sci. Technol. Adv. Mater.* 21 (2020) 147–186.
- [5] W. Huh, D. Lee, C.-H. Lee, *Adv. Mater.* 32 (2020) 2002092.
- [6] S. Pazos, X. Xu, T. Guo, K. Zhu, H.N. Alshareef, M. Lanza, *Nat. Rev. Mater.* (2024) 1–16.
- [7] G.S.H. Thien, M. Ab Rahman, B.K. Yap, N.M.L. Tan, Z. He, P.-L. Low, N. K. Devaraj, A.F. Ahmad Osman, Y.-K. Sin, K.-Y. Chan, *ACS Omega* 7 (2022) 39472–39481.
- [8] D. Panda, T.-Y. Tseng, *Ferroelectrics* 471 (2014) 23–64.
- [9] K.Y. Cheong, I.A. Tayeb, F. Zhao, J.M. Abdullah, *Nanotechnol. Rev.* 10 (2021) 680–709.
- [10] E.J. Yoo, M. Lyu, J.-H. Yun, C.J. Kang, Y.J. Choi, L. Wang, *Adv. Mater.* 27 (2015) 6170–6175.
- [11] D. Ielmini, C. Cagli, F. Nardi, Y. Zhang, *J. Phys. D: Appl. Phys.* 46 (2013) 074006.
- [12] G. Milano, S. Porro, I. Valov, C. Ricciardi, *Adv. Electron. Mater.* 5 (2019) 1800909.
- [13] P. Liu, A.T. Liu, D. Koizawa, J. Dong, J.F. Yang, V.B. Koman, M. Saccone, S. Wang, Y. Son, M.H. Wong, M.S. Strano, *Nat. Mater.* 17 (2018) 1005–1012.
- [14] F. Hui, C. Zhang, H. Yu, T. Han, J. Weber, Y. Shen, Y. Xiao, X. Li, Z. Zhang, P. Liu, *Adv. Funct. Mater.* n/a (2023) 2302073.
- [15] J. Yang, L.Z. Tan, A.M. Rappe, *Phys. Rev. B* 97 (2018) 085130.
- [16] R. Waser, R. Dittmann, G. Staikov, K. Szot, *Adv. Mater.* 21 (2009) 2632–2663.
- [17] M.A. Villena, J.B. Roldán, F. Jiménez-Molinos, E. Miranda, J. Suñé, M. Lanza, *J. Comput. Electron.* 16 (2017) 1095–1120.
- [18] M. Lanza, H.-S.P. Wong, E. Pop, D. Ielmini, D. Strukov, B.C. Regan, L. Larcher, M. A. Villena, J.J. Yang, L. Goux, A. Belmonte, Y. Yang, F.M. Puglisi, J. Kang, B. Magyari-Köpe, E. Yalon, A. Kenyon, M. Buckwell, A. Mehonic, A. Shluger, H. Li, T.-H. Hou, B. Hudec, D. Akinwande, R. Ge, S. Ambrogio, J.B. Roldan, E. Miranda, J. Suñé, K.L. Pey, Y. Wu, N. Raghavan, E. Wu, W.D. Lu, G. Navarro, W. Zhang, H. Wu, R. Li, A. Holleitner, U. Wurstbauer, M.C. Lemme, M. Liu, S. Long, Q. Liu, H. Lv, A. Padovani, P. Pavan, I. Valov, X. Jing, T. Han, K. Zhu, S. Chen, F. Hui, Y. Shi, *Adv. Electron. Mater.* 5 (2019) 1800143.
- [19] R. Ge, X. Wu, L. Liang, S.M. Hus, Y. Gu, E. Okogbue, H. Chou, J. Shi, Y. Zhang, S. K. Banerjee, Y. Jung, J.C. Lee, D. Akinwande, *Adv. Mater.* 33 (2021) 2007792.
- [20] K.D.M. Rao, A.A. Sagade, R. John, T. Pradeep, G.U. Kulkarni, *Adv. Electron. Mater.* 2 (2016) 1500286.
- [21] M. Lanza, A. Sebastian, W.D. Lu, M. Le Gallo, M.-F. Chang, D. Akinwande, F. M. Puglisi, H.N. Alshareef, M. Liu, J.B. Roldan, *Science* 376 (2022) eabj9979.
- [22] F. Aguirre, A. Sebastian, M. Le Gallo, W. Song, T. Wang, J.J. Yang, W. Lu, M.-F. Chang, D. Ielmini, Y. Yang, A. Mehonic, A. Kenyon, M.A. Villena, J.B. Roldán, Y. Wu, H.-H. Hsu, N. Raghavan, J. Suñé, E. Miranda, A. Eltawil, G. Setti, K. Smagulova, K.N. Salama, O. Krestinskaya, X. Yan, K.-W. Ang, S. Jain, S. Li, O. Alharbi, S. Pazos, M. Lanza, *Nat. Commun.* 15 (2024) 1974.
- [23] Emerging non-volatile memory™: market analysis report, (<http://www.i-micronews.com/products/emerging-non-volatile-memory-2021>) (visited February 12, 2024).
- [24] C. Pan, Y. Ji, N. Xiao, F. Hui, K. Tang, Y. Guo, X. Xie, F.M. Puglisi, L. Larcher, E. Miranda, L. Jiang, Y. Shi, I. Valov, P.C. McIntyre, R. Waser, M. Lanza, *Adv. Funct. Mater.* 27 (2017) 1604811.
- [25] Y. Yang, Y. Takahashi, A. Tsurumaki-Fukuchi, M. Arita, M. Moors, M. Buckwell, A. Mehonic, A.J. Kenyon, *J. Electroceram.* 39 (2017) 73–93.
- [26] X. Guo, C. Schindler, S. Menzel, R. Waser, *Appl. Phys. Lett.* 91 (2007) 133513.
- [27] Y.C. Yang, F. Pan, Q. Liu, M. Liu, F. Zeng, *Nano Lett.* 9 (2009) 1636–1643.
- [28] Y. Li, S. Long, Q. Liu, H. Lv, M. Liu, *Small* 13 (2017) 1604306.
- [29] H. Yildirim, R. Pachter, *ACS Appl. Electron. Mater.* 1 (2019) 467–477.
- [30] S. Prada, M. Rosa, L. Giordano, C. Di Valentini, G. Pacchioni, *Phys. Rev. B* 83 (2011) 245314.
- [31] N. Onofrio, D. Guzman, A. Strachan, *Nat. Mater.* 14 (2015) 440–446.
- [32] S.M. Hus, R. Ge, P.-A. Chen, L. Liang, G.E. Donnelly, W. Ko, F. Huang, M.-H. Chiang, A.-P. Li, D. Akinwande, *Nat. Nanotechnol.* 16 (2021) 58–62.
- [33] S. Mitra, S. Mahapatra, *Npj 2D Mater. Appl.* 8 (2024) 1–14.
- [34] T.D. Dongale, S.S. Sutar, Y.D. Dange, A.C. Khot, S.S. Kundale, S.R. Patil, S.V. Patil, A.A. Patil, S.S. Khot, P.J. Patil, J. Bae, R.K. Kamat, T.G. Kim, *Appl. Mater. Today* 29 (2022) 101650.
- [35] S.M. Patil, S.S. Kundale, S.S. Sutar, P.J. Patil, A.M. Teli, S.A. Beknalkar, R. K. Kamat, J. Bae, J.C. Shin, T.D. Dongale, *Sci. Rep.* 13 (2023) 4905.
- [36] S. Ambrogio, B. Magyari-Köpe, N. Onofrio, M. Mahbubul Islam, D. Duncan, Y. Nishi, A. Strachan, *J. Electroceram.* 39 (2017) 39–60.
- [37] R.M. Martin, *Electronic Structure: Basic Theory and Practical Methods*, Cambridge University Press, Cambridge, 2004.
- [38] M.E. Tuckerman, *Statistical Mechanics: Theory and Molecular Simulation*, Oxford University Press, 2023.
- [39] P. Hohenberg, W. Kohn, *Phys. Rev.* 136 (1964) B864–B871.
- [40] A.D. Becke, *Phys. Rev. A* 38 (1988) 3098–3100.
- [41] J.P. Perdew, Y. Wang, *Phys. Rev. B* 45 (1992) 13244–13249.
- [42] G. Kresse, J. Hafner, *Phys. Rev. B* 49 (1994) 14251–14269.
- [43] M.J. Frisch, G.W. Trucks, H.B. Schlegel, G.E. Scuseria, M.A. Robb, J.R. Cheeseman, G. Scalmani, V. Barone, G.A. Petersson, H. Nakatsuji, X. Li, M. Caricato, A.V. Marenich, J. Bloino, B.G. Janesko, R. Gomperts, B. Mennucci, H.P. Hratchian, J.V. Ortiz, A.F. Izmaylov, J.L. Sonnenberg, D. Williams-Young, F. Ding, F. Lipparini, F. Egidi, J. Goings, B. Peng, A. Petrone, T. Henderson, D. Ranasinghe, V.G. Zakrzewski, J. Gao, N. Rega, G. Zheng, W. Liang, M. Hada, M. Ehara, K. Toyota, R. Fukuda, J. Hasegawa, M. Ishida, T. Nakajima, Y. Honda, O. Kitao, H. Nakai, T. Vreven, K. Throssell, J.A. Montgomery Jr., J.E. Peralta, F. Ogliaro, M.J. Bearpark, J.J. Heyd, E.N. Brothers, K.N. Kudin, V.N. Staroverov, T. A. Keith, R. Kobayashi, J. Normand, K. Raghavachari, A.P. Rendell, J.C. Burant, S. S. Iyengar, J. Tomasi, M. Cossi, J.M. Millam, M. Klene, C. Adamo, R. Cammi, J.W. Ochterski, R.L. Martin, K. Morokuma, O. Farkas, J.B. Foresman, D.J. Fox, Gaussian Inc. (2016) <<https://gaussian.com/gaussian16/>>.
- [44] P. Giannozzi, S. Baroni, N. Bonini, M. Calandri, R. Car, C. Cavazzoni, D. Ceresoli, G.L. Chiarotti, M. Cococcioni, I. Dabo, A.D. Corso, S. de Gironcoli, S. Fabris, G. Fratesi, R. Gebauer, U. Gerstmann, C. Gouguissis, A. Kokalj, M. Lazzeri, L. Martin-Samos, N. Marzari, F. Mauri, R. Mazzarello, S. Paolini, A. Pasquarello, L. Paulatto, C. Sbraccia, S. Scandolo, G. Scaluzero, A. Seitsonen, A. Smogunov, P. Umari, R.M. Wentzcovitch, *J. Phys.: Condens. Matter* 21 (2009) 395502.
- [45] P. Giannozzi, O. Andreussi, T. Brummel, O. Bunau, M.B. Nardelli, M. Calandri, R. Car, C. Cavazzoni, D. Ceresoli, M. Cococcioni, N. Colonna, I. Carnimeo, A. D. Corso, S. de Gironcoli, P. Delugas, R.A. DiStasio, A. Ferretti, A. Floris, G. Fratesi, G. Fugallo, R. Gebauer, U. Gerstmann, F. Giustino, T. Gorni, J. Jia, M. Kawamura, H.-Y. Ko, A. Kokalj, E. Küçükbenli, M. Lazzeri, M. Marsili, N. Marzari, F. Mauri, N.L. Nguyen, H.-V. Nguyen, A. Otero-de-la-Roza, L. Paulatto, S. Poncé, D. Rocca, R. Sabatini, B. Santra, M. Schlipf, A.P. Seitsonen, A. Smogunov, I. Timrov, T. Thonhauser, P. Umari, N. Vast, X. Wu, S. Baroni, *J. Phys.: Condens. Matter* 29 (2017) 465901.
- [46] S. Smidstrup, T. Markussen, P. Vancrevelweld, J. Wellendorff, J. Schneider, T. Gunst, B. Verstichel, D. Stradi, P.A. Khomyakov, U.G. Vej-Hansen, M.-E. Lee, S. T. Chill, F. Rasmussen, G. Penazzi, F. Corsetti, A. Ojanperä, K. Jensen, M.L. N. Palsgaard, U. Martinez, A. Blom, M. Brandbyge, K. Stokbro, *J. Phys.: Condens. Matter* 32 (2019) 015901.
- [47] T.D. Kühne, M. Iannuzzi, M. Del Ben, V.V. Rybkin, P. Seewald, F. Stein, T. Laino, R.Z. Khalilli, O. Schütt, F. Schiffmann, D. Golze, J. Wilhelm, S. Chulkov, M. H. Bani-Hashemian, V. Weber, U. Borštník, M. Taillefumier, A.S. Jakobovits, A. Lazzaro, H. Pabst, T. Müller, R. Schade, M. Guidon, S. Andermatt, N. Holmberg, G.K. Schenter, A. Hehn, A. Bussy, F. Belleflamme, G. Tabacchi, A. Glööb, M. Lass, I. Bethune, C.J. Mundy, C. Plessl, M. Watkins, J. Vandevondele, M. Krack, J. Hutter, *J. Chem. Phys.* 152 (2020) 194103.
- [48] E. Artacho, E. Anglada, O. Diéguez, J.D. Gale, A. García, J. Junquera, R. M. Martin, P. Ordejón, J.M. Prunedo, D. Sánchez-Portal, J.M. Soler, *J. Phys.: Condens. Matter* 20 (2008) 064208.
- [49] A. García, N. Papir, A. Akhtar, E. Artacho, V. Blum, E. Bosoni, P. Brandimarte, M. Brandbyge, J.I. Cerdá, F. Corsetti, R. Cuadrado, V. Dikan, J. Ferrer, J. Gale, P. García-Fernández, V.M. García-Suárez, S. García, G. Huhs, S. Illera, R. Kortyári, P. Koval, I. Lebedeva, L. Lin, P. López-Tarifa, S.G. Mayo, S. Mohr, P. Ordejón, A. Postnikov, Y. Pouillon, M. Prunedo, R. Robles, D. Sánchez-Portal, J.M. Soler, R. Ullah, V.W. Yu, J. Junquera, *J. Chem. Phys.* 152 (2020) 204108.
- [50] A.P. Thompson, H.M. Aktulga, R. Berger, D.S. Bolintineanu, W.M. Brown, P. S. Crozier, P.J. in 't Veld, A. Kohlmeyer, S.G. Moore, T.D. Nguyen, R. Shan, M. J. Stevens, J. Tranchida, C. Trott, S.J. Plimpton, *Comput. Phys. Commun.* 271 (2022) 108171.
- [51] W. Kohn, L.J. Sham, *Phys. Rev.* 140 (1965) A1133–A1138.
- [52] J.P. Perdew, Y. Wang, *Phys. Rev. B* 98 (2018) 079904.
- [53] D.M. Ceperley, B.J. Alder, *Phys. Rev. Lett.* 45 (1980) 566–569.

- [54] D. Rappoport, N.R. Crawford, F. Furche, K. Burke, C. Wiley, *Comput. Inorg. Bioinorg. Chem.* 594 (2008) 1–25.
- [55] J.E. Jones, Proc. R. Soc. Lond. Ser. A, Contain. Pap. A Math. Phys. Character 106 (1924) 441–462.
- [56] J.E. Lennard-Jones, Proc. Phys. Soc. 43 (1931) 461.
- [57] J. Wildman, P. Repičák, M.J. Paterson, I. Galbraith, *J. Chem. Theory Comput.* 12 (2016) 3813–3824.
- [58] R. Jinnouchi, J. Lahnsteiner, F. Karsai, G. Kresse, M. Bokdam, *Phys. Rev. Lett.* 122 (2019) 225701.
- [59] R. Jinnouchi, F. Karsai, G. Kresse, *Phys. Rev. B* 100 (2019) 014105.
- [60] R. Jinnouchi, F. Karsai, C. Verdi, R. Asahi, G. Kresse, *J. Chem. Phys.* 152 (2020) 234102.
- [61] A.C.T. van Duin, S. Dasgupta, F. Lorant, W.A. Goddard, *J. Phys. Chem. A* 105 (2001) 9396–9409.
- [62] M.F. Russo, A.C.T. van Duin, *Nucl. Instrum. Methods Phys. Res. Sect. B: Beam Interact. Mater. At.* 269 (2011) 1549–1554.
- [63] D.R. Hamann, M. Schlüter, C. Chiang, *Phys. Rev. Lett.* 43 (1979) 1494–1497.
- [64] D. Vanderbilt, *Phys. Rev. B* 41 (1990) 7892–7895.
- [65] P.E. Blochl, *Phys. Rev. B* 50 (1994) 17953–17979.
- [66] G. Kresse, D. Joubert, *Phys. Rev. B* 59 (1999) 1758–1775.
- [67] VASP – Available PAW potential website, (https://www.vasp.at/wiki/index.php/Available_PAW_potentials) (visited February 5, 2024).
- [68] K. Schwarz, P. Blaha, *Comput. Mater. Sci.* 28 (2003) 259–273.
- [69] R. Dovesi, A. Erba, R. Orlando, C.M. Zicovich-Wilson, B. Civalleri, L. Maschio, M. Réat, S. Casassa, J. Baima, S. Salustro, B. Kirtman, *WIREs Comput. Mol. Sci.* 8 (2018) e1360.
- [70] J.P. Perdew, K. Burke, Y. Wang, *Phys. Rev. B* 54 (1996) 16533–16539.
- [71] R. Pererati, D.G. Truhlar, *J. Chem. Theory Comput.* 8 (2012) 2310–2319.
- [72] A.V. Krukau, O.A. Vydrov, A.F. Izmaylov, G.E. Scuseria, *J. Chem. Phys.* 125 (2006) 224106.
- [73] C. Lee, W. Yang, R.G. Parr, *Phys. Rev. B* 37 (1988) 785–789.
- [74] H. Yıldırım, R. Pachter, *ACS Appl. Mater. Interfaces* 10 (2018) 9802–9816.
- [75] C. Künneth, R. Materlik, M. Falkowski, A. Kersch, *ACS Appl. Nano Mater.* 1 (2018) 254–264.
- [76] J.-H. Yuan, Q. Chen, L.R.C. Fonseca, M. Xu, K.-H. Xue, X.-S. Miao, *J. Phys. Commun.* 2 (2018) 105005.
- [77] N. Ooi, A. Raikar, L. Lindsley, J.B. Adams, *J. Phys.: Condens. Matter* 18 (2005) 97.
- [78] E.S. Kadantsev, P. Hawrylak, *Solid State Commun.* 152 (2012) 909–913.
- [79] R. Coehoorn, C. Haas, J. Dijkstra, C.J.F. Flipse, R.A. de Groot, A. Wold, *Phys. Rev. B* 35 (1987) 6195–6202.
- [80] W. Zhao, Z. Ghorannevis, L. Chu, M. Toh, C. Kloc, P.-H. Tan, G. Eda, *ACS Nano* 7 (2013) 791–797.
- [81] J. Zhang, X. Liu, Y. Wen, L. Shi, R. Chen, H. Liu, B. Shan, *ACS Appl. Mater. Interfaces* 9 (2017) 2509–2515.
- [82] F. Saiz, R. Rurrali, *Nano Ex.* 1 (2020) 010026.
- [83] F. Saiz, J. Carrete, R. Rurrali, *Nanoscale Adv.* 2 (2020) 5352–5361.
- [84] M. Dion, H. Rydberg, E. Schröder, D.C. Langreth, B.I. Lundqvist, *Phys. Rev. Lett.* 92 (2004) 246401.
- [85] M. Dion, H. Rydberg, E. Schröder, D.C. Langreth, B.I. Lundqvist, *Phys. Rev. Lett.* 95 (2005) 109902.
- [86] F. Bloch, *Z. Phys.* 52 (1929) 555–600.
- [87] H.J. Monkhorst, J.D. Pack, *Phys. Rev. B* 13 (1976) 5188–5192.
- [88] V. Wang, N. Xu, J.-C. Liu, G. Tang, W.-T. Geng, *Comput. Phys. Commun.* 267 (2021) 108033.
- [89] SeeK-path: the k-path finder and visualizer, (<https://www.materialscloud.org/work/tools/seekpath>) (visited May 27, 2024).
- [90] M.I. Aroyo, D. Orobengoa, G. De La Flor, E.S. Tasci, J.M. Perez-Mato, H. Wondratschek, *Acta Crystallogr. A Found. Adv.* 70 (2014) 126–137.
- [91] A Practical Guide to VASP, (<https://rosenreview.cbe.princeton.edu/dft/vasp>) (visited May 27, 2024).
- [92] k-points and ENCUT convergence tests before or after relaxation?, (<https://mattermodeling.stackexchange.com/questions/1896/k-points-and-encut-convergence-tests-before-or-after-relaxation>) (visited May 27, 2024).
- [93] Energy cut off and FFT mesh, (https://www.vasp.at/wiki/index.php/Energy_cut_off_and_FFT_mesh) (visited May 27, 2024).
- [94] H.B. Callen, *Thermodynamics and an Introduction to Thermostatistics*, John Wiley & Sons, 1991.
- [95] M.W. Zemansky, R.H. Dittman, H.L. Scott, *Am. J. Phys.* 66 (1998) 164–167.
- [96] H. Nyquist, *Proc. IEEE* 90 (2002) 280–305.
- [97] H.J. Landau, *Proc. IEEE* 55 (1967) 1701–1706.
- [98] C. da Silva, F. Saiz, D.A. Romero, C.H. Amon, in: ASME 2015 International Mechanical Engineering Congress and Exposition, 2015, pp. V08AT10A002. <https://doi.org/10.1115/IMECE2015-50675>.
- [99] F. Saiz, Y. Karaaslan, R. Rurrali, C. Sevik, *J. Appl. Phys.* 129 (2021) 155105.
- [100] K. Burke, *J. Chem. Phys.* 136 (2012) 150901.
- [101] B.G. Janesko, *Chem. Soc. Rev.* 50 (2021) 8470–8495.
- [102] S. Tappertzhofen, I. Valov, T. Tsuruoka, T. Hasegawa, R. Waser, M. Aono, *ACS Nano* 7 (2013) 6396–6402.
- [103] I. Valov, T. Tsuruoka, *J. Phys. D: Appl. Phys.* 51 (2018) 413001.
- [104] S.R. Ovshinsky, *Phys. Rev. Lett.* 21 (1968) 1450–1453.
- [105] D. Kau, S. Tang, I.V. Karpov, R. Dodge, B. Klehn, J.A. Kalb, J. Strand, A. Diaz, N. Leung, J. Wu, S. Lee, T. Langtry, K. Chang, C. Papagianni, J. Lee, J. Hirst, S. Erra, E. Flores, N. Righos, H. Castro, G. Spadini, in: 2009 IEEE International Electron Devices Meeting (IEDM), 2009, pp. 1–4. <https://doi.org/10.1109/IEDM.2009.5424263>.
- [106] L. Sech, M. Jenkins, *Intel. Micron Prod. Breakthr. Mem. Technol.* (2015).
- [107] T. Siegrist, P. Jost, H. Volker, M. Woda, P. Merkelbach, C. Schlockermann, M. Wuttig, *Nat. Mater.* 10 (2011) 202–208.
- [108] W. Zhang, A. Thieß, P. Zalden, R. Zeller, P.H. Dederichs, J.-Y. Raty, M. Wuttig, S. Blügel, R. Mazzarello, *Nat. Mater.* 11 (2012) 952–956.
- [109] W. Zhang, V.L. Deringer, R. Dronskowski, R. Mazzarello, E. Ma, M. Wuttig, *MRS Bull.* 40 (2015) 856–869.
- [110] J.Y. Raty, W. Zhang, J. Luckas, C. Chen, R. Mazzarello, C. Bichara, M. Wuttig, *Nat. Commun.* 6 (2015) 7467.
- [111] S. Gabardi, S. Caravati, G.C. Sosso, J. Behler, M. Bernasconi, *Phys. Rev. B* 92 (2015) 054201.
- [112] K. Shportko, S. Kremer, M. Woda, D. Lencer, J. Robertson, M. Wuttig, *Nat. Mater.* 7 (2008) 653–658.
- [113] J.-J. Wang, Y.-Z. Xu, R. Mazzarello, M. Wuttig, W. Zhang, *Materials* 10 (2017) 862.
- [114] L. Waldecker, T.A. Miller, M. Rudé, R. Bertoni, J. Osmond, V. Pruner, R. E. Simpson, R. Ernstorfer, S. Wall, *Nat. Mater.* 14 (2015) 991–995.
- [115] S.W. Fong, C.M. Neumann, H.-S.P. Wong, *IEEE Trans. Electron Devices* 64 (2017) 4374–4385.
- [116] G. Bruns, P. Merkelbach, C. Schlockermann, M. Salinga, M. Wuttig, T.D. Happ, J. B. Philipp, M. Kund, *Appl. Phys. Lett.* 95 (2009) 043108.
- [117] M. Luo, M. Wuttig, *Adv. Mater.* 16 (2004) 439–443.
- [118] Z. Sun, J. Zhou, R. Ahuja, *Phys. Rev. Lett.* 96 (2006) 055507.
- [119] K.B. Borisenko, Y. Chen, D.J.H. Cockayne, S.A. Song, H.S. Jeong, *Acta Mater.* 59 (2011) 4335–4342.
- [120] T.H. Lee, S.R. Elliott, *Phys. Rev. Lett.* 107 (2011) 145702.
- [121] D. Loke, T.H. Lee, W.J. Wang, L.P. Shi, R. Zhao, Y.C. Yeo, T.C. Chong, S.R. Elliott, *Science* 336 (2012) 1566–1569.
- [122] J.M. Skelton, T.H. Lee, S.R. Elliott, *Appl. Phys. Lett.* 101 (2012) 024106.
- [123] B. Prasai, G. Chen, D.A. Drabold, *Appl. Phys. Lett.* 102 (2013) 041907.
- [124] W. Zhang, I. Ronneberger, P. Zalden, M. Xu, M. Salinga, M. Wuttig, R. Mazzarello, *Sci. Rep.* 4 (2014) 6529.
- [125] Y. Saito, J. Tominga, P. Fons, A.V. Kolobov, T. Nakano, *Phys. Status Solidi (RRL) – Rapid Res. Lett.* 8 (2014) 302–306.
- [126] J.M. Skelton, D. Loke, T. Lee, S.R. Elliott, *ACS Appl. Mater. Interfaces* 7 (2015) 14223–14230.
- [127] S. Hu, B. Liu, Z. Li, J. Zhou, Z. Sun, *Comput. Mater. Sci.* 165 (2019) 51–58.
- [128] L. Sun, Y.-X. Zhou, X.-D. Wang, Y.-H. Chen, V.L. Deringer, R. Mazzarello, W. Zhang, *Npj Comput. Mater.* 7 (1) (2021) 8.
- [129] W.-X. Song, F. Martelli, Z. Song, *Mater. Sci. Semicond. Process.* 136 (2021) 106102.
- [130] K. Konstantinou, S.R. Elliott, J. Akola, J. Mater. Chem. C 10 (2022) 6744–6753.
- [131] C. Woo Lee, J.-S. Oh, S.-H. Park, H. Wook Lim, D. Sol Kim, K.-J. Cho, C.-W. Yang, Y.-K. Kwon, M.-H. Cho, *Appl. Surf. Sci.* 602 (2022) 154274.
- [132] Y. Xu, Y. Zhou, X.-D. Wang, W. Zhang, E. Ma, V.L. Deringer, R. Mazzarello, *Adv. Mater.* 34 (2022) 2109139.
- [133] D. Lencer, M. Salinga, B. Grabowski, T. Hickel, J. Neugebauer, M. Wuttig, *Nat. Mater.* 7 (2008) 972–977.
- [134] W. Zhang, R. Mazzarello, M. Wuttig, E. Ma, *Nat. Rev. Mater.* 4 (2019) 150–168.
- [135] J.A. Kalb, F. Spaepen, M. Wuttig, *J. Appl. Phys.* 98 (2005) 054910.
- [136] E.R. Meinders, A.V. Mijiritskii, L. van Pieterson, M. Wuttig, *Optical Data Storage: Phase-Change Media and Recording*, Springer Science & Business Media, 2006.
- [137] S. Kohara, K. Kato, S. Kimura, H. Tanaka, T. Usuki, K. Suzuya, H. Tanaka, Y. Moritomo, T. Matsunaga, N. Yamada, Y. Tanaka, H. Suematsu, M. Takata, *Appl. Phys. Lett.* 89 (2006) 201910.
- [138] S. Caravati, M. Bernasconi, T.D. Kühne, M. Krack, M. Parrinello, *Appl. Phys. Lett.* 91 (2007) 171906.
- [139] J. Hegedüs, S.R. Elliott, *Nat. Mater.* 7 (2008) 399–405.
- [140] J. Kalikka, J. Akola, R.O. Jones, *Phys. Rev. B* 90 (2014) 184109.
- [141] T. Matsunaga, N. Yamada, Y. Kubota, *Acta Cryst. B* 60 (2004) 685–691.
- [142] N. Yamada, *MRS Bull.* 21 (1996) 48–50.
- [143] N. Yamada, T. Matsunaga, *J. Appl. Phys.* 88 (2000) 7020–7028.
- [144] I. Ronneberger, Y. Chen, W. Zhang, R. Mazzarello, *Phys. Status Solidi (RRL) – Rapid Res. Lett.* 13 (2019) 1800552.
- [145] S. Gabardi, S. Caravati, M. Bernasconi, M. Parrinello, *J. Phys.: Condens. Matter* 24 (2012) 385803.
- [146] D.B. Strukov, G.S. Snider, D.R. Stewart, R.S. Williams, *Nature* 453 (2008) 80–83.
- [147] B. Hoefflinger, in: B. Hoefflinger (Ed.), *Chips 2020: A Guide to the Future of Nanoelectronics*, Springer, Berlin, Heidelberg, 2012, pp. 161–174.
- [148] D.S. Jeong, R. Thomas, R.S. Katiyar, J.F. Scott, H. Kohlstedt, A. Petraru, C. S. Wang, *Rep. Prog. Phys.* 75 (2012) 076502.
- [149] M. Lanza, R. Waser, D. Ielmini, J.J. Yang, L. Goux, J. Suñe, A.J. Kenyon, A. Mehonic, S. Spiga, V. Rana, S. Wiefels, S. Menzel, I. Valov, M.A. Villena, E. Miranda, X. Jing, F. Campabadal, M.B. Gonzalez, F. Aguirre, F. Palumbo, K. Zhu, J.B. Roldan, F.M. Puglisi, L. Larcher, T.-H. Hou, T. Prodromakis, Y. Yang, P. Huang, T. Wan, Y. Chai, K.L. Pey, N. Raghavan, S. Dueñas, T. Wang, Q. Xia, S. Pazos, *ACS Nano* 15 (2021) 17214–17231.
- [150] Fujitsu Semiconductor Memory Solution, (<https://www.fujitsu.com/jp/group/fsm/en/products/ram/>), (visited February 5, 2024).
- [151] S. Clima, Y.Y. Chen, R. Degraeve, M. Mees, K. Sankaran, B. Govoreanu, M. Jurczak, S. De Gendt, G. Pourtois, *Appl. Phys. Lett.* 100 (2012) 133102.
- [152] L. Zhao, Z. Jiang, H.-Y. Chen, J. Sohn, K. Okabe, B. Magyari-Köpe, H.-S. Philip Wong, Y. Nishi, in: 2014 IEEE International Electron Devices Meeting, 2014, p. 6.6.1–6.6.4. <https://doi.org/10.1109/IEDM.2014.7046998>.
- [153] S.R. Bradley, A.L. Shluger, G. Bersuker, *Phys. Rev. Appl.* 4 (2015) 064008.

- [154] S.R. Bradley, G. Bersuker, A.L. Shluger, *J. Phys.: Condens. Matter* 27 (2015) 415401.
- [155] Y. Dai, Z. Pan, F. Wang, X. Li, *AIP Adv.* 6 (2016) 085209.
- [156] D. Duncan, B. Magyari-Köpe, Y. Nishi, *IEEE Electron Device Lett.* 37 (2016) 400–403.
- [157] H. Nakamura, Y. Asai, *Phys. Chem. Chem. Phys.* 18 (2016) 8820–8826.
- [158] K.Z. Rushchanskii, S. Blügel, M. Ležaić, *Faraday Discuss.* 213 (2019) 321–337.
- [159] Y. Zhang, G.-Q. Mao, X. Zhao, Y. Li, M. Zhang, Z. Wu, W. Wu, H. Sun, Y. Guo, L. Wang, X. Zhang, Q. Liu, H. Lv, K.-H. Xue, G. Xu, X. Miao, S. Long, M. Liu, *Nat. Commun.* 12 (2021) 7232.
- [160] M.L. Urquiza, M.M. Islam, A.C.T. van Duin, X. Cartoixà, A. Strachan, *ACS Nano* 15 (2021) 12945–12954.
- [161] F.F. Athena, M.P. West, P. Basnet, J. Hah, Q. Jiang, W.-C. Lee, E.M. Vogel, *J. Appl. Phys.* 131 (2022) 204901.
- [162] H.D. Lee, B. Magyari-Köpe, Y. Nishi, *Phys. Rev. B* 81 (2010) 193202.
- [163] L. He, Z.-M. Liao, H.-C. Wu, X.-X. Tian, D.-S. Xu, G.L.W. Cross, G.S. Duesberg, I. V. Shvets, D.-P. Yu, *Nano Lett.* 11 (2011) 4601–4606.
- [164] B. Magyari-Köpe, M. Tendulkar, S.-G. Park, H.D. Lee, Y. Nishi, *Nanotechnology* 22 (2011) 254029.
- [165] S.-G. Park, B. Magyari-Köpe, Y. Nishi, *IEEE Electron Device Lett.* 32 (2011) 197–199.
- [166] K. Kamiya, M. Young Yang, S.-G. Park, B. Magyari-Köpe, Y. Nishi, M. Niwa, K. Shiraishi, *Appl. Phys. Lett.* 100 (2012) 073502.
- [167] M. Rogala, G. Bihlmayer, W. Speier, Z. Klusek, C. Rodenbücher, K. Szot, *Adv. Funct. Mater.* 25 (2015) 6382–6389.
- [168] Z. Wan, H. Mohammad, Y. Zhao, R.B. Darling, M.P. Anantram, *IEEE Electron Device Lett.* 39 (2018) 1290–1293.
- [169] J. Jiang, R. Pachter, K. Mahalingam, J. Ciston, R. Dhall, R.J. Bondi, M. J. Marinella, D.A. Telesca, S. Ganguli, *Adv. Electron. Mater.* 9 (2023) 2200828.
- [170] U. Rasheed, H. Ryu, C. Mahata, R.M.A. Khalil, M. Imran, A.M. Rana, F. Kousar, B. Kim, Y. Kim, S. Cho, F. Hussain, S. Kim, *J. Alloy. Compd.* 877 (2021) 160204.
- [171] Z. Guo, B. Sa, J. Zhou, Z. Sun, *J. Alloy. Compd.* 580 (2013) 148–151.
- [172] B. Magyari-Köpe, S.G. Park, H.-D. Lee, Y. Nishi, *J. Mater. Sci.* 47 (2012) 7498–7514.
- [173] L. Zhao, S.-G. Park, B. Magyari-Köpe, Y. Nishi, *Math. Comput. Model.* 58 (2013) 275–281.
- [174] D. Duncan, B. Magyari-Köpe, Y. Nishi, *MRS Online Proc. Libr. (OPL)* 1430 (2012) mrs12.
- [175] H. Xie, Q. Liu, Y. Li, H. Lv, M. Wang, X. Liu, H. Sun, X. Yang, S. Long, S. Liu, M. Liu, *Semicond. Sci. Technol.* 27 (2012) 125008.
- [176] L. Zhao, S.-G. Park, B. Magyari-Köpe, Y. Nishi, *Appl. Phys. Lett.* 102 (2013) 083506.
- [177] N. Deng, H. Pang, W. Wu, *Chin. Phys. B* 23 (2014) 107306.
- [178] M. Firdos, F. Hussain, M. Imran, M. Ismail, A.M. Rana, M.A. Javid, A. Majid, R.M. A. Khalil, H. Ullah, *Mater. Res. Express* 4 (2017) 106301.
- [179] D. Das, A. Barman, P.K. Sarkar, P. Rajput, S.N. Jha, R. Hübner, D. Kanjilal, P. Johari, A. Kanjilal, *J. Mater. Chem. C* 9 (2021) 3136–3144.
- [180] Y. Zhao, J. Wang, J. Xu, F. Yang, Q. Liu, Y. Dai, *J. Semicond.* 35 (2014) 042002.
- [181] D. Duncan, B. Magyari-Köpe, Y. Nishi, *Phys. Rev. Appl.* 7 (2017) 034020.
- [182] H. Zhang, B. Gao, B. Sun, G. Chen, L. Zeng, L. Liu, X. Liu, J. Lu, R. Han, J. Kang, B. Yu, *Appl. Phys. Lett.* 96 (2010) 123502.
- [183] B. Magyari-Köpe, L. Zhao, K. Kamiya, M.Y. Yang, M. Niwa, K. Shiraishi, Y. Nishi, *ECS Trans.* 64 (2014) 153.
- [184] F. Hussain, M. Imran, A.M. Rana, R.M.A. Khalil, E.A. Khera, S. Kiran, M.A. Javid, M.A. Sattar, M. Ismail, *Appl. Nanosci.* 8 (2018) 839–851.
- [185] S. Kim, S. Choi, J. Lee, W.D. Lu, *ACS Nano* 8 (2014) 10262–10269.
- [186] L. Goux, J.Y. Kim, B. Magyari-Köpe, Y. Nishi, A. Redolfi, M. Jurczak, *J. Appl. Phys.* 117 (2015) 124501.
- [187] L. Zhu, J. Zhou, Z. Guo, Z. Sun, *J. Phys. Chem. C* 120 (2016) 2456–2463.
- [188] J. Mulroue, D.M. Duffy, *Proc. R. Soc. A: Math., Phys. Eng. Sci.* 467 (2011) 2054–2065.
- [189] T. Tsuruoka, K. Terabe, T. Hasegawa, M. Aono, *Nanotechnology* 21 (2010) 425205.
- [190] Y. Li, J. Chu, W. Duan, G. Cai, X. Fan, X. Wang, G. Wang, Y. Pei, *ACS Appl. Mater. Interfaces* 10 (2018) 24598–24606.
- [191] S. Choi, J. Yang, G. Wang, *Adv. Mater.* 32 (2020) 2004659.
- [192] U. Diebold, *Surf. Sci. Rep.* 48 (2003) 53–229.
- [193] T. Tamura, S. Ishibashi, K. Terakura, H. Weng, *Phys. Rev. B* 80 (2009) 195302.
- [194] L. Giordano, J. Goniakowski, G. Pacchioni, *Phys. Rev. B* 67 (2003) 045410.
- [195] J. Aeschlimann, M.H. Bani-Hashemian, F. Ducry, A. Emboras, M. Luisier, *Solid-State Electron.* 199 (2023) 108493.
- [196] K.K.H. Smith, S.V. Suryavanshi, M. Muñoz Rojo, A.D. Tedjarati, E. Pop, *ACS Nano* 11 (2017) 8456–8463.
- [197] K.K.H. Smith, A.V. Kravev, C.S. Bailey, H.R. Lee, E. Yalon, B. Aslan, M. Muñoz Rojo, S. Krylyuk, P. Taheri, A.V. Davydov, T.F. Heinz, E. Pop, *ACS Appl. Nano Mater.* 1 (2018) 572–579.
- [198] J. Jian, H. Feng, P. Dong, H. Chang, A. Vena, S. Brice, *Adv. Electron. Mater.* 8 (2022) 2100905.
- [199] S. Li, S. Wang, D.-M. Tang, W. Zhao, H. Xu, L. Chu, Y. Bando, D. Golberg, G. Eda, *Appl. Mater. Today* 1 (2015) 60–66.
- [200] S.M. Eichfeld, L. Hossain, Y.-C. Lin, A.F. Piasecki, B. Kupp, A.G. Birdwell, R. A. Burke, N. Lu, X. Peng, J. Li, A. Azcatl, S. McDonnell, R.M. Wallace, M.J. Kim, T. S. Mayer, J.M. Redwing, J.A. Robinson, *ACS Nano* 9 (2015) 2080–2087.
- [201] C.L. He, F. Zhuge, X.F. Zhou, M. Li, G.C. Zhou, Y.W. Liu, J.Z. Wang, B. Chen, W. J. Su, Z.P. Liu, Y.H. Wu, P. Cui, R.-W. Li, *Appl. Phys. Lett.* 95 (2009) 232101.
- [202] F.J. Romero, A. Toral, A. Medina-Rull, C.L. Moraila-Martinez, D.P. Morales, A. Ohata, A. Godoy, F.G. Ruiz, N. Rodríguez, *Front. Mater.* 7 (2020).
- [203] F. Hui, E. Grustan-Gutierrez, S. Long, Q. Liu, A.K. Ott, A.C. Ferrari, M. Lanza, *Adv. Electron. Mater.* 3 (2017) 1600195.
- [204] L. Jiang, Y. Shi, F. Hui, K. Tang, Q. Wu, C. Pan, X. Jing, H. Uppal, F. Palumbo, G. Lu, T. Wu, H. Wang, M.A. Villena, X. Xie, P.C. McIntyre, M. Lanza, *ACS Appl. Mater. Interfaces* 9 (2017) 39758–39770.
- [205] G. Lu, T. Wu, Q. Yuan, H. Wang, H. Wang, F. Ding, X. Xie, M. Jiang, *Nat. Commun.* 6 (2015) 6160.
- [206] S. Mitra, S. Mahapatra, *J. Appl. Phys.* 132 (2022) 224302.
- [207] X.-D. Li, N.-K. Chen, B.-Q. Wang, X.-B. Li, *Appl. Phys. Lett.* 121 (2022) 073505.
- [208] S. Mitra, A. Kabiraj, S. Mahapatra, *Npj 2D Mater. Appl.* 5 (2021) 1–11.
- [209] Y. Da, J. Liu, L. Zhou, X. Zhu, X. Chen, L. Fu, *Adv. Mater.* 31 (2019) 1802793.
- [210] N. Li, Y. Wang, H. Sun, J. Hu, M. Zheng, S. Ye, Q. Wang, Y. Li, D. He, J. Wang, G. Zhang, J. Qi, *Appl. Phys. Lett.* 116 (2020) 063503.
- [211] S.H. Chae, Y. Jin, T.S. Kim, D.S. Chung, H. Na, H. Nam, H. Kim, D.J. Perello, H. Y. Jeong, T.H. Ly, Y.H. Lee, *ACS Nano* 10 (2016) 1309–1316.
- [212] M. Wang, S. Cai, C. Pan, C. Wang, X. Lian, Y. Zhuo, K. Xu, T. Cao, X. Pan, B. Wang, S.-J. Liang, J.J. Yang, P. Wang, F. Miao, *Nat. Electron* 1 (2018) 130–136.
- [213] W. Tong, Y. Liu, *Sci. China Inf. Sci.* 66 (2023) 160402.
- [214] J.-Y. Mao, S. Wu, G. Ding, Z.-P. Wang, F.-S. Qian, J.-Q. Yang, Y. Zhou, S.-T. Han, *Small* 18 (2022) 2106253.
- [215] C. Wen, X. Li, T. Zanotti, F.M. Puglisi, Y. Shi, F. Saiz, A. Antidormi, S. Roche, W. Zheng, X. Liang, J. Hu, S. Duhm, J.B. Roldan, T. Wu, V. Chen, E. Pop, B. Garrido, K. Zhu, F. Hui, M. Lanza, *Adv. Mater.* 33 (2021) 2100185.
- [216] R. Ge, X. Wu, M. Kim, J. Shi, S. Sonde, L. Tao, Y. Zhang, J.C. Lee, D. Akinwande, *Nano Lett.* 18 (2018) 434–441.
- [217] R. Xu, H. Jiang, M.-H. Lee, D. Amanov, Y. Cho, H. Kim, S. Park, H. Shin, D. Ham, *Nano Lett.* 19 (2019) 2411–2417.
- [218] X.-D. Li, B.-Q. Wang, N.-K. Chen, X.-B. Li, *Nanotechnology* 34 (2023) 205201.
- [219] J. Ge, H. Huang, Z. Ma, W. Chen, X. Cao, H. Fang, J. Yan, Z. Liu, W. Wang, S. Pan, *Mater. Des.* 198 (2021) 109366.
- [220] S.K. Ojha, A. Singh, A.K. Ojha, *Mater. Chem. Phys.* 240 (2020) 122149.
- [221] W.-J. Yin, T. Shi, Y. Yan, *Appl. Phys. Lett.* 104 (2014) 063903.
- [222] T.T. Ngo, U.T.T. Doan, Q.T.T. Vo, T.L. Huynh, N.H. Vu, H.K.T. Ta, L.T.M. Hoa, Y. Kawazoe, P.T. Nguyen, N.K. Pham, *J. Phys. D: Appl. Phys.* 56 (2023) 215301.
- [223] D. Harshini, V.M. Angela, P. Devibala, P.M. Imran, N.S.P. Bhuvanesh, S. Nagarajan, *ACS Appl. Electron. Mater.* 4 (2022) 4383–4395.
- [224] M. Julliere, *Phys. Lett. A* 54 (1975) 225–226.
- [225] H. Yang, S.O. Valenzuela, M. Chshiev, S. Couet, B. Diény, B. Dlubak, A. Fert, K. Garello, M. Janet, D.-E. Jeong, K. Lee, T. Lee, M.-B. Martin, G.S. Kar, P. Séneor, H.-J. Shin, S. Roche, *Nature* 606 (2022) 663–673.
- [226] T. Andre, S.M. Alam, D. Gogl, C.K. Subramanian, H. Lin, W. Meadows, X. Zhang, N.D. Rizzo, J. Janesky, D. Houssameddine, J.M. Slaughter, *Proceedings of the IEEE 2013 Custom Integrated Circuits Conference*, 2013, pp. 1–8, <https://doi.org/10.1109/CICC.2013.6658449>.
- [227] X. Fong, Y. Kim, R. Venkatesan, S.H. Choday, A. Raghunathan, K. Roy, *Proc. IEEE* 104 (2016) 1449–1488.
- [228] I. Bouziani, Y. Benhouri, I. Essaoudi, A. Ainane, R. Ahuja, *Mater. Sci. Eng.: B* 253 (2020) 114484.
- [229] M. Gani, K.A. Shah, S.A. Parah, *IEEE Trans. Nanotechnol.* 20 (2021) 466–473.
- [230] X. Li, J.-T. Lü, J. Zhang, L. You, Y. Su, E.Y. Tsymbal, *Nano Lett.* 19 (2019) 5133–5139.
- [231] D. Waldron, L. Liu, H. Guo, *Nanotechnology* 18 (2007) 424026.
- [232] M. Chakraverty, H.M. Kittur, P.A. Kumar, *IEEE Trans. Nanotechnol.* 12 (2013) 971–977.
- [233] R.A. de Groot, F.M. Mueller, P.G. van Engen, K.H.J. Buschow, *Phys. Rev. Lett.* 50 (1983) 2024–2027.
- [234] J.-H. Park, E. Vesco, H.-J. Kim, C. Kwon, R. Ramesh, T. Venkatesan, *Nature* 392 (1998) 794–796.
- [235] M. Ishikawa, H. Sugiyama, T. Inokuchi, T. Tanamoto, K. Hamaya, N. Tezuka, Y. Saito, *J. Appl. Phys.* 114 (2013) 243904.
- [236] Y.P. Feng, L. Shen, M. Yang, A. Wang, M. Zeng, Q. Wu, S. Chintalapati, C.-R. Chang, *WIREs Comput. Mol. Sci.* 7 (2017) e1313.
- [237] A. Mahmood, S.M. Ramay, W. Al-Masry, A.A. Al-Zahrani, N.Y.A. Al-Garadi, *J. Mater. Res. Technol.* 9 (2020) 14783–14791.
- [238] S. Özdemir Kart, M. Uludogan, I. Karaman, T. Çagin, *Phys. Status Solidi (a)* 205 (2008) 1026–1035.
- [239] T.D. Huan, V. Sharma, G.A. Rossetti, R. Ramprasad, *Phys. Rev. B* 90 (2014) 064111.
- [240] M. Pesić, C. Künneth, M. Hoffmann, H. Mulaosmanovic, S. Müller, E.T. Breyer, U. Schroeder, A. Kersch, T. Mikolajick, S. Slesazeck, *J. Comput. Electron.* 16 (2017) 1236–1256.
- [241] S.E. Reyes-Lillo, K.F. Garrity, K.M. Rabe, *Phys. Rev. B* 90 (2014) 140103.
- [242] B. Huang, Z. Xie, D. Feng, L. Li, X. Li, T.R. Paudel, Z. Han, W. Hu, G. Yuan, T. Wu, Z. Zhang, *Adv. Electron. Mater.* 8 (2022) 2101059.
- [243] L. Pan, G. Liu, H. Li, S. Meng, L. Han, J. Shang, B. Chen, A.E. Platero-Prats, W. Lu, X. Zou, R.-W. Li, *J. Am. Chem. Soc.* 136 (2014) 17477–17483.
- [244] Q. Wang, S.-X. Go, C. Liu, M. Li, Y. Zhu, L. Li, T.H. Lee, D.K. Loke, *AIP Adv.* 12 (2022) 125303.
- [245] Q. Wang, S.-X. Go, C. Liu, M. Li, Y. Zhu, L. Li, T. Hoon Lee, D.K. Loke, *Mater. Adv.* 3 (2022) 5532–5539.
- [246] J.P.B. Silva, K. Kamakshi, K.C. Sekhar, J.A. Moreira, A. Almeida, M. Pereira, M.J. M. Gomes, *J. Phys. Chem. Solids* 92 (2016) 7–10.

- [247] H. Fan, C. Chen, Z. Fan, L. Zhang, Z. Tan, P. Li, Z. Huang, J. Yao, G. Tian, Q. Luo, Z. Li, X. Song, D. Chen, M. Zeng, J. Gao, X. Lu, Y. Zhao, X. Gao, J.-M. Liu, *Appl. Phys. Lett.* 111 (2017) 252901.
- [248] J.E. Lowther, J.K. Dewhurst, J.M. Leger, J. Haines, *Phys. Rev. B* 60 (1999) 14485–14488.
- [249] R. Materlik, C. Künneth, A. Kersch, *J. Appl. Phys.* 117 (2015) 134109.
- [250] S.V. Barabash, D. Pramanik, Y. Zhai, B. Magyari-Kope, Y. Nishi, *ECS Trans.* 75 (2017) 107.
- [251] S. Clima, D.J. Wouters, C. Adelmann, T. Schenk, U. Schroeder, M. Jurczak, G. Pourtois, *Appl. Phys. Lett.* 104 (2014) 092906.
- [252] M.H. Park, Y.H. Lee, T. Mikolajick, U. Schroeder, C.S. Hwang, *MRS Commun.* 8 (2018) 795–808.
- [253] T. Mikolajick, S. Slesazeck, M.H. Park, U. Schroeder, *MRS Bull.* 43 (2018) 340–346.
- [254] S.P. Beckman, X. Wang, K.M. Rabe, D. Vanderbilt, *Phys. Rev. B* 79 (2009) 144124.
- [255] D.R. Islamov, T.V. Perevalov, *Microelectron. Eng.* 216 (2019) 111041.
- [256] Z. Chai, P. Freitas, W. Zhang, F. Hatem, J.F. Zhang, J. Marsland, B. Govoreanu, L. Goux, G.S. Kar, *IEEE Electron Device Lett.* 39 (2018) 1652–1655.
- [257] G. González-Cordero, M.B. González, M. Zabala, K. Kalam, A. Tamm, F. Jiménez-Molinós, F. Campabadal, J.B. Roldán, *Solid-State Electron.* 183 (2021) 108034.
- [258] B. Sun, S. Ranjan, G. Zhou, T. Guo, Y. Xia, L. Wei, Y.N. Zhou, Y.A. Wu, *Mater. Today Adv.* 9 (2021) 100125.
- [259] M.K. Hota, M.N. Hedhili, N. Wehbe, M.A. McLachlan, H.N. Alshareef, *Adv. Mater. Interfaces* 3 (2016) 1600192.
- [260] S. Pazos, T. Becker, M.A. Villena, W. Zheng, Y. Shen, Y. Yuan, O. Alharbi, K. Zhu, J.B. Roldán, G. Wirth, F. Palumbo, M. Lanza, *Adv. Funct. Mater.* n/a (2023) 2213816.
- [261] M.J. Uren, D.J. Day, M.J. Kirton, *Appl. Phys. Lett.* 47 (1985) 1195–1197.
- [262] T. Matsumoto, K. Kobayashi, H. Onodera, in: *Proceedings of the IEEE 2014 Custom Integrated Circuits Conference*, 2014, pp. 1–8. <https://doi.org/10.1109/CICC.2014.6945997>.
- [263] F.M. Puglisi, N. Zagni, L. Larcher, P. Pavan, *IEEE Trans. Electron Devices* 65 (2018) 2964–2972.
- [264] F.M. Puglisi, P. Pavan, L. Vandelli, A. Padovani, M. Bertocchi, L. Larcher, in: *2015 IEEE International Reliability Physics Symposium*, 2015, p. 5B.5.1-5B.5.6. <https://doi.org/10.1109/IRPS.2015.7112746>.
- [265] T. Grasser, *Microelectron. Reliab.* 52 (2012) 39–70.
- [266] J.P. Campbell, P.M. Lenahan, A.T. Krishnan, S. Krishnan, *IEEE Trans. Device Mater. Reliab.* 6 (2006) 117–122.
- [267] T. Grasser, B. Kaczor, W. Goes, Th Achinger, Ph Hehenberger, M. Nelhiebel, in: *2009 IEEE International Reliability Physics Symposium*, 2009, pp. 33–44. <https://doi.org/10.1109/IRPS.2009.5173221>.
- [268] J.T. Ryan, P.M. Lenahan, T. Grasser, H. Enichlmair, in: *2010 IEEE International Reliability Physics Symposium*, 2010, pp. 43–49. <https://doi.org/10.1109/IRPS.2010.5488854>.
- [269] C.H. Henry, D.V. Lang, *Phys. Rev. B* 15 (1977) 989–1016.
- [270] P.E. Blöchl, *Phys. Rev. B* 62 (2000) 6158–6179.
- [271] F. Schanovsky, W. Göts, T. Grasser, *J. Comput. Electron.* 9 (2010) 135–140.
- [272] F.M. Puglisi, L. Larcher, P. Pavan, A. Padovani, G. Bersuker, in: *2014 IEEE International Reliability Physics Symposium*, 2014, p. MY.5.1-MY.5.5. <https://doi.org/10.1109/IRPS.2014.6861160>.
- [273] F.M. Puglisi, P. Pavan, A. Padovani, L. Larcher, G. Bersuker, *Solid-State Electron.* 84 (2013) 160–166.
- [274] S. Pazos, W. Zheng, T. Zanotti, F. Aguirre, T. Becker, Y. Shen, K. Zhu, Y. Yuan, G. Wirth, F. Maria Puglisi, J. Bautista Roldán, F. Palumbo, M. Lanza, *Nanoscale* 15 (2023) 2171–2180.
- [275] A.S. Foster, F. Lopez Gejo, A.L. Shluger, R.M. Nieminen, *Phys. Rev. B* 65 (2002) 174117.
- [276] D. Muñoz Ramo, J.L. Gavartin, A.L. Shluger, G. Bersuker, *Phys. Rev. B* 75 (2007) 205336.
- [277] A. Kimmel, P. Sushko, A. Shluger, G. Bersuker, *ECS Trans.* 19 (2009) 3.
- [278] E.H. Poindexter, W.L. Warren, *J. Electrochem. Soc.* 142 (1995) 2508.
- [279] W.L. Warren, J. Kanicki, E.H. Poindexter, *Colloids Surf. A: Physicochem. Eng. Asp.* 115 (1996) 311–317.
- [280] Volker L. Deringer, Albert P. Bartók, Noam Bernstein, David M. Wilkins, Michele Ceriotti, Gábor Csányi, *Chem. Rev.* 121 (2021) 10073–10141.
- [281] H. Wang, L. Zhang, J. Han, W. E, *Comput. Phys. Commun.* 228 (2018) 178–184.
- [282] J. Zeng, D. Zhang, D. Lu, P. Mo, Z. Li, Y. Chen, M. Rynik, L. Huang, Z. Li, S. Shi, Y. Wang, H. Ye, P. Tuo, J. Yang, Y. Ding, Y. Li, D. Tisi, Q. Zeng, H. Bao, Y. Xia, J. Huang, K. Muraoka, Y. Wang, J. Chang, F. Yuan, S.D. Bore, C. Cai, Y. Lin, B. Wang, J. Xu, J.-X. Zhu, C. Luo, Y. Zhang, R.E.A. Goodall, W. Liang, A.K. Singh, S. Yao, J. Zhang, R. Wentzovitch, J. Han, J. Liu, W. Jia, D.M. York, W. E, R. Car, L. Zhang, H. Wang, *J. Chem. Phys.* 159 (2023) 054801.
- [283] I.S. Novikov, K. Gubaev, E.V. Podryabinkin, A.V. Shapeev, *Mach. Learn.: Sci. Technol.* 2 (2020) 025002.
- [284] Y. Zuo, C. Chen, X. Li, Z. Deng, Y. Chen, J. Behler, G. Csányi, A.V. Shapeev, A. P. Thompson, M.A. Wood, S.P. Ong, *J. Phys. Chem. A* 124 (2020) 731–745.
- [285] V.L. Deringer, M.A. Caro, G. Csányi, *Adv. Mater.* 31 (2019) 1902765.
- [286] D. Marx, J. Hutter, *Mod. Methods Algorithms Quantum Chem.* 1 (2000) 141.
- [287] R. Iftimie, P. Minary, M.E. Tuckerman, *Proc. Natl. Acad. Sci.* 102 (2005) 6654–6659.
- [288] L. Grenouillet, N. Castellani, A. Persico, V. Meli, S. Martin, O. Billoint, R. Segaud, S. Bernasconi, P. Pellissier, C. Jahan, C. Charpin-Nicolle, P. Dezest, C. Carabasse, P. Besombes, S. Ricavy, N.-P. Tran, A. Magalhaes-Lucas, A. Roman, C. Boixaderas, T. Magis, M. Bedjaoui, M. Tessaire, A. Seignard, F. Mazen, S. Landis, E. Vianello, G. Molas, F. Gaillard, J. Arcamone, E. Nowak, in: *2021 IEEE International Memory Workshop (IMW)*, 2021, pp. 1–4. <https://doi.org/10.1109/IMW51353.2021.9439607>.
- [289] J.-Y. Chen, C.-L. Hsin, C.-W. Huang, C.-H. Chiu, Y.-T. Huang, S.-J. Lin, W.-W. Wu, L.-J. Chen, *Nano Lett.* 13 (2013) 3671–3677.
- [290] E.A. Khera, H. Ullah, M. Imran, N.A. Niaz, F. Hussain, R.M.A. Khalil, U. Resheed, A.M. Rana, M.I. Hussain, C. Mahata, S. Kim, *J. Mol. Graph. Model.* 103 (2021) 107825.
- [291] H. Lu, S. Clark, Y. Guo, J. Robertson, *J. Appl. Phys.* 129 (2021) 240902.
- [292] F.C. Mocanu, K. Konstantinou, T.H. Lee, N. Bernstein, V.L. Deringer, G. Csányi, S. R. Elliott, *J. Phys. Chem. B* 122 (2018) 8998–9006.
- [293] M. Shi, P. Mo, J. Liu, *IEEE Electron Device Lett.* 41 (2020) 365–368.
- [294] H.-Y. Li, X.-D. Huang, J.-H. Yuan, Y.-F. Lu, T.-Q. Wan, Y. Li, K.-H. Xue, Y.-H. He, M. Xu, H. Tong, X.-S. Miao, *Adv. Electron. Mater.* 6 (2020) 2000309.
- [295] A. Mazumder, T. Ahmed, E. Mayes, S.A. Tawfik, S.P. Russo, M.X. Low, A. Ranjan, S. Balendhran, S. Walia, *Adv. Electron. Mater.* 8 (2022) 2100999.
- [296] G. Milano, F. Raftone, M. Luebben, L. Boarino, G. Cicero, I. Valov, C. Ricciardi, *ACS Appl. Mater. Interfaces* 12 (2020) 48773–48780.
- [297] N. Onofrio, D. Guzman, A. Strachan, *Nanoscale* 8 (2016) 14037–14047.
- [298] S. Goumri-Said, M.B. Kanoun, F. Calvayrac, J. Magn. Magn. Mater. 321 (2009) 1012–1014.
- [299] M. Imam, N. Stojić, N. Binggeli, *Nanotechnology* 28 (2017) 315202.
- [300] Y. Umeno, T. Shimada, T. Kitamura, C. Elsässer, *Phys. Rev. B* 74 (2006) 174111.
- [301] J.P. Velev, C.-G. Duan, K.D. Belashchenko, S.S. Jaswal, E.Y. Tsymbal, *Phys. Rev. Lett.* 98 (2007) 137201.
- [302] M. Zhang, X. Chen, Z. Chen, R. Dan, Y. Wei, H. Rong, Q. Wang, X. Chen, A. Han, Y. Wang, W. Shao, H. Zhang, Y. Zhang, L. Wang, J. Xu, Y. Tong, *Appl. Surf. Sci.* 613 (2023) 155956.
- [303] L.G.S. Albano, T.P. Vello, D.H.S. de Camargo, R.M.L. da Silva, A.C.M. Padilha, A. Fazzio, C.C.B. Bufon, *Nano Lett.* 20 (2020) 1080–1088.
- [304] S.H. Foulger, Y. Bandera, B. Grant, J. Vilčáková, P. Sáha, *J. Mater. Chem. C* 9 (2021) 8975–8986.
- [305] S. Goswami, D. Thompson, R.S. Williams, S. Goswami, T. Venkatesan, *Appl. Mater. Today* 19 (2020) 100626.
- [306] S. Goswami, R. Pramanick, A. Patra, S.P. Rath, M. Foltin, A. Ariando, D. Thompson, T. Venkatesan, S. Goswami, R.S. Williams, *Nature* 597 (2021) 51–56.
- [307] Y. Han, C. Nickle, Z. Zhang, H.P.A.G. Astier, T.J. Duffin, D. Qi, Z. Wang, E. del Barco, D. Thompson, C.A. Nijhuis, *Nat. Mater.* 19 (2020) 843–848.
- [308] B. Hu, R. Quhe, C. Chen, F. Zhuge, X. Zhu, S. Peng, X. Chen, L. Pan, Y. Wu, W. Zheng, Q. Yan, J. Lu, R.-W. Li, *J. Mater. Chem.* 22 (2012) 16422–16430.
- [309] G. Liu, X. Zhuang, Y. Chen, B. Zhang, J. Zhu, C.-X. Zhu, K.-G. Neoh, E.-T. Kang, *Appl. Phys. Lett.* 95 (2009) 253301.
- [310] P. Liu, F. Hui, F. Aguirre, F. Saiz, L. Tian, T. Han, Z. Zhang, E. Miranda, M. Lanza, *Adv. Mater.* 34 (2022) 2201197.
- [311] Y. Tao, H. Liu, H.-Y. Kong, T.-X. Wang, H. Sun, Y.J. Li, X. Ding, L. Sun, B.-H. Han, *Angew. Chem.* 134 (2022) e202205796.
- [312] K. My Tran, D. Phuc Do, H. Nam Vu, T.T. Nguyen, B. Thang Phan, K. Hanh Ta Thi, K. Ngoc Pham, *Mater. Sci. Eng. C* 262 (2020) 114788.
- [313] A. Jay, C. Huet, N. Salles, M. Gunde, L. Martin-Samos, N. Richard, G. Landa, V. Goiffon, S. De Gironcoli, A. Hémeryck, N. Mousseau, *J. Chem. Theory Comput.* 16 (2020) 6726–6734.
- [314] A. Jay, A. Hémeryck, F. Cristiano, D. Rideau, P.L. Julliard, V. Goiffon, A. LeRoch, N. Richard, L.M. Samos, S.D. Gironcoli, in: *2021 International Conference on Simulation of Semiconductor Processes and Devices (SISPAD)*, 2021, pp. 128–132. <https://doi.org/10.1109/SISPAD54002.2021.9592553>.
- [315] F. Schanovsky, W. Göts, T. Grasser, *J. Vac. Sci. Technol. B* 29 (2011) 01A201.
- [316] J.C. Slater, *Phys. Rev.* 81 (1951) 385–390.
- [317] S.H. Vosko, L. Wilk, M. Nusair, *Can. J. Phys.* 58 (1980) 1200–1211.
- [318] J.P. Perdew, *Phys. Rev. B* 33 (1986) 8822–8824.
- [319] G. Vignale, W. Kohn, in: J.F. Dobson, G. Vignale, M.P. Das (Eds.), *Electronic Density Functional Theory: Recent Progress and New Directions*, Springer US, Boston, MA, 1998, pp. 199–216.
- [320] J.P. Perdew, P. Ziesche, H. Eschrig, (1991).
- [321] J.P. Perdew, K. Burke, M. Ernzerhof, *Phys. Rev. Lett.* 77 (1996) 3865–3868.
- [322] J.P. Perdew, A. Ruzsinszky, L.A. Constantin, J. Sun, G.I. Csonka, *J. Chem. Theory Comput.* 5 (2009) 902–908.
- [323] B. Hammer, L.B. Hansen, J.K. Nørskov, *Phys. Rev. B* 59 (1999) 7413–7421.
- [324] Y. Zhao, D.G. Truhlar, *J. Chem. Phys.* 128 (2008) 184109.
- [325] P.J. Stephens, F.J. Devlin, C.F. Chabalowski, M.J. Frisch, *J. Phys. Chem.* 98 (1994) 11623–11627.
- [326] J.P. Perdew, M. Ernzerhof, K. Burke, *J. Chem. Phys.* 105 (1996) 9982–9985.
- [327] J. Heyd, G.E. Scuseria, M. Ernzerhof, *J. Chem. Phys.* 118 (2003) 8207–8215.
- [328] A.D. Becke, *J. Chem. Phys.* 107 (1997) 8554–8560.
- [329] V.N. Staroverov, G.E. Scuseria, J. Tao, J.P. Perdew, *J. Chem. Phys.* 119 (2003) 12129–12137.



Marco A. Villena got a PhD in Physics with honors in 2015 at the University of Granada (Spain). After completing postdocs at Soochow University (China) and Stanford University (USA) in 2019, he joined to Applied Materials (Italy) as physicist at the AI R&D department. Since 2022, he is senior postdoctoral fellow at the King Abdullah University of Science and Technology (Saudi Arabia). His research focuses on characterization of 2D materials using several ab initio simulations, with special emphasis on resistive switching applications. He has published over 32 research articles in top journals, including one Nature.



Stephan Roche is ICREA Research Professor since 2009, head of “Theoretical & computational Nanoscience Group” at the Catalan Institute of Nanoscience and Nanotechnology (ICN2). He is a theoretician expert in the study of quantum transport theory in condensed matter, spin transport physics and devices simulation. He has pioneered the development of linear scaling quantum transport approaches, which enable unrivalled simulations of billion atoms-scale disordered models (www.lsquant.org), methods which are now connected with Artificial Intelligence methods. S. Roche is a Friedrich Wilhelm Bessel awardee (Alexander Von-Humboldt Foundation, Germany) and has worked as PhD, postdoc, assistant professor, research staff and visiting researchers at many institutions such as at French CNRS and CEA, University of Valladolid (Spain), University of TU-Dresden, National University of Singapore, and University of Tokyo. He is Editor in Chief of J. Phys. Materials from IoP since 2018



Onurcan Kaya is a doctoral researcher at the Catalan Institute of Nanoscience and Nanotechnology in Spain and a PhD student at both the Autonomous University of Barcelona in Spain and RMIT University in Australia. He received his BSc in Mechanical Engineering from Istanbul Technical University in 2018 and his MSc in Mechanical Engineering from Bogazici University. His research focuses on the generation of machine learning-based interatomic potentials and the investigation of material properties in disordered materials using atomistic simulation tools.



Mario Lanza got a PhD in Electronic Engineering in 2010 at the Autonomous University of Barcelona. After completing postdocs at Peking University and Stanford University, in 2013 he joined Soochow University (in China), where he promoted until the rank of Full Professor. Since October 2020 he is an Associate Professor of Materials Science and Engineering at the King Abdullah University of Science and Technology (in Saudi Arabia), where he leads a group formed by 10 PhD students and postdocs. His research focuses on how to improve electronic devices and circuits using 2D materials, with special emphasis on resistive switching applications. Prof. Lanza has published over 200 research articles in top journals, including 1 Nature, 2 Science, 7 Nature Electronics and multiple IEDM papers (among others), which have been cited over 11,000 times. Prof. Lanza has received multiple top distinctions, like the IEEE Fellow and Marie Curie Fellow (among others), and he is a Distinguished Lecturer from the IEEE – Electron Devices Society. Prof. Lanza is the Editor-in-Chief of the journal Microelectronic Engineering (Elsevier), and he serves in the board of many other journals and international conferences, including IEEE-IEDM and IEEE-IRPS.



Udo Schwingenschlögl is a Professor of Applied Physics at King Abdullah University of Science and Technology (KAUST). He joined KAUST as founding faculty member in 2008. His research interests in condensed matter physics and first-principles materials modeling focus on 2D materials, interface and defect physics, correlated materials, thermoelectric materials, metal-ion batteries, nanoparticles, and quantum transport.